Phototherapeutic Devices for the Treatment of Diabetic Retinopathy

Thesis by

Colin Andrew Cook

In Partial Fulfillment of the Requirements

for the Degree of

Doctor of Philosophy in Medical Engineering

CALIFORNIA INSTITUTE OF TECHNOLOGY

Pasadena, California

2019

(Defended 4-Decemeber-2018)

Colin Andrew Cook
ORCID: 0000-0002-6283-5105

ACKNOWLEDGEMENTS

Dedicated to my family and those who make our city on a hill shine brighter.

Thank you to my advisor Professor Yu-Chong Tai for giving me the latitude, resources, and support to pursue this work. You are a selfless champion of your students and I cherish the lessons and insights you have shared with me. It has been truly inspiring watching you make your vision of medicine a reality through the growth of the Medical Engineering Department. I will do whatever I can to ensure this legacy continues to flourish in the decades to come.

To my lab mates, Nick, Aubrey, May, Jake, Yuan, Shane, and Allen, it has been a pleasure working with each of you. I will never forget the lab dinners we enjoyed together or the Parylene machine cleanings we endured together. You are some of the brightest, hardest working individuals I have met and I know you will exceed my expectations. Thank you for taking the time to train me on equipment, to talk through research challenges, and to inspire me through your creativity. Nick, your stewardship of the lab, commitment to engineering excellence, and thoughtful guidance has been deeply appreciated. I have learned more about design and microfabrication from you than any textbook. Beyond your explicit contributions, you laid the foundations for this work in ways that I cannot hope to deconvolute. Know that I recognize this and am grateful for it. You are an exceptional individual.

To Christine and Trevor, thank you each for taking such pride in your work and for always going above and beyond to facilitate my research. Christine, you are a managerial maven and since the day we met you have faithfully shielded me from my

kryptonite: bureaucracy. You have made my life effortless within the department and freed up my mental bandwidth to focus exclusively on research challenges. This has been a gift. Beyond this, you are a caring, considerate, and all-around wonderful person. The department would not run without you. Trevor, the depth and breadth of your engineering know-how is staggering. I will always remember your can-do attitude, sense of humor, and willingness to jump in the cleanroom to fix a machine at a moment's notice. The MEMS Lab turns medical concepts into prototypes faster than anywhere in the world thanks to your diligent maintenance of equipment and continued expansion of capabilities.

To my collaborators at the University of Southern California, Professor Humayun, Dr Juan Carlos Martinez Camarillo, Qianhui Yang, and Karthik Murali, it was a pleasure working with you on the animal studies. Thank you for your flexibility, curiosity, can-do attitude, and commitment to excellence.

To my earliest mentors and role models, thank you for your unwavering support and motivation during my formative years. Jane Kuipers, you were that great teacher in my life. You taught me to channel talent and energy into meaningful endeavors and recited Ms. Mead's mantra long enough that I fell for it. Jack Wieler, you broadened my horizons and assuaged my cynicism of the humanities by introducing me to brilliant playwrights and challenging works. I can no longer sit at a formal dinner without thinking of *The Bald Soprano* and the absurdity of it. To the members of SHAD Valley, thank you for the work you do to empower youth. My summer at the University of British Columbia changed my career trajectory and gave me the confidence to pursue my ambitions. To Professors Cluett and Ho, thank you for taking a chance on me. My time at

the National University of Singapore opened my eyes to the field of research and ignited a passion that has carried me through my doctoral studies. Professor Rubinstein, I internalized the scientific method under your exceptional mentorship. Professor Foster, the lessons from your Praxis courses influence my engineering design decisions on a daily basis. Professor Grayson, I am eternally grateful for the mentorship and autonomy you provided me during my Masters research. Through your example, I have learned the value of investing in the next generation and think of you each time I bring on a summer student. Thank you for the expertise you passed on to me in cell culture, bioreactor design, and scientific writing.

To the many individuals and companies that went above and beyond to help make this work possible, thank you. Thanks to Keith and the folks at AVT for your help with RGP lens fabrication. Thanks to Gavin, Hannes, and the good folks at mb-microtec for your help in procuring the GTLS. Thanks to Danny from Mika Color for your impeccable service and rapid turn around on photomasks. Thanks to the wonderful members of the Caltech community.

To the industry, healthcare, and business advisors who shared their insights into the medical technology, venture capital, and public health fields with me: Karl, Bob, Chinmay, Paul, Omar, Tony, Damien, Ying, Darren, Jennifer, Yolie, Dr Indira, Julie, and others, thank you. I am grateful to have met each of you and for your generosity. To my colleagues, classmates, acquaintances, conference goers, and folks I have met along the way, thank you for always doing your best in whatever you pursue. I may not be able to specify exactly when, what, or how our interaction influenced this work, but I am sure it did. Giant shoulders and all.

Finally, thank you to my friends and family for your support, encouragement, and love throughout this process. You have been both my role models and champions over the years. This work is the culmination of the lessons and values you have taught me. I hope you enjoy it.

ABSTRACT

Diabetic retinopathy is a microvascular disease of the retina and a leading cause of vision loss worldwide. In the non-proliferative phase, diabetes-induced degradation of the retinal blood supply leads to edema and progressive tissue hypoxia. In response, the retinal tissue expresses proangiogenic growth factors (*e.g.* vascular endothelial growth factor), which drive proliferation of aberrant blood vessels within the eye. These poorly formed vessels leak fluid and blood cells into the eye and grow into the vitreous, which puts traction on the retina and leads to detachment. Given the hypoxic etiology, retinal oxygen tension and metabolism have received considerable attention. Dark-adapted conditions drive the retina to a significantly lower oxygen tension compared to light-adapted conditions as rod cells consume more energy in order to boost sensitivity. While tolerable in the healthy retina, it has been hypothesized that increased nightly metabolism overwhelms the compromised oxygen supply in the diabetic retina, leading to hypoxia and pathological vascular endothelial growth factor expression.

This thesis develops ocular devices that shine light onto the retina to modulate rod metabolism, reducing oxygen demand and mitigating nightly hypoxia. The *phototherapeutic* effect is characterized through mathematical modeling of retinal metabolism and *in vivo* testing. Implantable phototherapy devices are designed, fabricated, and evaluated. This thesis also develops overnight phototherapeutic contact lenses utilizing radioluminescence, chemiluminescence, and electroluminescence approaches. Phototherapy holds promise as a non-invasive, preventative therapy for the treatment of hypoxic retinal diseases such as diabetic retinopathy.

TABLE OF CONTENTS

LIST OF FIGURES

LIST OF TABLES

CHAPTER 1 : Diabetic Retinopathy and the Human Eye

Key Take-Aways
• Diabetic retinopathy is a leading cause of blindness, which affects over 100 million diabetics around the world. • Degradation of the retinal blood supply leads to oxygen deficiency within the retina, which drives pathological proliferation of new, poorly formed vessels. • Reduction of retinal metabolism through panretinal photocoagulation and/or interruption of the vascular endothelial growth factor signaling is therapeutic.

Epidemiology

Diabetes Mellitus (DM) is one of the world's fastest growing chronic diseases. The World Health Organization estimated that the total number of people with diabetes would double from 171 million in 2000 to 366 million by 2030. Alarmingly, these predictions have already been surpassed with more than 400 million people worldwide suffering from diabetes in 2015 (Figure 1.1).

Diabetes causes a number of complications in patients with diabetic retinopathy (DR) being one of the most significant. DR is a condition where damage occurs to the small blood vessels and neurons of the retina due to diabetes. DR is the leading cause of blindness in patients aged 20-74 years and affects 80-100% of people who have had diabetes for 20 years or more [1]–[3].

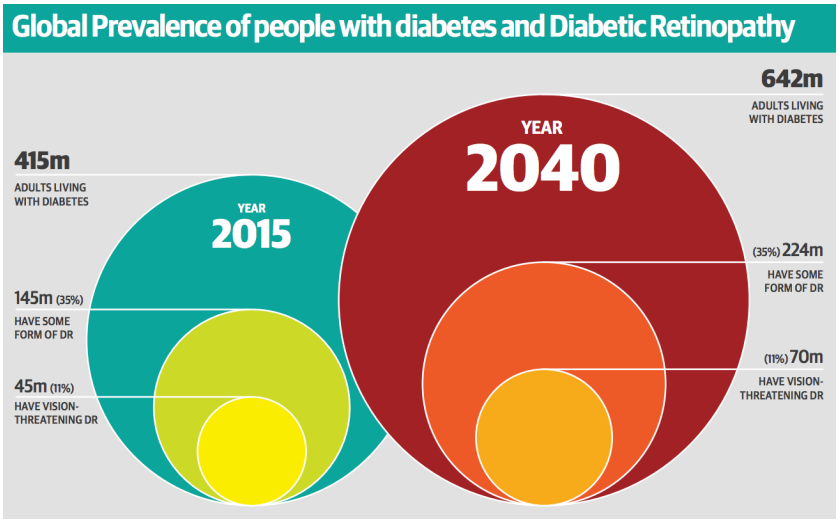

Figure 1.1: Global prevalence of diabetic retinopathy. Reprinted from [4].

It is estimated that over one-third of all diabetes patients worldwide have signs of DR, with the number of DR and vision-threatening DR (VTDR) cases expected to rise to 224 million and 70 million respectively by 2040 (Figure 1.2). Several factors drive this trend, including the increasing prevalence of diabetes due to dietary and lifestyle habits, increasing life expectancy of those with diabetes, and aging demographics, especially in developed countries [1], [4], [5].

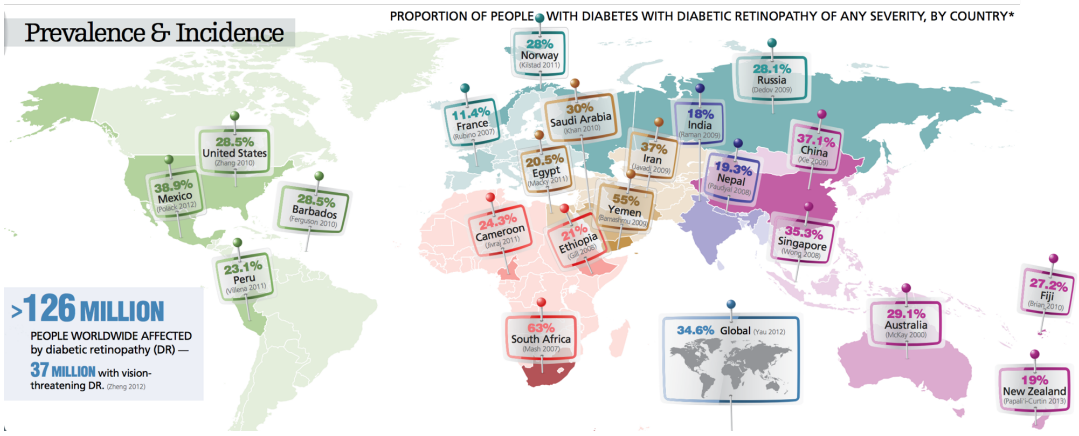

Figure 1.2: Regional incidence of diabetic retinopathy. Reprinted from [5].

Economic Burden

Diabetic retinopathy has a surprisingly large impact on the overall costs of diabetes care, including direct treatment costs as well as indirect costs (due to vision loss, such as lost wages, disability payments, rehabilitation counseling, transportation, residential care and caregiver costs). It has been estimated that the indirect costs of DR were ~ 3-fold greater than the direct costs [6]. Research predicts that effective prevention and treatment of diabetic retinopathy would result in annual savings of $600 million in the USA [3]. The healthcare costs also increase with the severity of DR (from mild NPDR to severe PDR) due to the increased cost of inpatient procedures [7]. Encouragingly, timely diagnosis and appropriate care can prevent up to 70% of diabetes-related visual impairment [3].

Classification

Diabetic retinopathy is a progressive disease. Clinicians commonly classify the disease according to the state of neovascularization, either non-proliferative or proliferative. Non-proliferative diabetic retinopathy (NPDR) characterizes the early stages of the disease and involves progressive alterations to blood vessels in the retina including occlusion, microaneurysms, and hemorrhages. Proliferative diabetic retinopathy (PDR) follows as hypoxia drives the ingrowth of new, often abnormally formed, blood vessels into the retina and vitreous of the eye. During NPDR, patients can still have 20/20 vision and symptoms are mild or non-existent, unless there is macular edema. Diabetic macular edema (DME) refers to the swelling of the region surrounding the center of the retina (*i.e.* the part of the retina that controls detailed vision). DME can

occur at any stage of DR, but it is more likely to happen as the disease progresses, ultimately causing total blindness. In contrast to NPDR, development of PDR represents a significant risk for blurred vision, significant vision loss (including blindness), scarring, retinal detachment, and the onset of glaucoma (damage to the optic nerve) [8].

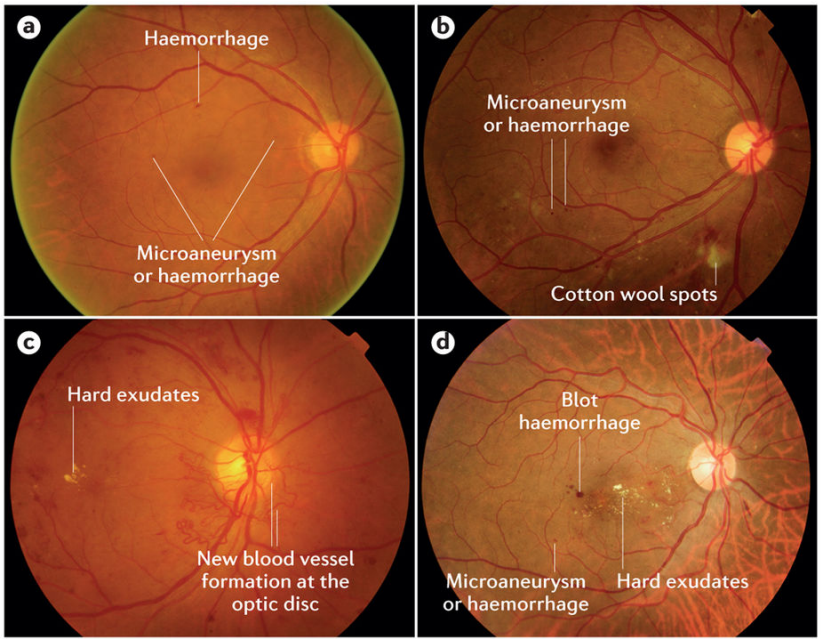

Figure 1.3: Stages of DR. a) Mild non-proliferative diabetic retinopathy (DR) with microaneurysms and hemorrhage. b) Moderate non-proliferative DR with microaneurysms, hemorrhage and cotton wool spots. c) Proliferative DR with new blood vessels at the optic disc. d) Diabetic macular edema with hard exudates at the fovea center. Reprinted from [8].

Risk Factors

The greatest risk factor for the development of diabetic retinopathy is the duration of diabetes [2]. The most important modifiable factor is glycemic control, which can reduce the rate of progression and incidence [9]–[11]. Table 1.1 summarizes other modifiable, non-modifiable and emerging risk factors [1], [12].

Table 1.1: Risk factors of diabetic retinopathy

Non-modifiable	Modifiable	Novel/Emerging
Duration of diabetes	Hyperglycemia	Inflammation
Puberty	Hypertension	Metabolic Hormones
Pregnancy	Hyperlipidemia	Oxidative Stress
Cataract Surgery	Obesity	Vitamin D deficiency
	Smoking	Genetic Risk Factors

Type 1 vs. Type 2 Diabetes Mellitus

Type 1 diabetes, also known as insulin-dependent diabetes mellitus (T1DM), is an autoimmune condition caused by the patient's body attacking its own pancreas and compromising insulin production. T1DM is associated with a genetic predisposition, and can also result from faulty beta-cells in the pancreas that are incapable of producing insulin. Another common name for T1DM, juvenile-onset diabetes, refers to the fact that it often begins in childhood.

Common names for type 2 diabetes mellitus (T2DM) include non-insulin dependent diabetes and adult-onset diabetes: this is the most common form of diabetes, accounting for roughly 90% of the cases in adults. In this condition, cells in the body become insulin-resistant, exceeding the capacity of the pancreas to produce insulin. Supplementing with exogenous insulin is effective in managing the disease. Sedentary lifestyle, improper diet, poor sleep habits, obesity, and stress are driving an increase of T2DM in teenagers [13].

The prevalence and incidence of DR in T1DM is much higher than T2DM (77.3% vs. 25.2%), although T2DM affects more people [1], [14]. Thus the proportion of cost associated with retinopathy is greater in T1DM compared to T2DM (Figure 1.4). This difference is in part due to the duration of diabetes in these patients, and recent studies

have shown a decline in the incidence of DR among those with T1DM due to increased awareness of risk factors, better glycemic control, and regular screening [1], [12].

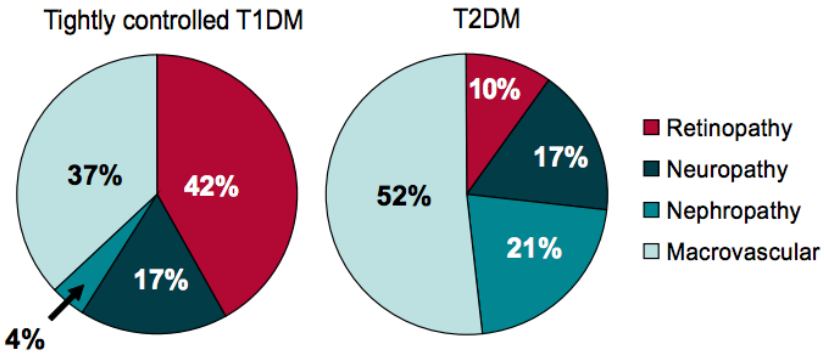

Figure 1.4: Relative contribution of complications to lifetime direct healthcare costs. Reprinted from [6].

In general, patients with T2DM in Western communities have a higher prevalence of DR than their Asian counterparts [1]. Many studies in Asia and the Middle East only include T2DM patients in their analysis due to the negligible fraction of T1DM in these ethnic groups. DR prevalence rate is highest in the USA followed by Europe.

Timeline of Diabetic Retinopathy Progression

The timeline for DR progression is highly variable and case-dependent; however, duration of diabetes seems to be one of the biggest risk factors affecting the onset of DR. Figure 1.5 shows the onset of DR in insulin-taking patients with a diagnosis of diabetes at age <30 years, as a function of duration of diabetes [15]. The probability of developing diabetic retinopathy reaches 80-100% within 10-15 years for patients, explaining the incidence in D1DM patients, who become insulin-dependent significantly younger [2]. Trends for patients diagnosed with diabetes at >30 years are similar [16].

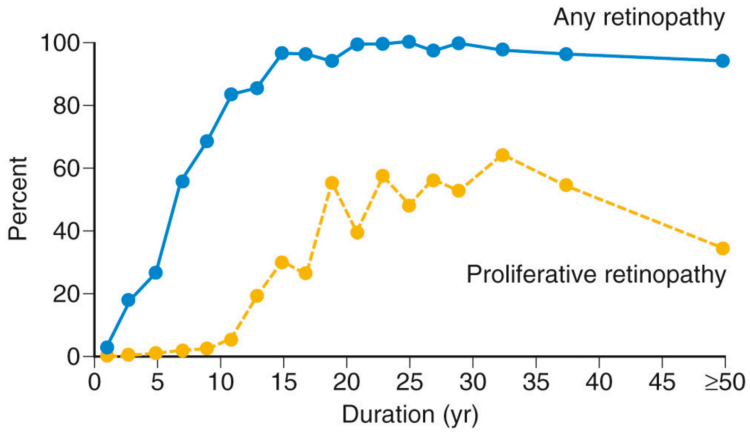

Figure 1.5: DR onset and progression in patients diagnosed with diabetes at <30 years old. Reprinted from [2].

Anatomy and Physiology of the Human Eye

Given that the eye is the organ that diabetic retinopathy affects, it is important to have a sense of its basic anatomy, physiology, and nomenclature (Figure 1.6) in order to understand the etiology of the disease as well as considerations for potential therapies. In humans, the eye is approximately 24 mm in diameter [17] with a spherical shape. A tough fibrous envelope, termed the sclera, surrounds the eye. The centrally located corneal tissue is transparent for light collection and protrudes slightly with a radius of curvature of approximately 8 mm. Three pairs of muscles, inserted into the sclera, allow for movement of the eye within its socket. Light entering the eye passes through several regions: cornea, aqueous humor, iris, lens, vitreous humor, and finally retina.

The cornea is an avascular tissue consisting of intricately arranged collagen fibers, which a sparse population of keratocytes maintains. It provides a clear optical opening into the rest of the eye. An outer layer of epithelial cells provides a barrier to bacteria

while an inner layer of endothelial cells maintains the hydration balance of the tissue. Lacrimal glands provide tears and mucus that is spread over the cornea through blinking. The cornea transitions continuously into the sclera. Table 1.2 summarizes key parameters of the cornea.

Table 1.2: Major corneal parameters in humans [18].

Area	$1.1cm^2$
Diameter	11.8mm (Horizontal) 10.6mm (Vertical)
Radius of Curvature	7.8mm (Anterior, Central) 6.5mm (Posterior, Central)
Thickness	0.54mm (Central) 0.67mm (Peripheral)
Refractive Index	1.376
Power	42D

The anterior chamber is the region below the cornea filled with aqueous humor, a transparent liquid that provides nutrients to the cornea and regulates intraocular pressure. The anterior chamber houses the iris, which is a thin, circular, and highly pigmented tissue that forms the pupil of the eye. A set of dilator muscles can pull on the iris radially to enlarge the pupil. The outer edge of pupil attaches to the anterior ciliary body and sclera. Just anterior of the iris is the important trabecular meshwork, which is responsible for drainage of aqueous humor back into the blood stream via the canal of Schlemm.

The lens of the eye is a biconvex structure consisting of a collagen lens capsule filled with high-refractive index crystallin proteins. Suspensory ligaments between the ciliary body and periphery of the lens capsule hold it just behind the iris and can change the shape of the lens and hence decrease or increase optical power through contraction or

relaxation of the ciliary muscles. The lens along with all anterior regions comprises the anterior segment of the eye.

The vitreous humor, retina, choroid, and optic nerve compose the posterior segment of the eye. The vitreous humor is a transparent collagen jelly composed mainly of water (98-99%) and surrounded by vitreous membrane.

The retina is a delicate and intricately layered tissue that is responsible for the transduction of light into electrical signals for the visual system. Moving inward from the sclera, the functional layers include [17]:

- the choroid, a dense vascular network that provides oxygen and nutrients to the outer retina;
- the pigmented epithelium, a layer of cells that contain high levels of melanin to absorb any photons that manage to pass through the photoreceptors;
- the photoreceptors, composed of rods (scotopic vision) and cones (photopic vision). Outer segments contain light-sensitive pigments and molecules involved in the phototransduction cascade; inner segments contain mitochondria, nuclei, and synapses to intermediate neurons;
- the intermediate neurons, composed of bipolar cells, horizontal cells, and amacrine cells responsible for processing signals from the photoreceptors and passing on to ganglion cells;
- the ganglion cell layer, neurons that transmit the electrical signals through the optic nerve fibre into the brain;

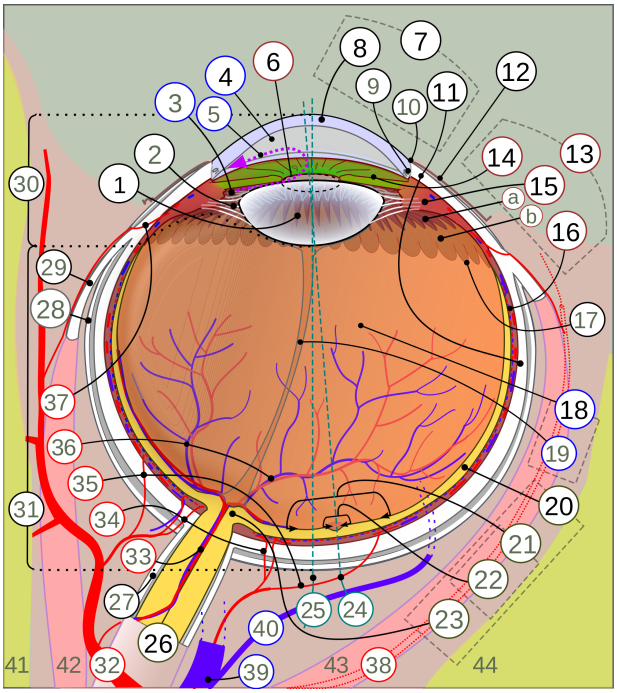

Figure 1.6: Anatomical overview of the eye. "1. Lens, 2. Zonule of Zinn or Ciliary zonule, 3. Posterior chamber and 4. Anterior chamber with 5. Aqueous humour flow; 6. Pupil, 7. Corneosclera or Fibrous tunic with 8. Cornea, 9. Trabecular meshwork and Schlemm's canal. 10. Corneal limbus and 11. Sclera; 12. Conjunctiva, 13. Uvea with 14. Iris, 15. Ciliary body (with a: pars plicata and b: pars plana) and 16. Choroid); 17. Ora serrata, 18. Vitreous humor with 19. Hyaloid canal/(old artery), 20. Retina with 21. Macula or macula lutea, 22. Fovea and 23 Optic disc → blind spot. 24. Optical axis of the eye. 25. Axis of eye. 26. Optic nerve with 27. Dural sheath, 28. Tenon's capsule or bulbar sheath, 29. Tendon. 30. Anterior segment, 31. Posterior segment. 32. Ophthalmic artery, 33. Artery and central retinal vein → 36. Blood vessels of the retina; Ciliary arteries (34. Short posterior ones, 35. Long posterior ones and 37. Anterior ones). 38. Lacrimal artery, 39. Ophthalmic vein, 40. Vorticose vein. 41. Ethmoid bone, 42. Medial rectus muscle, 43. Lateral rectus muscle, 44. Sphenoid bone." Reproduced from [19].

Macroscopically, the retina encompasses several regions (Figure 1.7) [17], [20]:

- the optic disc, the light-insensitive portion of the retina where the optic nerve pass through;
- the fovea, a small depressed area near the visual pole of highest visual acuity and cone density; the central region termed the faveola contains no blood vessels or rod cells;
- the parafovea, a region over which the photoreceptor layer thins to thicknesses observed around the rest of the retina;
- the perifovea, a region over which the ganglion layer thins from 4 cells to 1 cell;
- the peripheral area, the region between the parafovea and ora serrata;
- the ora serrata, the scalloped boundary of the retina near the front of the eye.

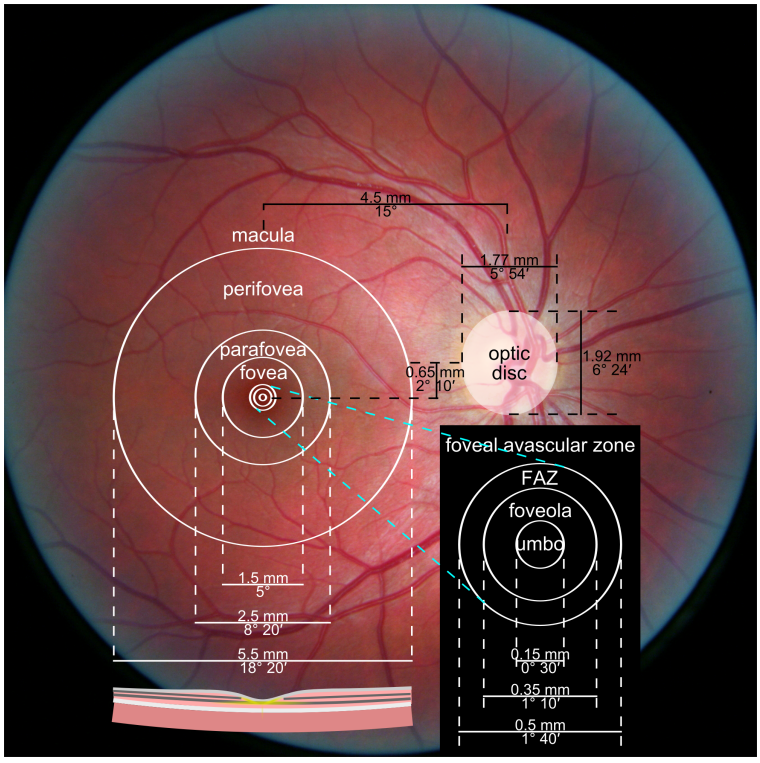

Figure 1.7: Regions of the retina with overlays indicating fovea, parafovea, perifovea, and macula. Reprinted from [21].

Vasculature of the Retina

As one of the most metabolically active tissues in the body, the retina has two distinct blood supplies [14]. Photoreceptors and pigmented epithelium (outer retina) sit on top of the non-autoregulated choroidal vasculature. Choroidal capillaries are broad, flat, and fenestrated, which allows for the passage of small molecules out of the vessels. A bi-layered retinal vasculature, composed of autoregulated superficial and deep capillaries, supplies the inner retina. Recent mapping of the retinal vessels using optical coherence tomography has improved understanding of vascular distribution [22]. The vessels have a very high ratio of pericyte to endothelial cells and form the blood-retinal barrier, which prevents non-transported molecules from reaching the retina.

In response to vascular insult, the retinal tissue can become hypoxic. The activation of a classic hypoxia inducible factor (HIF) pathway leads to angiogenic growth factor secretion, as well as the expression of survival factors and glycolytic enzymes. The prolyl hydroxylases involved in the cascade have a K_M for oxygen that is above atmospheric levels, so all changes in oxygen tension are transduced [23]. Key expressed proangiogenic growth factors include vascular endothelial growth factor (VEGF), erythropoietin (EPO), and stromal-derived growth factor 1 (SDF-1), along with many others of interest. VEGF in particular plays a role in the maintenance of the retinal vascular supply by stimulating growth and repair of blood vessels as well as increasing vascular permeability to enable cell extravasation. However, many diseases arise due to excessive production of VEGF, which can trigger pathological capillary growth and excessive permeability that can lead to tissue edema.

Etiology of Diabetic Retinopathy

In the non-proliferative phase of diabetic retinopathy there is progressive destruction of the retinal vasculature (*e.g.* occlusion of vessels, microaneurisms, nonperfusion), which leads to hypoxia (Figure 1.8). Other cells involved in maintaining the vasculature are also damaged and lost including pericytes, endothelial cells, Müller cells, and neurons. Inflammation of the tissue due to oxidative stress and hyperglycemia contribute to vessel loss, although the exact details are still under investigation.

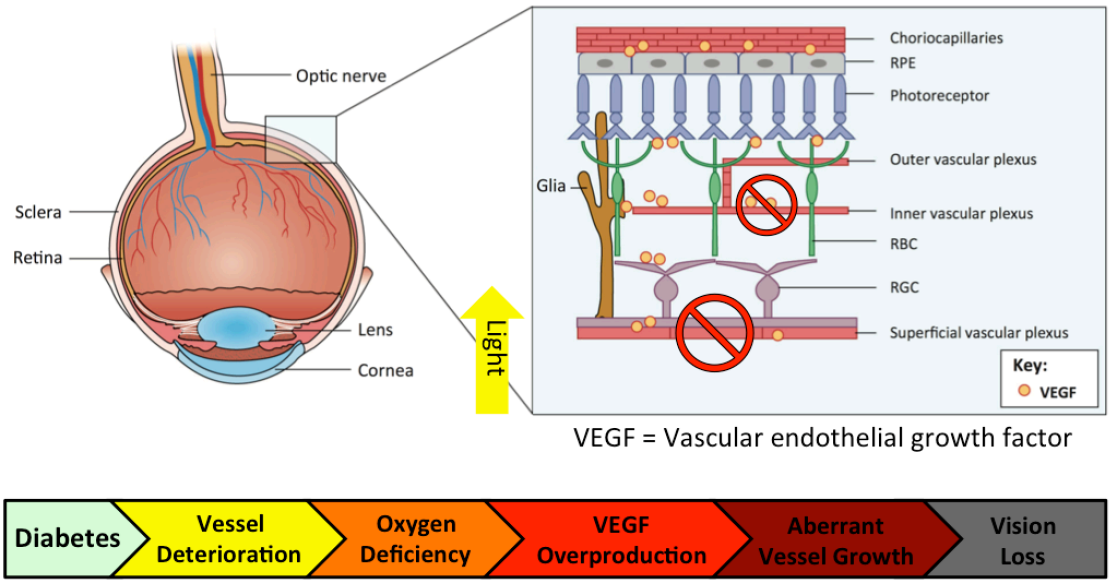

Figure 1.8: Hypoxic etiology of diabetic retinopathy. Adapted from [16].

After sufficient retinal vasculature degradation, the extensive hypoxia in the neurons and supporting astrocytes begins to drive aberrant neovascularization in the tissue. While other molecules are undoubtedly involved, VEGF represents a critical signalling molecule in diabetic retinopathy. Pharmacological blocking of VEGF provides immediate clinical benefits. Neovascularization of the superficial capillaries results in tortuous, leaky, and fragile vessels, which are prone to bleeding and fibrosis. Resulting

scarring can place traction on the retina, which lead to detachment. Furthermore, elevated VEGF can cause excessive vascular permeability resulting in retinal edema.

Oxygen and Diabetic Retinopathy

Capillary nonperfusion is a hallmark of diabetic retinopathy and results in ischemia and hypoxia that drive expression of proangiogenic growth factors, and lead to the proliferative phase of the disease [24]. Understanding the oxygen needs and characteristics of the retina is important for understanding how diabetic retinopathy progresses and what could be useful in stopping progression.

Under normal conditions, the oxygen tension in the inner retina is roughly 10-20 mmHg, while in the outer retina oxygen levels can drop from around 70 mmHg at the choroid to 0 mmHg in the photoreceptor inner segments in the dark [25], [26]. Thus in the dark, when photoreceptors are most metabolically active, oxygen may be siphoned from the inner retina to the photoreceptors with estimates of 7-15% [27]–[29] (Note: [27], [29] were carried out in macaque, which has been established as a good model for human retinal vasculature [30]). The oxygen uptake rate of the retina has been measured in humans to be "2.33 µl (O_2)/min or 1.42 ml (O_2)/min/100 g tissue blood" [31], which works out to 1.7 nmol/s/retina.

Interestingly, oxygen saturation has been found to be elevated in the vessels of the retina of patients with diabetic retinopathy:

- "control 63 ± 5%, mild non-proliferative DR 69 ± 7%, moderate non-proliferative DR 70 ± 5%, severe non-proliferative DR, 75 ± 5%, and proliferative DR 75 ± 8%" [32].

- "Oxygen saturation in the retinal arterioles of healthy volunteers was 93 ± 4% and 58 ± 6% in venules (mean ± SD, n=31). The corresponding values for all diabetic patients (n=20) were 101 ± 5% and 68 ± 7%" [33].
- "Increasing severity of retinal changes from no retinopathy to diabetic maculopathy was accompanied with increasing oxygen saturation in retinal venules and decreasing oxygen extraction, whereas proliferative diabetic retinopathy showed increased oxygen saturation in both retinal arterioles and venules to result in a normal oxygen extraction" [34].

These results suggest reduction in the efficiency of oxygen extraction by the retinal tissue, since metabolic needs are not expected to change in diabetes. Paired measurements of retinal blood flow and blood oxygenation in humans [35] enables the calculation of retinal oxygen uptake (Table 1.3). Retinal oxygen uptake is reduced by around 33% in patients with NPDR, amounting to a deficit of 0.62 nmol/s. Possible explanations for these results [32] are that occlusion or obliteration of capillaries reduces opportunity for gas exchange and formation of arterio-venous shunts shortens transport time [36]. There is also evidence that glycosylated hemoglobin (HbA1c) has significantly higher oxygen affinity (10×) compared to its unmodified form and could lead to reduced oxygen delivery. However, HbA1c only ranges from 6.4-12% in diabetics compared to 4-5.6% in healthy patients so differential oxygen affinity will not be a primary factor [37]. Furthermore, thickening of the capillary basement membrane reduces oxygen transfer efficiency to tissue [38]–[40]. Consistently, clinical trials have shown that vitreal oxygen tension is reduced in diabetic retinopathy (5.7 ± 0.7 mmHg) compared to healthy individuals (8.5 ± 0.6 mmHg) [41].

Table 1.3: Oxygen uptake in human retina in healthy and DR patients

	SO_2, venule (%)	SO_2, arteriole (%)	Total RBF (µL/min)	Retinal O_2 Uptake (nmol/s)	Difference (%)
Control	56.29 ± 4.7	92.9 ± 1.6	42.66 ± 7.5	1.87	N/A
NPDR	62.55 ± 5.7	94.74 ± 2.4	32.97 ± 9.2	1.25	33

Current Treatment Options

Given the hypoxic etiology of diabetic retinopathy, treatments seek to either reduce the hypoxia or block the pathological signalling cascade that it drives.

Laser Photocoagulation

Panretinal photocoagulation has been a mainstay in the treatment of diabetic retinopathy since its introduction in the 1950s [42]. Originally, clinicians used laser burns to seal leaky vessels in the peripheral retina to reduce macular edema; however, researchers soon realized that it is the reduction in retinal metabolism, as a result of the laser burns destroying tissue, that is therapeutic. Modern therapy therefore involves an array of laser burns across the peripheral retina (1200-1500 burns of 0.5 mm diameter) (Figure 1.9), which reduce metabolic demands in the outer retina by approximately 20% [43]. The macula is carefully avoided due to its role in high acuity vision. The cell-free burned regions provide pathways for oxygen to diffuse from the outer choroidal vasculature through to the inner retina where it can help compensate for reduced oxygen supply from the inner retinal blood vessels. VEGF levels decrease in patients after laser photocoagulation, highlighting how hypoxia drives disease progression via VEGF [44].

While panretinal photocoagulation generally leads to the arresting of the disease, it causes permanent reduction in peripheral vision acuity and contrast sensitivity. For this

reason, patients often put it off until they have begun to suffer central vision problems, many of which are irreversible. A major benefit of the therapy is that it is an effective and permanent solution, which makes it particularly attractive for patient groups with high compliance risk or accessibility challenges. Given the long history and extensive data on panretinal photocoagulation, it offers a tried and tested therapy for clinicians.

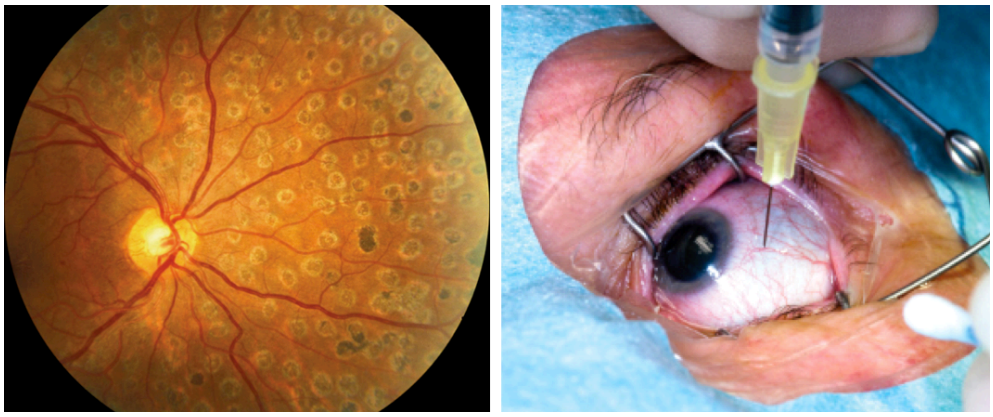

Figure 1.9: Interventions for diabetic retinopathy. (Left) Panretinal photocoagulation involves sacrificing a portion of the retina with an array of laser burns to reduce metabolic demand. (Right) Intravitreal injections of anti-VEGF drugs suppress neovascularization in the hypoxic retina and are given monthly to bi-monthly.

Anti-VEGF Injections

The emergence of VEGF as a driver of diabetic retinopathy led to design of anti-VEGF pharmaceuticals including ranibizumab (Lucentis) and aflibercept (Eylea) [45]. Monthly to bimonthly injection of these compounds into the vitreous of the eye causes regression of proliferative diabetic retinopathy and resolution of macular edema (Figure 1.9). Patient compliance however is often poor due to the discomfort associated with injections into the eye. The ongoing development of sustained release formulations aims

to reduce the frequency of injections. While effective managing diabetic retinopathy, chronic VEGF inhibition can result in loss of ganglion cells [46].

Hypoxic Diseases of the Eye

Beyond diabetic retinopathy, a number of retinal diseases with a hypoxic or VEGF-implicated etiology [14] exists and may benefit from similar treatments to diabetic retinopathy. Table 1.4 summarizes these benefits and highlights the magnitude of the problem.

Table 1.4: Retinal diseases that may benefit from reduced retinal hypoxia.

Disease	**Market Size**	**Rationale**
Diabetic Macular Edema	$3.71B globally (2017) [47]	Increased permeability due to VEGF expression in the retina leads to accumulation of fluid in the retina and swelling; increased thickness of the retina makes diffusion of oxygen less efficient leading to hypoxia
Glaucoma	$2.4B globally (2013) [48]	Increased capillary permeability due to VEGF expression in the retina leads to increased fluid entering the eye and increased pressure
Age-associated macular degeneration	$4B globally (2017) [49]	Drusen/plaque build-up between the outer blood supply and photoreceptors reduces oxygen diffusion
Retinal vein occlusion	$1.4B globally (2017) [50]	Blockage of blood flow leads to hypoxia in the retina
Retinal detachment	$2.6B globally (2023 estimate) [51]	When the retina detaches from the eye the photoreceptors lose blood supply so reducing their metabolism would be valuable while a tamponade is used to reattach the retina in proximity to the choroidal blood supply
Sickle-cell disease	No Data Available	Poor oxygen supply and increased likelihood of capillary occlusion leads to hypoxia in retina
Choroidal ischemia	No Data Available	Low oxygen delivery from the choroid leads to photoreceptor hypoxia
Retinopathy of Prematurity	No Data Available	Retinal hypoxia due to poorly developed Vasculature drives aberrant neovascularization [52]

Motivation for Preventative Therapies

Diabetic retinopathy represents a major and growing burden on the healthcare system. There is a desperate need for the development of preventative therapies to slow, stop, or even reverse disease progression. The following chapters outline the development of a new phototherapeutic technology that may be useful in conjunction with existing therapies to improve the outlook of diabetic retinopathy.

CHAPTER 2 : Photomodulation of Rod Metabolism

Key Take-Aways
• Rod metabolism is dominated by the circulating Na^+ (dark) current in the rod outer segment, which is reduced in light. • Photon absorption in rods reduces oxygen consumption by ~6000 O_2 per photon over the scotopic range of light intensity. • Phototherapy can improve retinal oxygenation similar to panretinal laser therapy.

Effect of Light on Retinal Metabolism

The transduction of photons into electrical signals enables human vision. The approximately 100 million rod cells of the retina [53] provide the high sensitivity phototransduction necessary for vision under low-light conditions. Due to the biochemistry of human vision, higher sensitivity requires greater energy expenditure. In the dark, rod cells burn considerably more energy to boost their sensitivity and allow us to perceive the faint scene. Unfortunately, the same expenditure occurs while sleeping in the dark, wastefully consuming oxygen and exacerbating retinal hypoxia.

The hypothesis that nightly rod-driven retinal hypoxia can be pathological was made by Dr Geoffrey Arden at least as early as 1998 [54]. As the retinal capillaries that oxygenate the inner retina are lost in diabetic retinopathy, the neural tissue becomes reliant on diffusion of oxygen from the (outer) choroidal vessels. During periods of illumination rod oxygen consumption is relatively low, allowing choroidal oxygen to reach the inner retina; however, during darkness (*e.g.* sleep) the increased rod metabolism

consumes virtually all of the choroidal oxygen causing the inner retina to become severely hypoxic. In response to oxygen deprivation, cells secrete proangiogenic growth factors, including VEGF, which initiates the proliferative phase of the disease by spurring the ingrowth of poorly formed, aberrant vessels that leak, bleed, and scar the tissue. The concept of phototherapy has been proposed wherein a nightly illumination on the retina tempers rod metabolism thereby saving choroidal oxygen for the de-vascularized inner retina.

The phototherapy approach is similar to panretinal photocoagulation in that it reduces the metabolism of the retina by around 20% and thus is likely to be similarly efficacious; however, it does so non-destructively and hence reversibly. While the concept of shining light onto the retina during sleep seems like it would be highly disturbing, the levels of light needed are quite low to suppress rod metabolism and because the illumination is constant the visual system quickly ignores it (Troxler effect). Mask-style phototherapeutic devices are under development in the UK by Polyphotonix and are undergoing evaluation [55]. This chapter explores aspects relevant to photomodulation of rod metabolism, laying the foundation for design of phototherapy devices.

Human Phototransduction Cascade

The rod outer segment is filled with lipid membrane discs packed with the components of the phototransduction cascade, providing a high probability of photon absorption. Several amplifying steps comprise the cascade, which enables the transduction of a single photon absorption event into a measurable electrical signal [56], [57]. Figure 2.1 summarizes the phototransduction cascade.

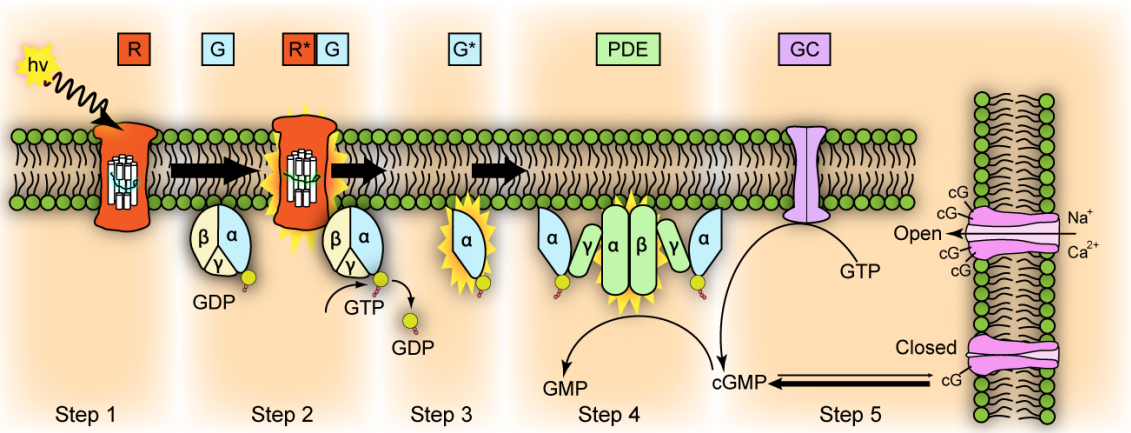

Figure 2.1: Summary of phototransduction cascade. Photon absorption by rhodopsin leads to protein activation, catalyzing the exchange of GDP for GTP in G-protein transducin. Consequently, the heterotrimer dissociates with its alpha subunit activating phosphodiesterase, which in turn hydrolyzes cGMP. Reduced cytoplasmic levels of cGMP cause the closure of gated sodium channels, reducing the influx of Na^+. Consequently, the cell hyperpolarizes leading to calcium channel closure, reduced intracellular Ca^{2+}, and reduced glutamate secretion. Reprinted from [56], [58].

Rhodopsin (R) is a key photosensitive protein composed of the membrane-bound protein scotopsin and covalently bound chromophore, retinal, responsible for the absorption of photons. The absorption of an incident photon causes the isomerization of retinal into all-trans-retinal, which results in the conformational change of rhodopsin to its active form metarhodopsin II (R*). This opsin interacts with transducins (G), a type of G protein, activating them by catalyzing the exchange of GDP for GTP. As a result, the heterotrimeric transducin dissociates, with its α subunit activating phosphodiesterase (PDE). Phosphodiesterase causes the breakdown of cGMP into 5'-GMP, leading to a drop in cGMP levels. cGMP-gated sodium channels then close leading to a reduction in

the sodium influx into the rod outer segment. However, since Na-K^+ ATPase in the rod inner segment continues to extrude Na^+, the cell hyperpolarizes. Voltage-gated calcium channels within the rod close in response to the hyperpolarization causing intracellular Ca^{2+} to drop. Neurotransmitter release from the rod slows, as the fusion of the glutamate containing vesicles to the cell membrane requires calcium. Reduced glutamate release causes depolarization of rod bipolar cells.

Metabolism of Phototransduction

In the dark, the rod cell supports a circulating sodium current that enters the outer segment via Na^+ channels and exits the inner segment via active extrusion by Na^+-K^+ ATPase [59]. Measurements of the current magnitude are on the order of 30 pA per rod cell [57], which requires an enormous energy expenditure to maintain, and accounts for the majority of overall rod metabolism [60], [61]. Given that a Na^+-K^+ ATPase requires 1 ATP to transport 3 Na^+ across the cell membrane, the energy expenditure per pA is:

$$\left(6.24\times10^{18}\,\frac{\mathrm{Na^+/s}}{\mathrm{A}}\right)\cdot(10^{-12}\mathrm{A/pA})\cdot\left(\frac{1\mathrm{ATP}}{3\mathrm{Na^+}}\right)=2.08\times10^{6}\,\frac{\mathrm{ATP/s}}{\mathrm{pA}}$$

Oxidative metabolism supplies most of the rod energy [62], requiring 1 O_2 molecule for every 6 ATP produced or $0.35\times10^{6}\,\frac{O_{2/s}}{pA}$. The literature provides a full accounting of rod metabolism and energy expenditure [60]. Figure 2.2 shows the total metabolic expenses amount to roughly $9\times10^{7}\,\frac{ATP/s}{rod}$ under dark adaptation and $2\times10^{7}\,\frac{ATP/s}{rod}$ under light adaptation. In practice, the presence of non-photoresponsive cells within the retina attenuates the stark contrast between light and dark-adapted retinal metabolism and oxygen levels.

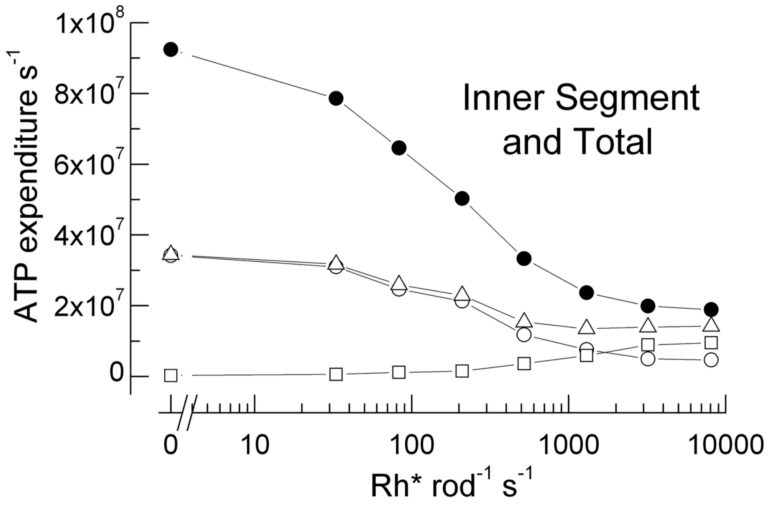

Figure 2.2: ATP expenditure in rod cell versus rhodopsin activation by light. "ATP required for extrusion of Na^+ entering through i_h channels (□), extrusion of Ca^{2+} entering voltage-gated channels at synaptic terminal (○), sum of ATP for Na^+ and Ca^{2+} extrusion (Δ), and sum of ATP turnover in whole rod (●)." Reprinted from [40].

Retinal oxygen profiles from a variety of non-primate and primate models have shown a significant reduction in retinal oxygen tension under dark adaptation and have quantified light-adapted and dark-adapted retinal metabolism (Table 2.1). Generally, it is only the outer retinal metabolism that changes significantly, while the inner retinal metabolism remains indifferent to illumination level [63].

Given that there are 100 million rod cells in the average human eye [53], the suppression of the rod dark current can provide considerable oxygen savings:

$$\frac{\Delta O_2}{\text{retina}} = \left(7\times10^7 \frac{\frac{\text{ATP}}{\text{s}}}{\text{rod}}\right)\left(\frac{1\ O_2}{6\ \text{ATP}}\right)\left(10^8 \frac{\text{rod}}{\text{retina}}\right)$$

$$\frac{\Delta O_2}{\text{retina}} = 1.1\times10^{15} \frac{O_2}{\text{retina}} = 1.9 \frac{\text{nmol}\ O_2}{\text{s}\cdot\text{retina}}$$

Therefore light can reduce retinal oxygen consumption by around 1.9 nmol/s.

Table 2.1: Retinal oxygen uptake differences under light and dark-adapted condition in macaque, rabbit, cat, bullfrog.

Species	Light Adapted	Dark Adapted	D / L Ratio	Reference
Macaque	Outer Retina: 4.6 ± 2.3 ml O_2 / 100g retina / min	Outer Retina: 6.4 ± 0.7 ml O_2 / 100g retina / min	1.4	[27]
Macaque *Macaca fascicularis* *Macaca nemestrina*	Outer Retina: *M. fasc.* 2.2 ± 1 ml O_2 / 100g retina / min *M. nem.* 2.6 ± 0.4 ml O_2 / 100g retina / min	Outer Retina: *M. fasc.* 3.1 ± 1 ml O_2 / 100g retina / min *M. nem.* 3.7 ± 0.6 ml O_2 / 100g retina / min	*M. fasc.* 1.4 *M. nem.* 1.4	[29]
Rabbit	93 ± 6 nmols / min	129±8 nmols / min	1.38	[62]
Cat	2 ml O_2 / 100g retina / min 1.4 ± 0.9 ml O_2 / 100g retina / min	6 ml O_2 / 100g retina / min 3.7 ± 1.5 ml O_2 / 100g retina / min	3 2.6	[64] [63]
Bullfrog	4.67 nmol/s/g	4.85 nmol/s/g	1.04	[65]

For comparison, consider the amount of oxygen being delivered to the retina through the retinal vasculature. Parameters from Table 2.2 enable calculation of oxygen supplied from the blood [66]:

$$s_{ox}\alpha_1 = bf \cdot m_{ret,in}\left[(p_{blood} - \beta_{ox}p)\alpha_1 + \left(\frac{p_{blood}^n}{p_{blood}^n + K_{hem}^n} - \frac{(\beta_{ox}p)^n}{(\beta_{ox}p)^n + K_{hem}^n}\right)Hb \cdot \delta\right]$$

$$s_{ox}\alpha_1 = \left(0.0066\frac{\text{mL}}{\text{g}\cdot\text{s}}\right)(0.137\text{g/retina})\left[(80-20\text{mmHg})\left(1.5\times10^{-6}\frac{\text{M}}{\text{mmHg}}\right)\right.$$

$$\left.+\left(\frac{80^{2.7}}{80^{2.7}+26^{2.7}}-\frac{20^{2.7}}{20^{2.7}+26^{2.7}}\right)\left(0.140\frac{\text{g}}{\text{mL}}\right)\cdot\left(0.0616\frac{\text{mmol}}{\text{g}}\right)\right]$$

$$s_{ox}\alpha_1 = 5\ \frac{\text{nmol O}_2}{\text{s}\cdot\text{retina}}$$

Therefore, the 1.9 $\frac{nmol\ O_2}{s\cdot retina}$ oxygen savings through suppression of the circulating dark current is comparable to 38% of the retinal blood supply.

Table 2.2: Retinal oxygen model parameters adapted from [44].

α_1	The solubility of oxygen in blood, a constant set to 1.5×10^{-3} (mM/mmHg)	[67]
α_2	The solubility of oxygen in retina, a constant set to 2.4×10^{-5} (ml O_2/ml tissue/mmHg)	[64]
β_{ox}	The ratio of the partial pressures of oxygen in venous blood and retina (at steady state), set to 1	
bf	Local blood flow in the inner retina , 0.0066 ml/g/s	[68]
D_{ox}	Diffusivity of oxygen in retina, 2×10^{-9} m^2/s	[69]
δ	The oxygen carrying capacity of hemoglobin, set to 0.0616 mmol/g	[70]
Hb	The hemoglobin concentration in blood, set to 140 g/L	[70]
K_{hem}	A constant which equals the partial pressure of oxygen at which hemoglobin is 50% saturated with oxygen, set to 26 mmHg	[71]
K_{ox}	The partial pressure of oxygen, at which the consumption runs at half maximal speed, set to 2 mmHg	[72]
n	Hill coefficient, set to 2.7	[71]
p	Local partial pressure of oxygen in retina 20 mmHg	[25]
p_{blood}	Partial pressure of oxygen in arterial blood 80 mmHg	[63]
$q_{ox,max}$	Maximal consumption rate of oxygen. Inner retina (26 mmHg/s independent of illumination) and inner segments (90 mmHg/s in light and 170 mmHg/s in darkness)	[63]
s_{ox}	The amount of oxygen per unit time transferred locally from the blood to retina mmHg/s	
$m_{ret,in}$	Inner retinal mass, 137 mg (from 1,094 mm^2 × 0.125 mm thick inner retina × 1 mg/mm^3)	[53][66]
$P_{choroid}$	Choroidal oxygen tension 55 mmHg	[25]

Energetics of Dark Current Suppression

In an individual rod, it takes around 600 photons/μm^2/s to achieve this suppression. Table 2.3 summarizes the relationship between light intensity and rod dark current suppression.

Table 2.3: Response of rod current to background illumination steps.

Species	Relationship with Illumination	Reference
Guinea pig rod cell; response to 5 s step in background light	$R(I) = \frac{I}{I + I_{50}}$ I_{50} = 325 photon/μm^2	[61]
Guinea pig rod cell; response to 5 s step in background light	$R(I) = R_{max}(1 - e^{-\frac{I}{K_s}})$ K_s = 387 photon/μm^2/s	[61]
Mouse	I_{50} = 120 photon/μm^2 (converted from 200 Rh*/rod/s)	[60]
Human, response to 4-6 s steps	$R(I) = R_{max}(1 - e^{-\frac{I}{K_s}})$ $K_s = \frac{1}{\tau(t)\cdot k} = 214$ to 739photon/μm^2/s $\tau(t)$ = 123 to 424 ms k = 0.011 μm^2/photon R_{max}= 13 pA	[73]

Then the oxygen savings per photon is:

$$\frac{\Delta O_2}{\text{photon}} = \frac{\left(7\times10^7 \frac{\text{ATP}}{\text{rod}\cdot\text{s}}\right)\left(\frac{1\ O_2}{6\ \text{ATP}}\right)}{\left(600\frac{\text{photons}}{\mu\text{m}^2\cdot\text{s}}\right)\left(3.1\frac{\mu\text{m}^2}{\text{rod}}\right)} = 6000\ \frac{O_2}{\text{photon}}$$

This calculation highlights the effectiveness by which light can modulate rod metabolism.

We can also compare the energy efficiency of photomodulation of rod oxygen consumption compared to the electrolysis of water to produce oxygen.

$$O_2(g) + 4H^+ + 4e^- \overset{1.23V}{\Longleftrightarrow} 2H_2O$$

$$E_{electrolysis} = (4e^-)(1.23V) \text{ per } O_2 = 4.92eV \text{ per } O_2$$

$$E_{photon} = \left(\frac{1.2398e\ V \cdot \mu m}{0.500\ \mu m}\right) \text{ per } 6000\ O_2 = 413\ \mu eV \text{ per } O_2$$

$$\frac{E_{hydrolysis}}{E_{photon}} = 11900\times$$

Therefore, the use of light to modulate oxygen consumption is $10^4\times$ more efficient than electrolysis and provides major benefits with respect to design since power considerations become minimal.

For suppression of rod circulating current the entire retina requires:

$$W_{photon,ret} = \phi A_{ret} = \left(600\ \frac{photons}{\mu m^2 \cdot s}\right)(1{,}094{,}000{,}000\ \mu m^2) = 7\times10^{11}\ \frac{photons}{s \cdot retina}$$

$$W_{photon,ret} = \left(7\times10^{11}\ \frac{photons}{s \cdot retina}\right)\left(\frac{1.2398\ eV \cdot \mu m}{0.500\ \mu m}\right)\left(1.6\times10^{-19}\frac{J}{eV}\right) = 280\ nW$$

An 8-hour period (*i.e.* duration of sleep) requires a total of 8 mJ for this illumination. Numerous powering strategies are suitable for providing such small amounts of energy.

Detailed Modeling of Phototherapeutic Effect

Modeling of retinal oxygen tension utilizing a four-layered, 1D model of the retina, modified from [63], [66], [74], aided in determining the therapeutic effect that phototherapy could have in alleviating hypoxia in diabetic retinopathy patients. The simulation (COMSOL Multiphysics) solves the diffusion equation:

$$\frac{dP}{dt} = \nabla(D_{ox}\nabla P) - q_{ox} + s_{ox}$$

where $q_{ox} = q_{ox,max}\frac{P}{P+K_{ox}}$ follows Michaelis-Menten kinetics for oxygen consumption and s_{ox} accounts for vascular oxygen supply as previously defined, included for inner retina only.

The retina subdivides into the following compartments from vitreous to choroid:

Inner retina: Accounts for 50% of retinal thickness. It contains the retinal vasculature providing a blood supply term s_{ox} that can be varied to account for vessel non-perfusion due to disease. Oxygen consumption is distributed over the inner retina, independent of illumination, and is due to ganglion cells, bipolar cells, Müller cells, and amacrine cells.

Outer nuclear layer: Accounts for 25% of retinal thickness. Contains the rod cell bodies but consumes little oxygen as energy is produced in the inner rod segments.

Inner rod segments: Accounts for 10% of retinal thickness. Contains most of the mitochondria supplying energy to the rod cell and therefore accounts for the vast majority of oxygen consumption. Oxygen consumption is dependent on illumination of the retina.

Outer rod segments: Accounts for 15% of retinal thickness. Responsible for the phototransduction cascade but consume little oxygen as energy is produced in the inner rod segments.

Regarding boundary conditions, the model assumes zero flux into the vitreous, justified by minimal oxygen gradient within vitreous, and a constant 55 mmHg at the choroid, since choroidal blood supply is robust and greatly exceeds retinal consumption.

A parameter sweep varying the retinal blood supply from 0.4 to 0 mL/g retina/min simulates the loss of blood flow due to diabetic retinopathy. Additionally, reducing oxygen consumption of the rod inner segments from 170 to 90 mmHg/s accounts for reduced metabolism under light/phototherapy/panretinal laser photocoagulation. Inner retinal metabolism remains constant at 26 mmHg/s. Panretinal laser photocoagulation involves 1200-1500 burns of 500 μm diameter (*i.e.* 20% of retinal area) and will reduce photoreceptors numbers and oxygen consumption accordingly [75],[76]. The model

postulates a 32% suppression of rod metabolism under phototherapy based on earlier estimates, though this can vary significantly depending on illumination intensity as reported by [60]. Further, since the mechanisms of action of the therapies are independent the model treats combination therapies as multiplicative. Figure 2.3 depicts how blood flow and intervention affect the retinal oxygen profile.

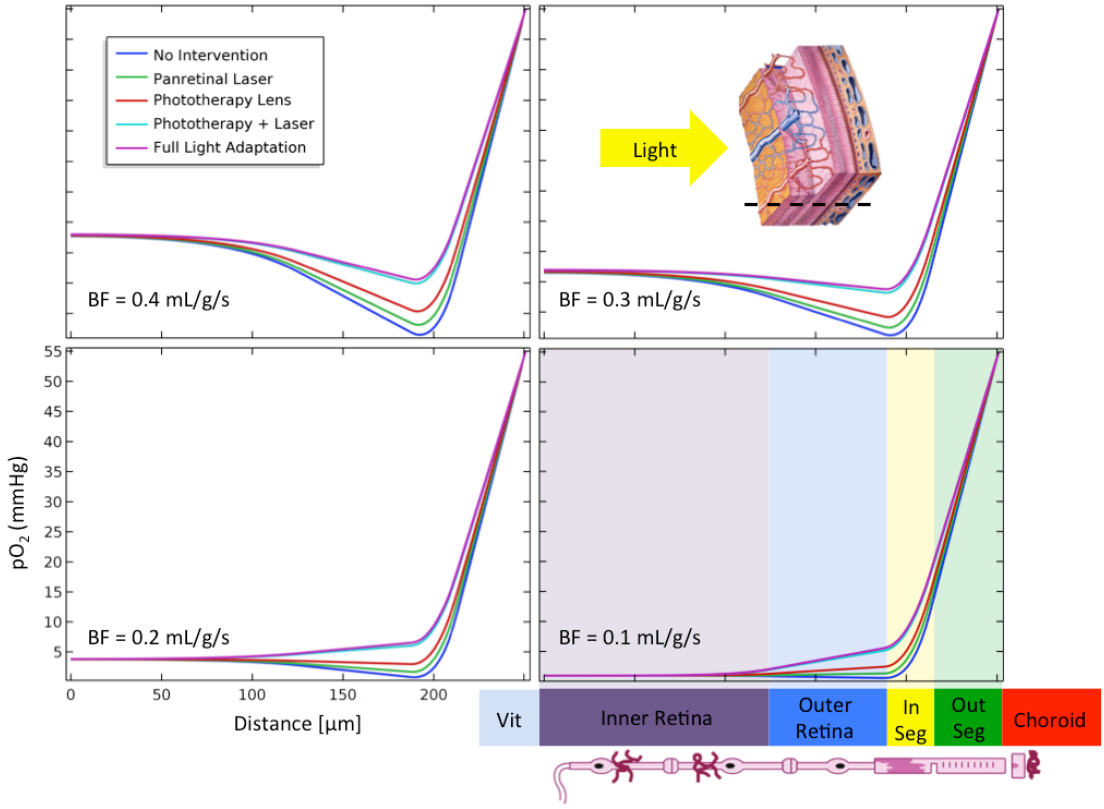

Figure 2.3: Simulated effect of blood flow and intervention on retinal oxygen tension. Inner segment metabolism: dark adaptation (q_{max} = 170 mmHg/s), panretinal laser (q_{max} = 136 mmHg), phototherapy lens (q_{max} = 116mmHg), phototherapy + panretinal laser (q_{max} = 92 mmHg), and light adaptation (q_{max} = 90 mmHg). Inner retinal metabolism: q_{max} = 26 mmHg/s. Michaelis-Menten constant for cellular oxygen uptake: K_M = 2 mmHg. No flux assumed at vitreous while choroid held at 55 mmHg.

Since the choroid is relatively resistant to degradation in diabetic retinopathy, most of the hypoxia driving the disease likely arises in the inner retina, which suffers from a progressively degraded blood supply. Given that the inner retina is supplied from the retinal vasculature while the outer retina is supplied by the choroid, it may not be initially obvious how the suppression of photoreceptor metabolism can improve inner retinal oxygenation. Researchers hypothesize that, analogous to the mechanism of action of panretinal photocoagulation, reducing rod metabolism can mitigate siphoning of oxygen from the inner retina or allow choroidal oxygen to reach the inner retina [75]. To this end, Figure 2.4 plots the oxygen flux through the outer nuclear layer of the retina.

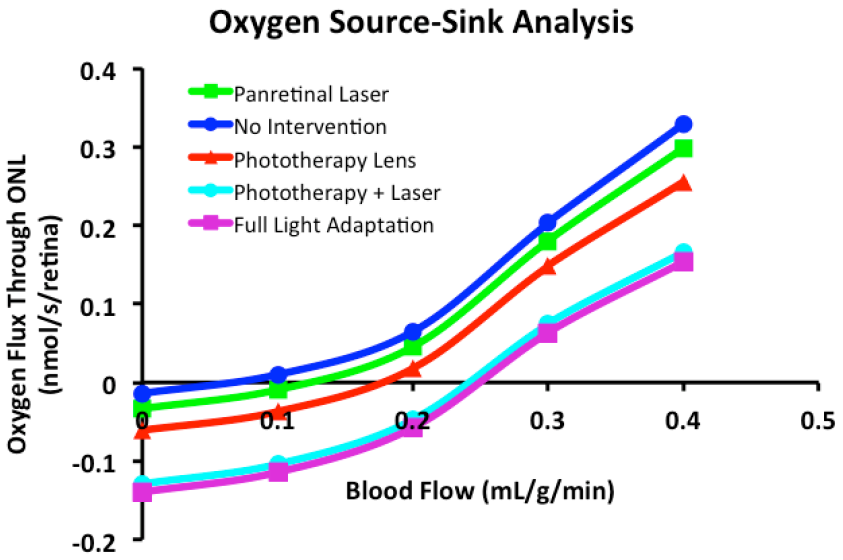

Figure 2.4: Oxygen flux through outer nuclear layer (ONL) / outer retina as a function of retinal blood supply and intervention. Positive values indicate that photoreceptors are siphoning inner retinal oxygen while negative values indicate choroidal oxygen is reaching the inner retina.

Based on these simulations, it becomes apparent that both mechanisms of action are possible depending on the degree of retinal blood flow and the metabolic state of the rod cells. The difference in oxygen flux between light and dark conditions is approximately 0.15 nmol/s, which is relatively small compared to total inner retinal blood supply in a healthy retina (~5 nmol/s in this model) but comparable to the clinically measured oxygen deficit in diabetics of 0.62 nmol/s [35]. Alternatively, consider that panretinal laser photocoagulation is therapeutically effective and it improves oxygen flux by only 0.03 nmol/s in this model; thus, the 0.07 nmol/s savings from a phototherapy lens is relatively significant.

Coupling of 1D Model with VEGF Expression

There is strong evidence in the literature that VEGF mediates the transition to proliferative diabetic retinopathy by driving the aberrant growth of blood vessels, primarily in the inner retina [77], [78]. The prolyl hydroxylase of the HIF signaling cascade, which is responsible for the transduction of oxygen tension to angiogenic gene expression, has a Michaelis constant for oxygen greater than atmosphere ($K_M > P_{O2}$) so there is a monotonically increasing relationship between physiological oxygen and HIF signaling [23]. The rate of VEGF secretion, driven by HIF, roughly follows a power law in humans dependent on the local oxygen tension (Table 2.4).

Table 2.4: Relationship between VEGF secretion and oxygen tension.

Model	Relationship	Comment	Reference
Human lymphocytes	$V_{VEGF} = \left(\frac{40mmHg}{P_{O_2}}\right)^{0.49}$	Used in simulations. Low exponent value makes this most conservative.	[79]
HeLa cells	$V_{VEGF} = \left(\frac{50mmHg}{P_{O_2}}\right)^{0.84}$	None.	[80]
Glial (Müller) cells from ex vivo rabbit retina	$V_{VEGF} = \begin{cases} 1.25mmol\ Glu, \left(\frac{206mmHg}{P_{O_2}}\right)^{0.94} \\ 5mmol\ Glu, \left(\frac{76mmHg}{P_{O_2}}\right)^{1.77} \\ 10mmol\ Glu, \left(\frac{188mmHg}{P_{O_2}}\right)^{0.88} \end{cases}$	Values extracted from paper by curve fitting; each glucose concentration only had 2 oxygen data points.	[81]

The weighting of retinal oxygen profiles by their likelihood to induce VEGF secretion allows for comparisons between interventions. Figure 2.5 plots the relative amount of total VEGF production expected as a function of light conditions and disease progression. Loss of blood flow in the inner retina functions as a proxy of disease progression in this model.

From the plot, it can be seen that with phototherapy a patient could sustain nearly 20% loss of retinal vasculature before VEGF levels reached levels experienced by healthy individuals during sleep (which are known to be safe). This result gives an indication of the therapeutic value of the light in modulating oxygen consumption, hypoxia, and VEGF secretion.

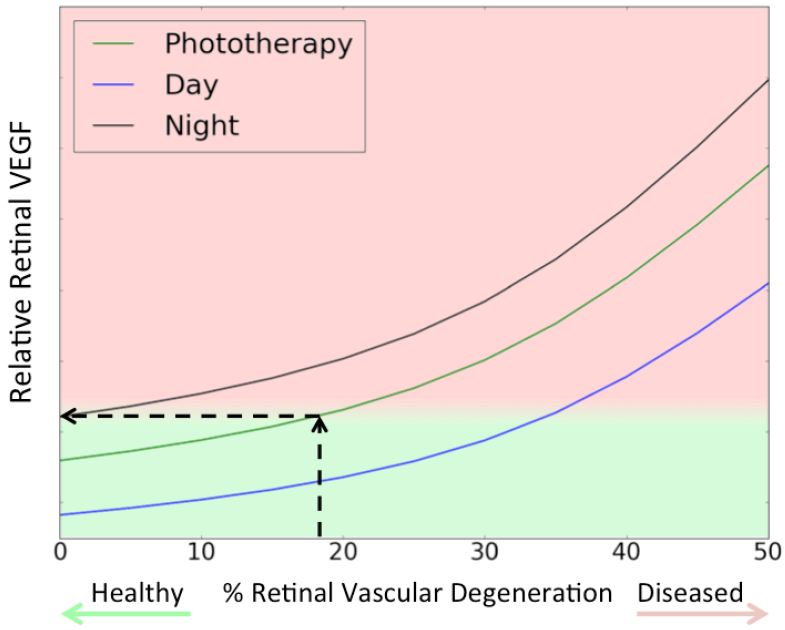

Figure 2.5: Relative VEGF expression in the retina as a function of retinal vascular degeneration and light intensity. Overlaid dashed arrows indicate that a patient treated with phototherapy can sustain nearly 20% retinal vascular loss, while maintaining tolerable VEGF levels (i.e. equal to those seen in a healthy individual at night).

It should be noted that this model is a first approximation and does not account for different hypoxia thresholds among cell types in the retina. Retinal staining for VEGF in enucleated eyes suffering from proliferative diabetic retinopathy found localization of VEGF expression primarily within the inner retina [82].

Absorbance Spectrum of Rod Cell, Emission Spectrum of Light Source

Rod and cone absorbance vary as a function of incident light wavelength [83]. For rod cells, the key pigment is rhodopsin, which has a peak absorbance of 491 to 505nm with a mean of 498 ± 3 nm (S.D) and a full-width half maximal of 104 nm. The probability of absorbance of a photon of a given wavelength is then the product of the

relative absorbance at the given wavelength and the quantum efficiency of the chromophore or overall rod cell. Since light sources and phosphors emit with a distribution of wavelength, integrating the product of the relative emission curve E(λ) and the chromophore absorbance curve A(λ) provides the average absorbance probability P:

$$P = \int A(\lambda) \cdot E(\lambda) d\lambda$$

Example plots for a green and iceblue emitting phosphor are depicted in Figure 2.6, highlighting the efficiency loss due to emission with off-peak absorbance wavelength.

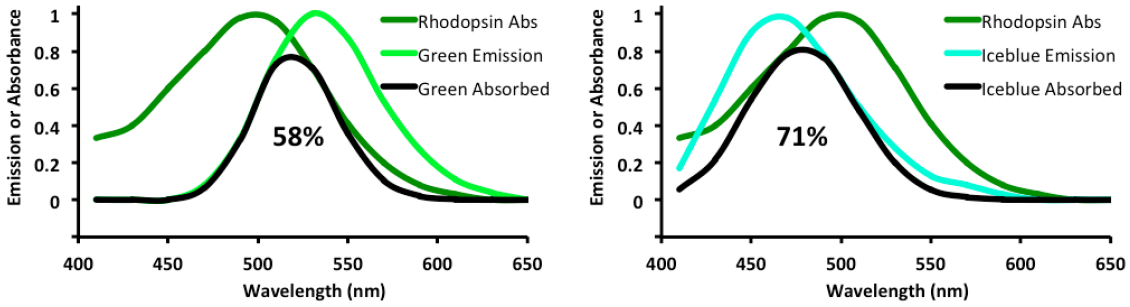

Figure 2.6: Absorbance spectrum of rhodopsin, emission spectra of green and iceblue phosphors, and their respective probability products with integrated average probability inlaid.

Quantum Efficiency of Eye

An important parameter in calculating the necessary photon flux density for the suppression of rod metabolism is the quantum efficiency of the rod. It accounts for the fact that rhodopsin does not absorb each photon incident on the retina. The mean number of photon absorptions, m [Rh^*/rod] is proportional to the light intensity, I [photons/μm^2], and the effective collection area, A_{eff} [μm^2] of the outer segment [84]:

$$m = A_{eff} \cdot I$$

For light incident parallel to the rod outer segment, the effective collection area is the cross-sectional area of the rod (including a focusing factor F, which accounts for a larger collection aperture of the inner segments compared to the outer segments) times the probability of photon absorption, which is the product of the quantum efficiency of isomerization Q_{isom}, a factor f that accounts for the relative efficiency of absorption for axial light (f=1) versus transverse light (f ≈ 0.5) with respect to the rod (and chromophores) [85], and absorbed photons fraction based on a specific axial pigment density α [μm^{-2}]:

$$A_{eff} = (\pi r^2 F)\left(Q_{isom} V(\lambda)\left[1 - 10^{-f\alpha L}\right]\right)$$

$$A_{eff,500nm} = \left(\pi(1\mu m)^2(2)\right)\left((0.67)(0.98)[1 - 10^{-1\cdot 0.016\cdot 25}]\right) = 2.5\,\frac{\mu m^2}{rod}$$

Thus at a photon flux density of 1 photon/μm^2/s isomerization will occur at 2.5 Rh^*/rod/s. Note that this analysis assumes photon flux density at photoreceptors and therefore does not include the pre-retinal transmittance.

Table 2.5: Parameters for quantum efficiency of the eye.

r	Rod radius, human, 1 μm 0.65 μm	[73] [14]
L	Rod outer segment length, 20-25 μm 25-45 μm	[73] [14]
F	Focusing factor, approximately 2	[73], [86]
Q_{isom}	Quantum efficiency of isomerization, 0.67	[87]
α	Specific axial pigment density, 0.016 μm^{-1}	[85]
f	Light orientation factor, axial = 1, transverse ≈ 0.5	[85]
V(λ)	Scotopic luminosity function, 0.98 @ 500 nm	[88]
$T_{pre\text{-}ret}$	Pre-retinal transmittance, 0.69 0.75	[89] [90].

A similar process as above can be carried out for transverse light (*i.e.* perpendicular to the rod) without the focus factor F; however, the absorbed fraction needs to be integrated due

to the varying path lengths across the circular body. The calculation can be simplified using a Taylor expansion so long as $f\alpha d \ll 1$ (*i.e.* negligible self-screening):

$$A_{eff,transverse} = \pi r^2 l Q_{isom} V(\lambda) \ln(10) f\alpha$$

Troland Definition and Conversion

For a given scene, the amount of light entering the eye is proportional to the area of the pupil. The *troland* unit, T, accounts for this proportionality:

$$T = L_v \cdot p$$

L_v is the luminance [lm/sr/m^2 = cd/m^2] of the scene and p is the area of the pupil [mm^2].

Conversion of Luminance to Retinal Photon Flux Irradiance

In many instances, it is useful to convert an object of a given luminance into a photon flux irradiance on the retina. Starting from the luminance L_v $\left[\frac{lm}{sr \cdot m^2}\right]$, convert to radiance L_e $\left[\frac{W}{sr \cdot m^2}\right]$:

$$L_e = \frac{L_v}{K_m' \cdot V'(\lambda)},$$

$K_m' = 1700 \frac{lm}{W}$ is the scotopic luminous efficacy (507nm). Then convert to photon flux radiance L_p $\left[\frac{photons/s}{sr \cdot m^2}\right]$ by dividing through by the energy per photon:

$$E_{photon} = \frac{hc}{\lambda} = \frac{1.986 \times 10^{-25}\ J \cdot m}{\lambda\ [m] \cdot photon}$$

$$L_p = \frac{L_e}{E_{photon}} = 5.03 \times 10^{24} \cdot \lambda[m] \cdot L_e = (2.96 \times 10^{21} \cdot \lambda[m]\ ) \frac{L_v}{V'(\lambda)}$$

Table 2.6: Constants of light.

h	Planck constant	6.626×10^{-34} [J·s]	[91]
c	Speed of light	299792458 [m/s]	[92]

The photon flux at the pupil $P_p\left[\frac{\text{photons}}{s}\right]$, given the area of the source $A_s[m^2]$, area of the pupil $A_p[m^2]$, and distance from the source D_s [m] is:

$$P_p = \frac{L_p A_s A_p}{{D_s}^2}$$

Using a simplified model of the eye optics with a posterior nodal distance, D_r, of 16.67 mm [93], the area of the object image on the retina is:

$$A_r = \frac{{D_r}^2 A_s}{{D_s}^2}$$

For a complete treatment of the theoretical eye see [94]. Then the retinal flux irradiance $E_p\left[\frac{\text{photons}}{s\cdot m^2}\right]$ is:

$$E_p = T\frac{P_p}{A_r} = T\frac{L_p A_p}{{D_r}^2}$$

T is the pre-retinal transmittance.

For a screen of luminance L, the ratio of retinal flux irradiance when the subject views the screen at a distance (*i.e.* through normal eye optics) versus through a closed eyelid at close proximity is:

$$\frac{E_{distance}}{E_{eyelid}} = \frac{T_{eye}\frac{L_p A_p}{{D_r}^2}}{\frac{T_{lid}\cdot T_{eye}\cdot L_p\cdot A_p}{D_{eye}^2}} = \frac{D_{eye}^2}{T_{lid}\cdot {D_r}^2} = \frac{(24mm)^2}{0.01\cdot(16.67mm)^2} \cong 200$$

This formula is useful for converting between luminance values under typical experimental conditions versus the less common situation of light emitting sleep masks.

Analysis of Phototherapeutic Sleep Mask Failure

The only preventive phototherapy-based device currently reported in the literature is the Noctura 400 sleep mask, which Polyphotonix (UK) produces and has recently completed Phase III clinical trials [95]. The mask features organic LED patches over each eye with onboard battery and circuitry to monitor wear. The device is intended to deliver light through the eyelid and onto the retina. While previous smaller studies with the mask showed some promise (*e.g.* reduced retinal edema, improved visual acuity, reduced bleeding) [45], [54], [96]–[100] the larger Phase III ultimately showed no therapeutic effect. Furthermore, patient compliance with the light emitting sleep mask was reported as only 19.5% after 2 years (39.5% at 4 months). The analysis in this section will look at probable reasons the sleep mask style device failed and suggest ways of overcoming those challenges.

Figure 2.7: Noctura 400 phototherapeutic sleep mask [55].

Calculation of Approximate Retinal Irradiance from Noctura 400

According to the manufacturer of the Noctura 400 sleep mask, it emits 186 scotopic cd/m^2 at 505 nm with the aim to achieve a 40% reduction in rod-circulating current (retinal irradiance of 100 photons/μm^2/s). Knowing these parameters, it is possible to infer the other assumptions they made about the optics of the eye during sleep. The retinal irradiance resulting from light emitted from a mask, that passes through an attenuating eyelid, a forward gazing pupil, and absorbing media of the eye is:

$$E_p = \frac{T_{lid} \cdot T_{eye} \cdot L_p \cdot A_p}{D_{eye}^2} = \frac{T_{lid} \cdot T_{eye} \left(5.03\times10^{15} \cdot \lambda \cdot \frac{L_v}{K_m{}' \cdot V'(\lambda)}\right) \cdot A_p}{D_{eye}^2}$$

If we assume D_{eye} = 24 mm, $T_{lid} = 10^{-2}$ [99], T_{eye} = 0.69 [89], A_p = 28 mm^2 (a 6 mm diameter pupil) we find:

$$E_p = \frac{0.01 \cdot 0.69 \cdot \left(5.03\times10^{24} \cdot 505\times10^{-9} \cdot \frac{186}{1700 \cdot 0.99}\right) \cdot 28}{(24)^2} = 94 \ \frac{\text{photons}}{\text{s} \cdot \mu\text{m}^2}$$

This finding suggests that the designers of the Noctura 400 assumed a dilated pupil and relatively high eyelid transmittance. However, these assumptions are not valid as discussed below and may be the reason the sleep mask failed to be efficacious in trials.

Factor 1: Variability in the Transmissivity of the Eyelid and Pupil Dilation

The transmissivity of the human eyelid is varies over an order of magnitude across the population from about 10^{-2} to 10^{-3} at 505 nm (Figure 2.8) [101]. This variation means that if the mask was designed assuming an eyelid transmissivity of 10^{-2}, then it will be significantly less efficacious for patients with eyelid transmissivity below this. The large range of eyelid transmissivity would require personalized testing and calibration for each patient but this was not done.

A second source of variability arises due to differences in the diameter of the dark-adapted pupil across the population. It is known to vary by a factor of 4 in area from 12.5 to 50 mm^2 [102]. However, the assumption of a dilated pupil during sleep is likely incorrect altogether as explained below.

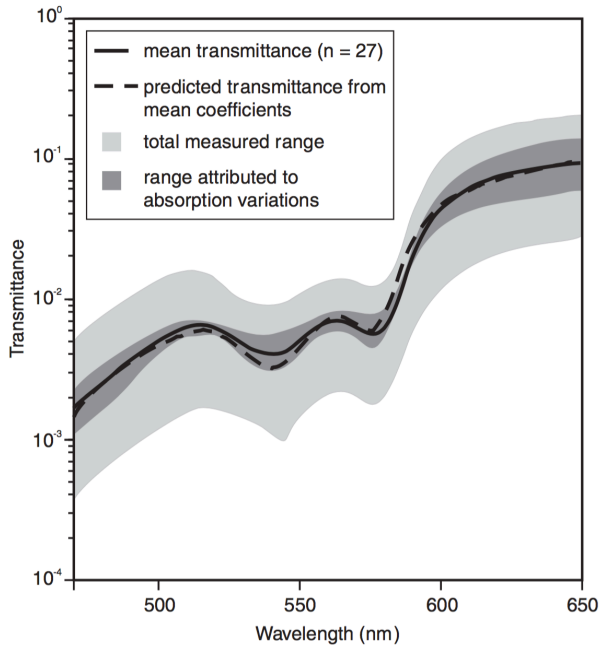

Figure 2.8: Range of transmittance of human eyelid over visible spectrum. Reproduced from [77].

Factor 2: Pupil Constriction During Sleep

Though not common knowledge even among ophthalmologists, the pupil actually constricts progressively the deeper the sleep [103], including during REM [104]. This process restricts the aperture for light to enter the eye even during forward gaze. In the limited studies that have looked at pupil size during sleep, one monitoring children ages 1 to 5 found that the average pupil diameter during deep sleep was 2.1 ± 0.5 mm while under dark-adapted awake conditions it was 6.1 ± 0.9 mm [103]. This reduction in pupil area during deep sleep would result in a retinal flux reduction to 11% of the dilated state.

The pupil in older (61 ± 4.4 y) patients tends to be more constricted compared to younger (22.8 ± 4 y) individuals under both conditions of light-adaptation (65% relative area) and dark-adaptation (73% relative area) [105]. Therefore, the effect of pupillary constriction in an elderly population is expected to be comparable or worse.

Factor 3: Bell's Phenomenon, Upward Gaze Angle During Sleep

A compounding factor is that during sleep, the eye has a tendency to roll upwards in the socket and therefore away from the light emitting sources. During drowsiness and Stage 1 of sleep the eyes deviates upwards from a forward gaze significantly (up to 40°), during Stage 2, 3, 4 the gaze is elevated 55-85% of the time (0-20°: ~1/4, 20-40°: ~1/2, >40°: ~1/4), and during REM a forward or below forward gaze is typical [106]. Thus photon flux density at the retina will reduce accordingly.

The transmittance will decrease significantly due to the additional thickness of eyelid that the light must pass through. Anatomically, the eyelid narrows towards the lashes and thickens towards the brow. As a conservative first approximation, assume that the path length through the eyelid is $t(\theta) = t_0/\cos(\theta)$. The transmissivity is then:

$$T(\theta) = 10^{\frac{\log(T_0)}{t_0}\frac{t_0}{\cos(\theta)}} = 10^{\frac{\log(T_0)}{\cos(\theta)}} = T_0^{\frac{1}{\cos(\theta)}}$$

For $T_0 = 0.01$:

$$T(40°) = 10^{\frac{\log(0.01)}{\cos(40°)}} = 0.0024$$

The amount of light reaching the pupil will also decrease due to the geometry of the system. The governing equation for radiative transfer is:

$$d\Phi = L \cdot dA_1 \cdot \cos(\theta_1) \cdot \frac{dA_2 \cdot \cos(\theta_2)}{\rho^2}$$

A is an area, θ is the angle between surface normal and the line-of-sight between surfaces, and L is the radiance of the emitting surface [107]. As the gaze angle increases both the effective surface area of the emitter and the solid angle of the receiving pupil decrease. Furthermore, the thickness of eyelid that light must transmit through increases. Utilizing a simplified 2D geometry for the eye and Noctura 400 phototherapy sleep mask, shown in Figure 2.9, the relative amount of light transmitted as a function of gaze angle was calculated and plotted in Figure 2.10.

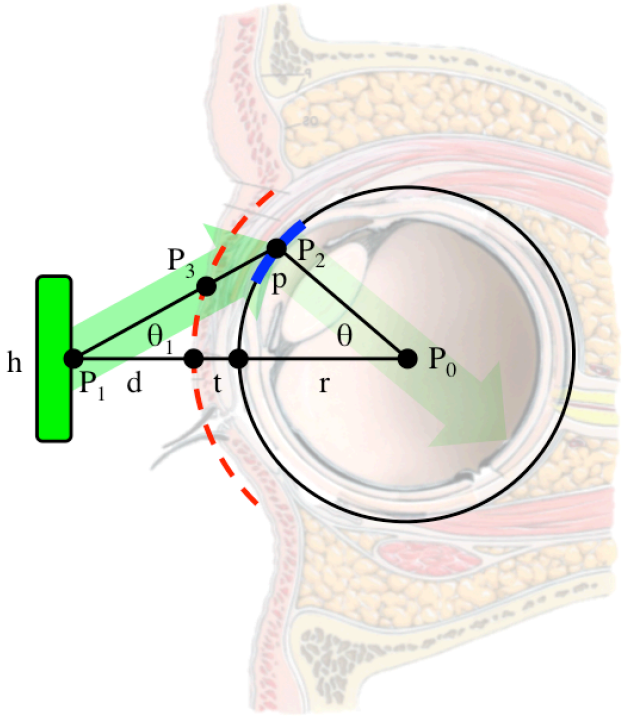

Figure 2.9: Schematic of Noctura 400 light emitting sleep mask optics and geometry of retinal illumination. Overlays on anatomical cross section of human eye indicate simplified eyelid of thickness t (red, dash), pupil of arc length p (blue, bold), eyeball of radius r and gaze angle θ (black circle), OLED of height h at a distance d away from the eye, and primary optical path P_1 to P_2 with eyelid transmission through P_3 to P_2.

Calculation of Retinal Irradiance Versus Gaze Angle

Table 2.7 summarizes the relevant parameters used in the calculation of retinal irradiance versus gaze angle.

Table 2.7: Parameters of calculation for Noctura 400 light emitting sleep mask optics and geometry of retinal illumination.

Symbol	Description	Value
P_i	0: Point at center of eye 1: Point on OLED 2: Point on pupil 3: Intersection point on eyelid	
θ	Gaze angle	0 to 50°
p_0	Arc length of pupil	6mm
h_0	Height of OLED	12.7mm
w_0	Width of OLED	19mm
d_0	Nearest distance of OLED to eyelid	5mm
t_0	Thickness of eyelid	0.5mm
r_0	Radius of eye	12mm
T_0	Transmissivity of eyelid	0.01 at 0.5mm thick

Briefly, the point of illumination was parameterized by h and defined as:

$$P_1: \begin{matrix} x_1 = 0 \\ y_1 = h \end{matrix}$$

The point of the pupil receiving light was parameterized by arc length p and defined as:

$$\theta_p = \frac{p}{r_0}$$

$$P_2: \begin{matrix} x_2 = d_0 + t_0 + r_0\left[1 - \cos\left(\theta + \theta_p\right)\right] \\ y_2 = r_0 \cdot \sin\left(\theta + \theta_p\right) \end{matrix}$$

From points P_1 and P_2, the angle and length of the line-of-sight was calculated as:

$$\theta_1 : \tan^{-1}\left(\frac{y_2 - y_1}{x_2 - x_1}\right)$$

$$\rho = \sqrt{(x_2 - x_1)^2 + (y_2 - y_1)^2}$$

The point of entry into the eyelid P_3 was calculated at the intersection of the line-of-sight and arc of the eyelid:

$$P_3: \begin{matrix} x_3 \\ y_3 \end{matrix} \text{ at intersection of } \begin{matrix} y = \frac{y_2 - y_1}{x_2 - x_1} \cdot x + h \\ (x - d_0 - t_0 - r_0)^2 + y^2 = (t_0 + r_0)^2 \end{matrix}$$

The distance of transmission through the eyelid was then calculated as the distance between P_2 and P_3:

$$t' = \sqrt{(x_2 - x_3)^2 + (y_2 - y_3)^2}$$

Since a 2D calculation was performed, the differential areas of the OLED and pupil were defined as:

$$dA_1 = w_0 \cdot dh$$

$$dA_2 = \frac{p_0}{4}\pi \cdot dp$$

The equation for radiative transfer was then integrated to provide the amount of light exiting the eyelid just above the pupil and is plotted in Figure 2.10:

$$\Phi(\theta) = \frac{L_0 w_0 p_0 \pi}{4} \int_{\frac{-h_0}{2}}^{\frac{h_0}{2}} \int_{\frac{-p_0}{2}}^{\frac{p_0}{2}} \frac{\cos(\theta_1) \cdot \cos(\theta + \theta_1 + \theta_p)}{\rho^2} \cdot T^{\frac{t'}{t_0}} \cdot dp \cdot dh$$

Weighting the transmissivity by the gaze angle during sleep, the average transmissivity can be estimated as:

$$T_{avg} = \frac{1}{4}T_{10^\circ} + \frac{1}{2} \cdot T_{30^\circ} + \frac{1}{4}T_{40^\circ} = \frac{1}{4}0.86 + \frac{1}{2} \cdot 0.23 + \frac{1}{4}0.05 = 0.34$$

Thus the intensity of light on the retina is likely 1/3 of what the designers intended due to this effect.

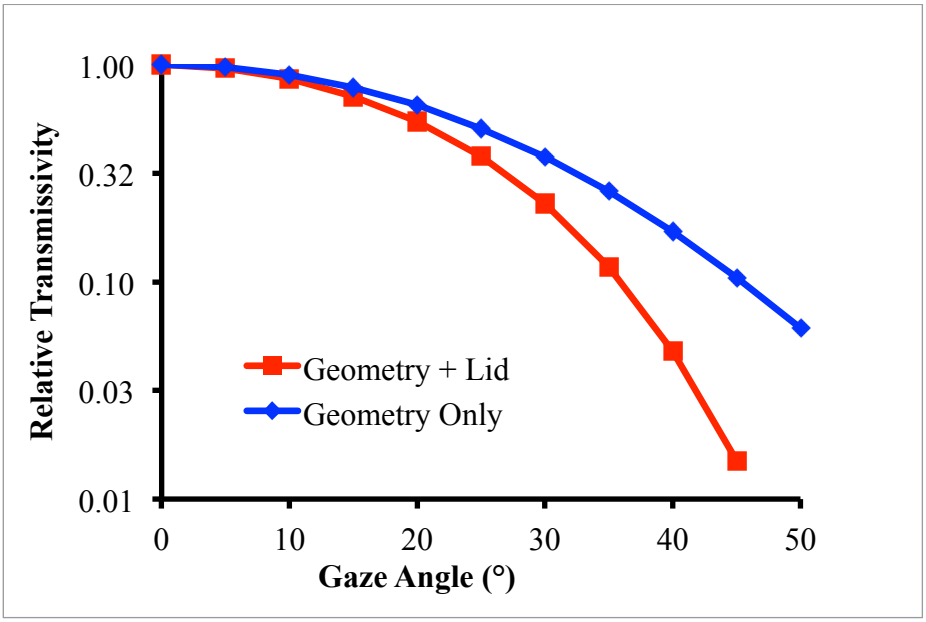

Figure 2.10: Relative amount of light transmitted to retina as a function of gaze angle while sleeping. Results of gaze angle only (blue) and combined gaze angle with eyelid absorbance (red) highlights the compounding of these loss mechanisms. Logarithmic y-axis.

Compliance Challenges for Sleep Masks

All phototherapy sleep mask trials to date report compliance as a major challenge. After an initial drop in compliance (defined as wearing the mask ≥6 hour/night) down to 30-45% following start of the trial, compliance continued to drop off exponentially with a time constant of 3 years [95] (paper appendix). Given that diabetic retinopathy is a slow progressing disease on the order of 10 years, it is unlikely that any meaningful number of patients would comply long enough to improve outcomes. Furthermore, the actual compliance in a real world setting compared to a clinical trial setting has historically been less than 50% [108], [109] (private correspondence with Tony Kuo, Director of Research

& Evaluation in the Division of Chronic Disease and Injury Prevention at the Los Angeles County Department of Public Health).

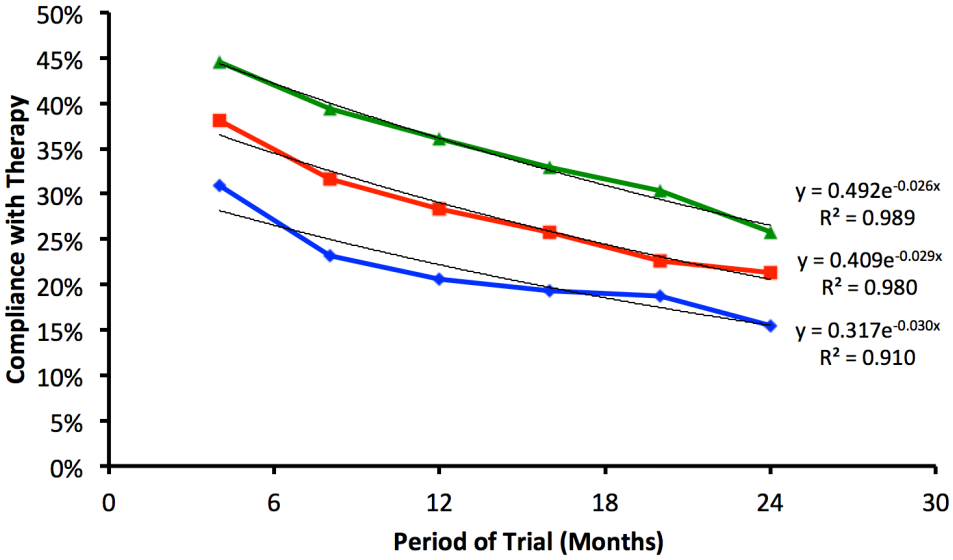

Figure 2.11: Compliance in CLEOPATRA phototherapeutic sleep mask trial over time. Level of compliance defined as wearing the mask for ≥6hours/night at least 70% (blue), 60% (red), or 50% (green) of the time. Adapted from supplementary data of [95].

The literature [109], [110] describes several factors that affect compliance to a therapy, including: cognitive (literacy, comprehension), interpersonal (physician-patient trust), cultural (socioeconomic), complexity of regimen, burden of regimen, immediacy of therapy results, among many others. In the case of preventative therapies like phototherapy, the two major challenges are the burden of the therapy and the lack of immediacy between therapy and results. What follows is an analysis of the impact these challenges have on sleep mask phototherapy and a proposed solution to overcome them.

Analysis of Troxler Neural Adaptation in Phototherapy

The idea of shining light onto the retina to suppress retinal metabolism and prevent tissue hypoxia makes good physiological sense but faces the immediate objection that it will negatively impact the ability of the patient to sleep. However, the visual system like many sensory systems responds to changes in stimuli rather than absolute stimuli magnitude. This gives rise to the well known phenomenon whereby a stabilized image on the retina quickly disappears from conscious vision, known eponymously as Troxler fading [26], [111]–[114]. Studies with contact lenses and suction cups have demonstrated that when illumination is stabilized on the retina, complete perceptual loss occurs within a few minutes [115].

Using data on time to fading versus luminance difference [111], the time constant of Troxler fading was estimated. The data was plotted as time to fading versus the ratio of maximum to minimum/background scene luminance. A logarithmic fit was used due the logarithmic nature of vision and need for only a single parameter *k*; it also returns a time to fading of 0 for a ratio of 1, as expected:

$$\text{Time to Fading} \;=\; \mathrm{k} \cdot \ln\left(\frac{\mathrm{B_{max}}}{\mathrm{B_{min}}}\right)$$

A further assumption was made that the fading is exponential in nature. Humans are able to perceive contrast differences $\frac{\mathrm{B_{max}}-\mathrm{B_{min}}}{\mathrm{B_{max}}+\mathrm{B_{min}}}$ on the order of 8% [116][117]. Given that an exponential will decay within 2.5 time constants τ to 8%, the time to fading was approximated as 2.5τ. The resulting fit had a constant of k = 12:

$$2.5 \cdot \tau \;=\; 12 \cdot \ln\left(\frac{\mathrm{B_{max}}}{\mathrm{B_{min}}}\right) \text{[s] with an } \mathrm{R^2} = 0.88$$

$$\tau = 4.8 \cdot \ln\left(\frac{B_{max}}{B_{min}}\right) [s]$$

Then, a retinal image of initial brightness B will fade as follows:

$$B_{perceived} = B_0 \cdot e^{-\frac{t}{\tau}}$$

Consider that changes in perceived brightness can occur as a combination of temporal changes (*e.g.* neural adaptation) and changes due to eye motion across a scene of varying brightness. The material derivative can be used to combine these contributions:

$$\frac{DB}{Dt} = \frac{\partial B}{\partial t} + \boldsymbol{u} \cdot \nabla B$$

Where B is the brightness and **u** is the velocity of gaze parameters (*e.g.* angle, pupil area), ∇ is the gradient. Consider a simplified case where only gaze angle varies at a rate $\frac{d\theta}{dt}$ (*i.e.* assume pupil area is constant). Then the perceived brightness is governed by:

$$\frac{DB}{Dt} = -\frac{B}{\tau} + \frac{d\theta}{dt}\frac{dB}{d\theta}$$

To solve the differential equation, consider a specific example where the eye is oscillating between two gaze angles within a period of time T.

$$\theta(t) = \frac{\theta_{max}+\theta_{min}}{2} + \frac{\theta_{max}-\theta_{min}}{2}\left(\sin\left(2\pi\frac{t}{T}\right)\right)$$

From the previous analysis of retinal irradiance from Noctura 400 versus gaze angle, the orientation of the eye can be mapped to an actual brightness. For simplicity of analysis, assume a linear mapping $\theta_{max} \rightarrow B_{max}$ and $\theta_{min} \rightarrow B_{min}$, then:

$$B_{scene}(t) = \frac{B_{max}+B_{min}}{2} + \frac{B_{max}-B_{min}}{2}\left(\sin\left(2\pi\frac{t}{T}\right)\right)$$

$$\frac{dB}{dt} = \frac{B_{max} - B_{min}}{2}\frac{2\pi}{T}\cos(2\pi\frac{t}{T})$$

Solving the differential equation:

$$B_{perc}(t) = \frac{\left(2\pi\frac{\tau}{T}\right)^2 \frac{B_{max} - B_{min}}{2} \sin\left(2\pi\frac{t}{T}\right)}{\left(2\pi\frac{\tau}{T}\right)^2 + 1} + \frac{2\pi\frac{\tau}{T}\frac{B_{max} - B_{min}}{2} \cos\left(2\pi\frac{t}{T}\right)}{\left(2\pi\frac{\tau}{T}\right)^2 + 1} + k_1 e^{-\frac{t}{\tau}}$$

The term $k_1 e^{-\frac{t}{\tau}}$ in the solution of the equation is ignored because it quickly decays away.

For $\frac{\tau}{T} \gg \frac{1}{2\pi} \cong 0.16$ (*i.e.* changes in brightness are fast with respect to neural adaptation):

$$B_{perc}(t) = \frac{B_{max} - B_{min}}{2} \sin\left(2\pi\frac{t}{T}\right) + \frac{\frac{B_{max} - B_{min}}{2} \cos\left(2\pi\frac{t}{T}\right)}{2\pi\frac{\tau}{T}}$$

$$B_{perc}(t) \cong \frac{B_{max} - B_{min}}{2} \sin\left(2\pi\frac{t}{T}\right)$$

For $\frac{\tau}{T} \ll \frac{1}{2\pi} \cong 0.16$ (*i.e.* changes in brightness are slow with respect to neural adaptation):

$$B_{perc}(t) = 2\pi\frac{\tau}{T}\frac{B_{max} - B_{min}}{2}\left(2\pi\frac{\tau}{T}\sin\left(2\pi\frac{t}{T}\right) + \cos\left(2\pi\frac{t}{T}\right)\right)$$

$$B_{perc}(t) \cong 2\pi\frac{\tau}{T}\frac{B_{max} - B_{min}}{2}\cos\left(2\pi\frac{t}{T}\right)$$

In general, the range (max-min) of perceived brightness is:

$$B_{perc,range} = 2\pi\frac{\tau}{T}\frac{B_{max} - B_{min}}{\sqrt{\left(2\pi\frac{\tau}{T}\right)^2 + 1}}$$

From studies on human sleep, room light levels of 5-10 lux (lm/m^2) have been shown to cause sleep disturbance and depression [118]. This amounts to approximately 0.5-1 photons/μm^2/s on the retina. As an example, consider the eye deviating from 35° to 40°, which will cause a change in brightness of $\frac{B_{35°}}{B_{40°}} = 2.5$ and an expected Troxler fading

time constant of 4.4 s. Assuming 100 photons/μm^2/s is provided by the Noctura 400, then the perceived brightness is:

$$B_{perc,range} = 2\pi\frac{11}{T}\frac{100-\frac{100}{2.5}}{\sqrt{\left(2\pi\frac{11}{T}\right)^2+1}}$$

Figure 2.12 plots the perceived brightness of light on the retina as a function of the period of eye oscillation between 35° to 40°. It can be observed that even relatively small and slow eye movements are expected to produce a flicker in light intensity above levels (1 photon/μm^2/s) known to cause sleep disturbance.

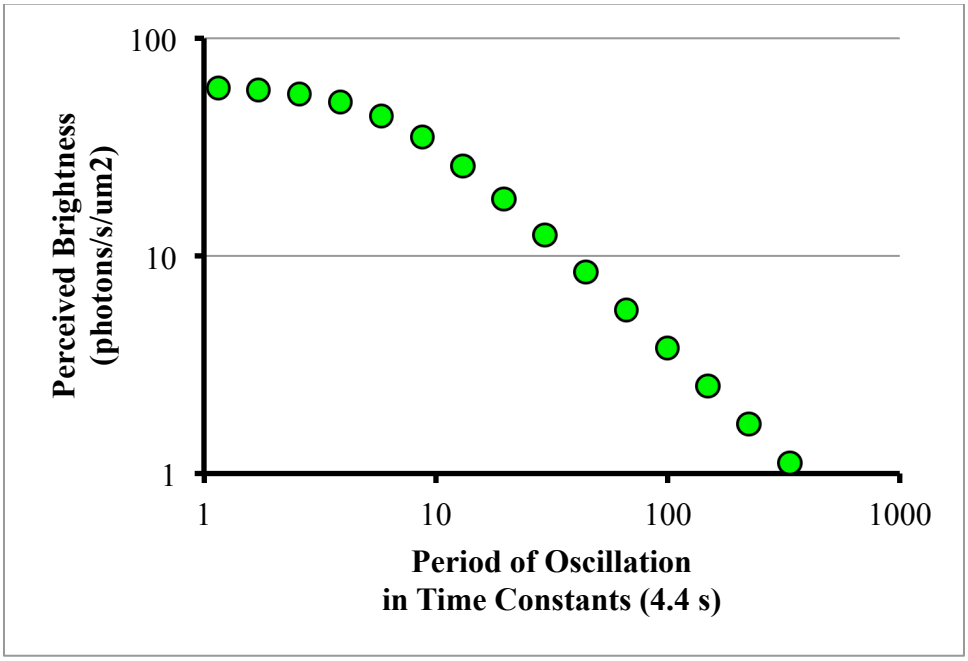

Figure 2.12: Perceived brightness of light from a sleep on retina versus the period of eye oscillation between 35 to 40°.

This analysis shows that Troxler neural adaptation is generally too slow to eliminate perception of light from a sleep mask. Even addition of a feedback control system is unlikely to provide much improvement given that different regions of the retina

experience different levels of light attenuation as a function of gaze angle. Compensation of total retinal light dose not overcome this problem. One viable solution is to affix the light source to the eye such that it maintains a constant path despite eye movement. This can be accomplished through an implant or a contact lens. Psychophysical studies using light sources suction cupped onto the cornea to stabilize retinal illumination have shown elimination of perceived light (to levels comparable with Eigengrau) well into the photopic range, highlighting the viability of such an approach [115].

Pros and Cons of Phototherapy Light Mask Approach

The concept of phototherapy is promising for the treatment of diabetic retinopathy; however, a sleep mask is likely not the best means of delivering the therapy. The following chapters explore the development of new phototherapy devices that overcome the limitations of sleep masks.

Table 2.8: Pros and cons of sleep mask phototherapy.

Pros	Cons
• No irreversible eye damage or side-effects due to treatment (compared to traditional therapies like laser and repeated anti-VEGF injections • A preventive therapy • Agnostic of phenotype (*e.g.* genetic factors) • Validated clinical safety [95], [119]	• Illumination occurs through the eyelid and is not uniform across patients • Eye rolls back towards the skull during sleep (Bell's phenomena), leading to variation of light dosage on the retina and affecting sleep quality • Requires regular nightly use for therapeutic efficacy • Bulky device on face while sleeping, thus leading to compliance issues • Phototherapy is yet to obtain regulatory approval • Phase III trials [95] refuted efficacy claims of previous trials [119] • Troxler neural adaptation is incomplete

CHAPTER 3 – Chandelier Style Phototherapy Device

Key Take-Aways
• Radioluminescence provides long-term retinal illumination and a small size. • Skirt-style anchoring system allows for rapid and leak-free implantation of a chandelier device through the pars plana. • 4-week animal tests demonstrate safety of implantation and phototherapy

The delivery mode of phototherapy is critical to the success of the therapy for anatomical/physiological reasons (*e.g.* external light is attenuated by the eyelid and pupil; varying eye gaze during sleep causes light intensity variation) as well as human factors (*e.g.* low long-term patient compliance in preventative therapies). One strategy for delivering light to the retina at a constant, predictable, and therapeutic dose is to implant the light source within the eye. Clinical success in glaucoma drainage devices and retinal prostheses has demonstrated that long-term implantation is feasible. The additional benefit of implantation is that patient compliance can be greatly improved so long as the device does not require patient input (*e.g.* recharging device). This chapter develops and describes an implantable phototherapy device powered via radioluminescence.

Choosing Radioluminescence

There are numerous means of producing light such as electrical discharge, incandescence, and luminescence. Each method has distinct benefits, limitation, and

constraints that restrict suitability for a given application. For the purposes of an ocular implant, it is desirable that the method:

- require minimal power
- occupy minimal volume
- have maximal lifetime
- generate minimal byproducts (*e.g.* heat, waste, sound, radiation)
- is safe (product of probability of failure and severity of failure)
- maintain performance in the body (*i.e.* does not degrade)
- be controllable
- provide sufficient light output

After analyzing the available means of light generation, radioluminescence stood out as a viable candidate. Radioluminescence is the production of light through the interaction of ionizing radiation (*e.g.* alpha particle, beta particle, gamma ray) with a phosphor material. Several radioluminescent systems have been developed:

- Radium-based: Radium-226 emits alpha particles with an average energy of 4.6 MeV to excite a combined phosphor. The high-energy alpha particles can damage the phosphor leading to degradation of luminosity over several years, significantly faster than the half-life of 1600 years. Furthermore, gamma rays of 0.7 MeV are also produced and can escape encapsulating layers, thus posing a safety risk.
- Promethium-based: Promethium-147 emits beta particles with a maximum energy of 0.23 MeV to excite a combined phosphor. However, the half-life is only 2.62 years and the high energy beta particles can penetrate up to 5mm of tissue, water, or plastic thus posing a safety risk.

- Strontium-based: Strontium-90 emits beta particles with a maximum energy of 0.546 MeV to excite a combined phosphor. It has a half-life of 28.8 years but the penetration depth of its beta particle and its long biological half-life of 18 years make it a safety risk.
- Tritium-based: Hydrogen-3 is a gas that emits beta particles with an energy of around 5keV (maximum 18.6 keV) to excite a phosphor within a hermetically sealed compartment. It has a half-life of 12.3 years. The low energy beta particle and short biological half-life of 8.2 days make it relatively safe.

Gaseous tritium light source (GTLS) provided the best combination of luminous lifetime and safety profile and were selected to move forward with. Extensive safety and testing data on tritium light sources is compiled in [120].

The activity of tritium commonly appears in units of Bequeral (Bq = [decays / s]). The molar content of tritium can be calculated, knowing the half-life of tritium as:

$$N_0 = \frac{Bq}{N_A\left(\frac{\ln 2}{\tau_{1/2}}\right)}$$

The parameters for the utilized GTLS (mb-microtec, CH) are summarized in Table 3.1.

Table 3.1: Measured and reported parameters of GTLS [121].

Model	T-6915	T-5666
Outer Diameter	300 µm	1.5 mm
Inner Diameter	250 µm	1 mm
Length	2 mm	6 mm
Wall Thickness	25 µm	250 µm
Tritium Activity	0.016 GBq	0.91 GBq
Tritium Content	15 nmol	850 nmol

Mechanism of Action

A gaseous tritium light source is constructed by filling a phosphor-lined glass capillary with tritium and then hermetically sealing it, often by use of a carbon diode laser. The tritium undergoes beta decay with a half-life of 12.3 years emitting high-energy electrons with an average energy of 5.7 keV that strike the phosphor. As the electron penetrates the phosphor, its kinetic energy converts to electrical energy through ionization of the phosphor atoms. The excited electrons diffuse within the phosphor until they are captured by luminescent/impurity centers where they de-excite, emitting a photon in the process. The phosphor and dopant are chosen to produce emission centered at particular wavelength, usually in the visible spectrum.

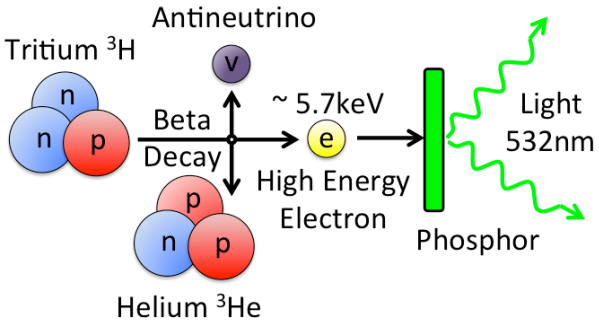

Figure 3.1: Principle of radioluminescence in a gaseous tritium light source. Tritium undergoes beta decay, emitting a high-energy electron, which strikes and ionizes phosphor, leading to light emission.

Source Lifetime

The brightness of GTLS decreases over time due primarily to an exponential decay in the tritium content, the degradation of the phosphor, and pressure buildup ($T_2 \rightarrow 2$ He) [121]. Reports from the manufacturer indicate that brightness will decrease to about 60-80% over 2 years and 10-50% over 10 years.

Safety Considerations

There are 3 major safety considerations in utilizing gaseous tritium light sources: the uptake of tritium from a fractured capillary, the escape of beta particles, and bremsstrahlung radiation. For implanted devices, the risk of fracture is minimal; however, the risk must be managed in the case of worn devices like contact lenses or sleep masks. Each of these aspects is covered in detail below.

Risk of Tritium Uptake from Broken Device

The radioluminescent light sources are themselves composed of a green emitting phosphor encapsulated in a glass capillary, which is filled with pure tritium gas. Tritium is considered one of the safest radioisotopes, having a half-life of 12.3 years and emitting a very low energy beta particle (<18.6 keV, average of 5.7 keV), unable to penetrate through the glass capillary.

From a radiation safety perspective, the worst hypothetical scenario would involve the breakage of the tritium capillary, oxidation of all the tritium to form tritiated water, followed by retention of the tritiated water within the body with a biological half-life of 10 days. The effective dose that would result is 20 mSievert per μmol tritium. For reference, a full body CT-scan is around 20 mSv. The calculation of dose is as follows. Tritium has a radioactive half-life, τ_R, of 12.3yrs and therefore beginning with an initial amount of tritium N_0, the remaining tritium if lost purely by radioactive decay is:

$$N_R(t) = N_0 \cdot 2^{\frac{-t}{\tau_R}} = N_0 \cdot e^{-t \cdot \frac{\ln(2)}{\tau_R}}$$

The rate constant for decay is then:

$$k_R = \frac{\ln(2)}{\tau_R}$$

In the body, tritium can oxidize to form tritiated water. Water has a biological half-life τ_B of less than 10 days or a rate constant of elimination of:

$$k_B = \frac{\ln(2)}{\tau_B}$$

Tritium within the body can therefore be eliminated by one of two mechanisms: radioactive decay or biological elimination. The rate of tritium loss is the sum of the two:

$$\frac{dN}{dt} = -k_R \cdot N - k_B \cdot N = -N \cdot (k_R + k_B)$$

So starting from an initial dose of tritium N_0 the amount left in the body is:

$$N(t) = N_0 e^{-(k_R + k_B) \cdot t}$$

The instantaneous dose D of radiation the body absorbs is:

$$D = k_R \cdot N(t)$$

The total dose T of radiation is the integration of the instantaneous dose over time:

$$T = \int_0^\infty D\, dt = \int_0^\infty k_R \cdot N_0 \cdot e^{-(k_R + k_B) \cdot t} = N_0 \cdot \frac{k_R}{k_R + k_B} = N_0 \cdot \frac{\tau_R}{\tau_R + \tau_B}$$

$$\frac{T}{N_0} = \frac{10 \text{ days}}{12.3 \text{ yrs} \cdot 365 \frac{\text{days}}{\text{yr}} + 10 \text{ days}} = 0.22\% \text{ decay in body}$$

The dosage can be then converted to standard units by assuming the beta particles (average energy of 5.7 keV/decay = 9.13×10^{-16} J/decay) are emitted uniformly over the entire body of a 60kg individual:

$$\frac{\text{Dosage}}{N_0} = \frac{(0.0022)\left(9.13 \times 10^{-16} \frac{\text{J}}{\text{decay}}\right)\left(6.022 \times 10^{23} \frac{\text{decay}}{\text{mol}}\right)}{60 \text{ kg}} = 20 \frac{\text{mGray}}{\mu\text{mol}}$$

When converting from dose (Gray) to effective dose (Sieverts), both the weighting factors for particle type and anatomical distribution are 1, so there is no weighting.

Risk of Beta Particle Escape and Considerations of Penetration Depth

The high-energy beta particle emitted during the radioactive decay of tritium is supposed to deposit its energy in the phosphor coating through ionization ultimately produce light. However, suppose the electron passes through a crack in the phosphor and strikes the glass capillary instead. It is worthwhile to consider the maximal penetration depth that would be expected to ensure the construction of the capillary is suitable to avoid radiation escaping the device.

The continuous slowing down approximation range Δx is found by integrating the reciprocal of the stopping power of the substrate, $S(E) = -\frac{dE}{dx}$, from the initial/maximal energy of the particle to rest [122]. Stopping power is often reported as mass stopping power S_m by dividing the stopping power by density. Using data for Pyrex glass [123] and a maximal beta electron energy of 18.6 keV, the continuous slowing down approximation range is then:

$$\Delta x = \int_0^{E_0} \frac{1}{S_m(E) \cdot \rho_{pyrex}} dE = \int_0^{18.6\ keV} \frac{1}{S_m(E) \cdot 2.32\ g/cm^3} dE = 4.5\ \mu m$$

Thus as long as the capillary is greater than 5 μm thick, negligible beta particles will escape the device. For a phosphor like zinc sulfide, $CSDA_{ZnS}$(20 keV) = 2.8 μm, which gives a ballpark estimate for the maximal thickness of this layer.

Risk of Bremsstrahlung Radiation

Electron energy loss by ionization increases approximately logarithmically with energy where as bremsstrahlung losses increase approximately linearly with energy. The critical energy E_c is defined as the energy at which both loss rates are equal. For

borosilicate glass the critical energy is around 50 MeV [124], so the fraction of energy lost to bremsstrahlung for an the relatively low energy, 18.2 keV tritium beta electron is negligible. The same is true for the low atomic weight phosphor [125]. Figure 3.2 plots the relative contributions of ionization and bremsstrahlung radiation loss mechanisms for copper, which has an E_c of around 20 MeV and Z=29, so it provides an upper bound on expected bremsstrahlung from lower atomic weight materials like glass and phosphor.

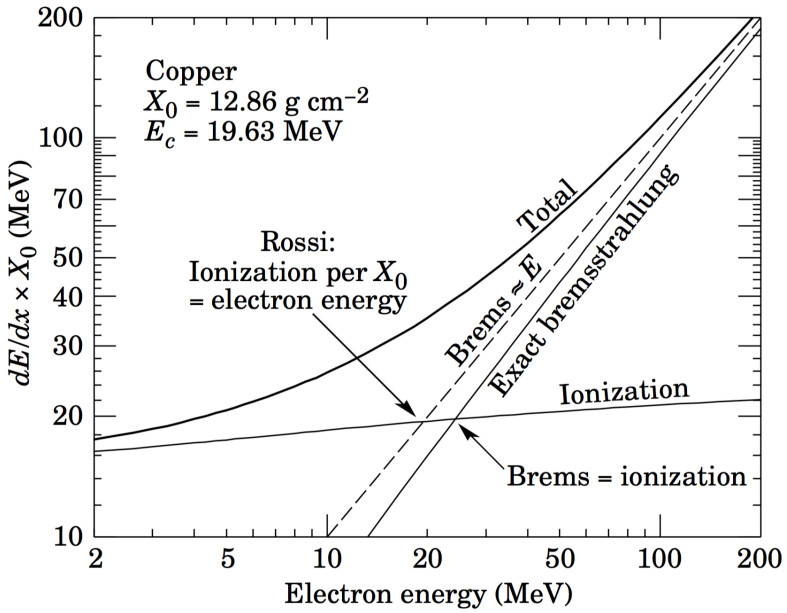

Figure 3.2: Relative contributions of ionization versus Bremsstrahlung losses in Copper (Z=29). Reprinted from [125] .

Irradiance vs. Distance from GTLS

According to the geometry in Figure 3.3, the radiant flux expected from a vertical cylindrical source on a surface below was calculated as a function of perpendicular distance away from the source axis, r. This calculation allows for the determination of source radiance.

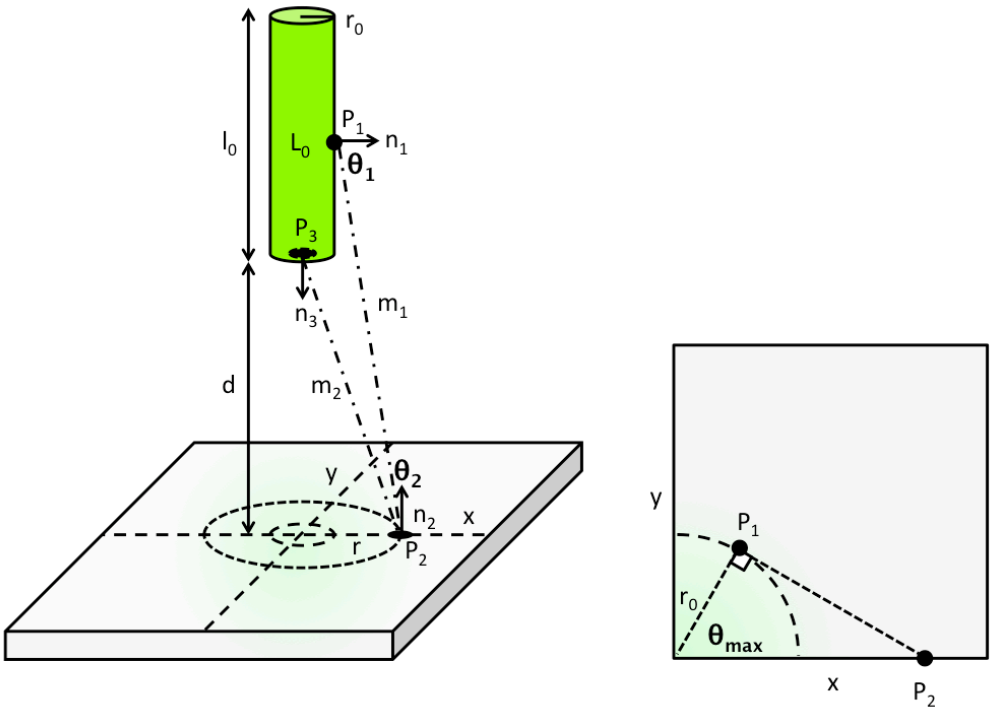

Figure 3.3: Geometry of GTLS with respect to photodetector in setup.

The calculation is as follows:

$$P_1 = (r_0 \cdot \cos(\theta), r_0 \cdot \sin(\theta), z)$$

$$P_2 = (r, 0, 0)$$

$$P_3 = (0, 0, d)$$

$$\vec{n}_1 = (\cos(\theta), \sin(\theta), 0)$$

$$\vec{n}_2 = (0, 0, 1)$$

$$\vec{n}_3 = (0, 0, -1)$$

$$\rho_{1,2} = \|P_2 - P_1\|$$

$$\rho_{2,3} = \|P_3 - P_2\|$$

$$\vec{m}_{1,2} = \frac{P_2 - P_1}{\rho_{1,2}} = -\vec{m}_{2,1}$$

$$\vec{m}_{3,2} = \frac{P_2 - P_3}{\rho_{3,2}} = -\vec{m}_{2,3}$$

$$\cos(\theta_1) = \vec{n}_1 \cdot \vec{m}_{1,2}$$

$$\cos(\theta_2) = \vec{n}_2 \cdot \vec{m}_{2,1}$$

$$\cos(\theta_3) = \vec{n}_3 \cdot \vec{m}_{3,2}$$

$$\cos(\theta_4) = \vec{n}_2 \cdot \vec{m}_{2,3}$$

$$\theta_{max} = \cos^{-1}\left(\frac{r_0}{r}\right)$$

$$dA_1 = r_0 \cdot d\theta \cdot dz$$

$$A_3 = \pi \cdot {r_0}^2$$

Then the radiant flux due to the sidewall of the cylinder is:

$$\frac{d\Phi_{side}}{dA_2} = \int_{A_1} L \cdot \cos(\theta_1) \cdot \frac{\cos(\theta_2)}{{\rho_{1,2}}^2} \cdot dA_1$$

$$\frac{d\Phi_{side}}{dA_2} = \int_{d}^{d+l_0} \int_{-\theta_{max}}^{\theta_{max}} L \cdot \frac{r0 \cdot (-r0 + r \cdot \cos(\theta)) \cdot z}{(r^2 - 2 \cdot \cos(\theta) \cdot r \cdot r0 + r0^2 + z^2)^2} d\theta dz$$

The radiant flux due to the bottom of the cylinder is:

$$\frac{d\Phi_{bottom}}{dA_2} = L \cdot \cos(\theta_3) \cdot \frac{\cos(\theta_4)}{{\rho_{3,2}}^2} \cdot A_3$$

$$\frac{d\Phi_{bottom}}{dA_2} = L \cdot \frac{\pi \cdot d^2 \cdot r0^2}{(d^2 + r^2)^2}$$

The total radiant flux on the sensor A_2 is then found by integrating total radiant flux over surface, noting that:

$$r = \sqrt{x^2 + y^2}$$

$$\Phi_{sensor} = \int_{A_2} d\Phi_{bottom} + d\Phi_{side}$$

In order to extract the radiance of the GTLS, the theoretical radiant power incident on the sensor was plotted as a function of distance and compared to the experimentally collected measurements. The best fit of the model occurred for a radiance of L = 2.56 mW/sr/m^2. This value is within the range the manufacturer reported [121]. The experimental details follow.

The photon irradiance as a function of distance from several GTLSs was measured using a Newport Power Meter (Model 1936-R) with photosensor wand (918D-ST-UV). Characterization enabled the selection of the smallest source capable of providing sufficient dosage for phototherapy. The photosensor was placed directly underneath the GTLS, which was affixed to a linear micrometer stage, allowing for precise control of the distance (Figure 3.6). The work was carried out in a dark room and the setup was further covered with a dark box between measurements. Using this setup, ambient light levels were below 1 pW/cm^2 (0.027 photons/s/μm^2) over the experiment. The GTLSs were measured in both a vertical (perpendicular) and horizontal (parallel) orientation with respect to the photosensor. Results for 1.5 mm D × 6 mm L and 300 μm D × 2 mm L GTLS with green phosphor (532 nm peak emission, 74 nm FWHM) are displayed in Figure 3.4 and Figure 3.5, respectively.

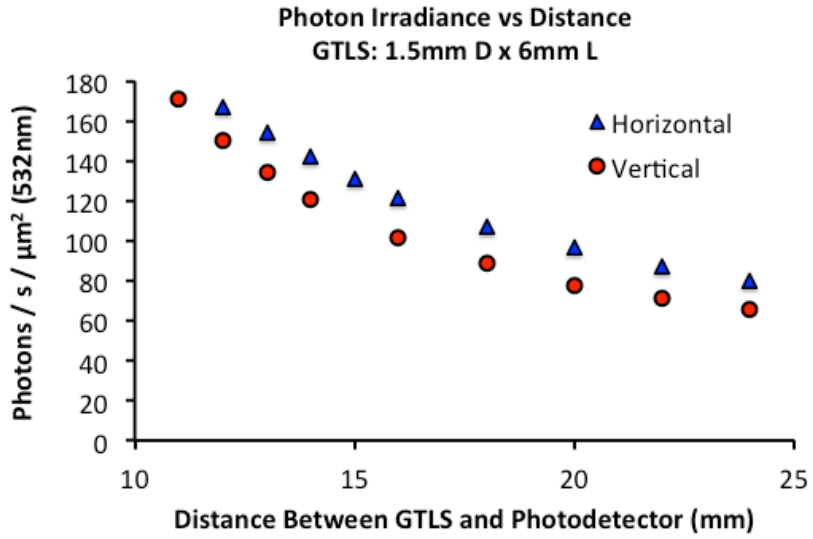

Figure 3.4: Photon irradiance as a function of distance from a GTLS source of 1.5 mm diameter, 6 mm length. Orientation of the source was either horizontal (parallel) or vertical (perpendicular) with respect to the photodetector. Shortest distances between GTLS and photodetector reported.

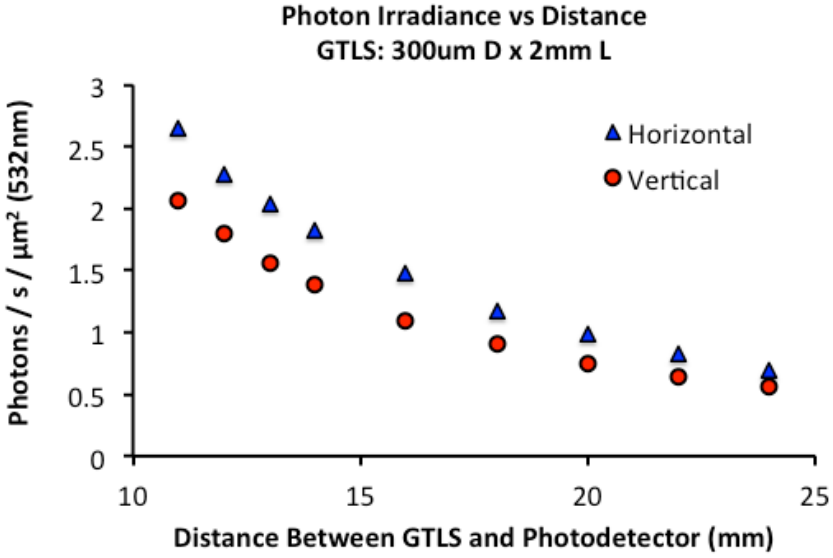

Figure 3.5: Photon irradiance as a function of distance from a GTLS source of 300 µm diameter, 2 mm length.

The 1.5 mm D×6 mm L GTLS provides a light output of:

$$P = 2\pi \cdot L_{h\nu} \cdot A_{GTLS} = 2\pi \cdot L_{h\nu} \cdot (2 \cdot \pi r^2 + 2\pi rl) = 4\pi^2 \cdot L_{h\nu} \cdot (r^2 + rl)$$

$$P = 4\pi^2 \cdot \left(2.56 \frac{mW}{sr \cdot m^2}\right) \cdot \left((7.5{\times}10^{-4} m)^2 + (7.5{\times}10^{-4} m)(6{\times}10^{-3} m)\right)$$

$$P = 510\ nW = 1.37{\times}10^{12} \frac{photons}{s} (532\ nm)$$

This light output is suitable for suppression of rod cell metabolism based on the range of irradiances explored in Chapter 2, which estimated $7{\times}10^{11}\ \frac{photons}{s \cdot retina}$.

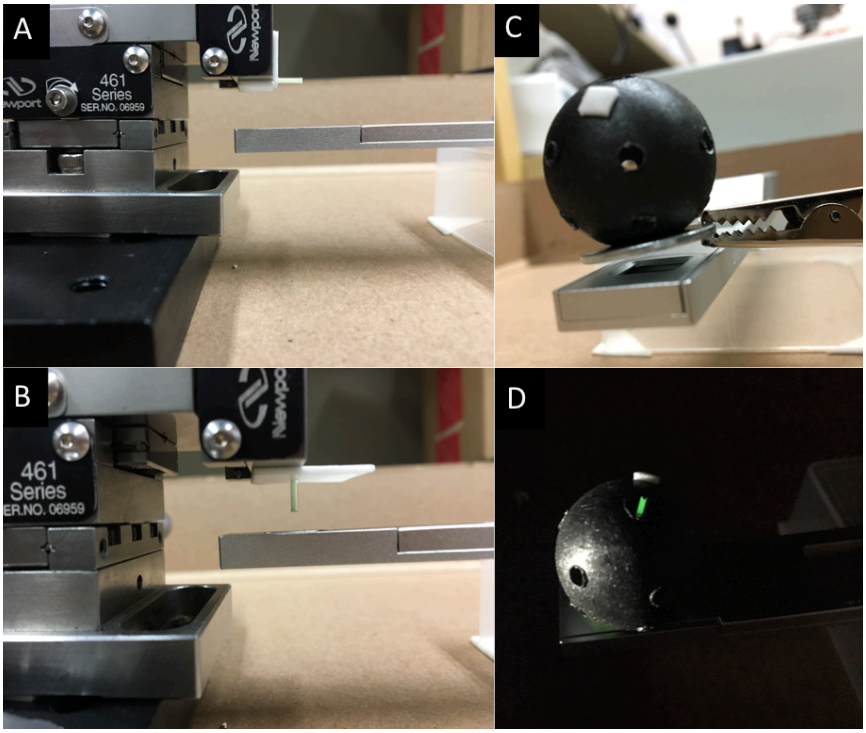

Figure 3.6: Setup for characterizing light output from GTLS. (A, B) Irradiance versus distance was measured by moving the GTLS known distances away from the photodetector in horizontal and vertical orientations, respectively. (C, D) Ocular model setup used measure the expected irradiance at various locations on retina. Isolated through-ports are sequentially positioned over the photodetector and measured.

Characterization of Irradiance from GTLS in an Eye Model

The candidate light source (1.5 mm D × 6 mm L) was then tested in an ocular model to map photon irradiance uniformity on the retina. The setup consisted of a hollow blackened polypropylene 25 mm diameter sphere with sampling ports drilled in three circumferential bands for taking irradiance measurements. The GTLS was inserted through a closely sized hole and secured (Figure 3.6).

Retinal photon irradiance was observed to be within the range of predicted therapeutic value over the eye, varying by a factor of 3× over the entire retina but by only a factor of 1.6× over the mid-periphery. Given that vision is logarithmic in nature, the variation in photon irradiance is acceptable.

Position	Irradiance (532nm) (photons/s/cm²)	Relative %
A1	9.96E+09	100%
A2	4.38E+09	44%
A3	4.38E+09	44%
A4	4.32E+09	43%
A5	6.57E+09	66%
A6	8.45E+09	85%
B1	4.48E+09	45%
B2	4.20E+09	42%
B3	3.41E+09	34%
B4	3.60E+09	36%
B5	3.82E+09	38%
B6	3.88E+09	39%
C1	3.16E+09	32%
C2	2.82E+09	28%
C3	3.19E+09	32%

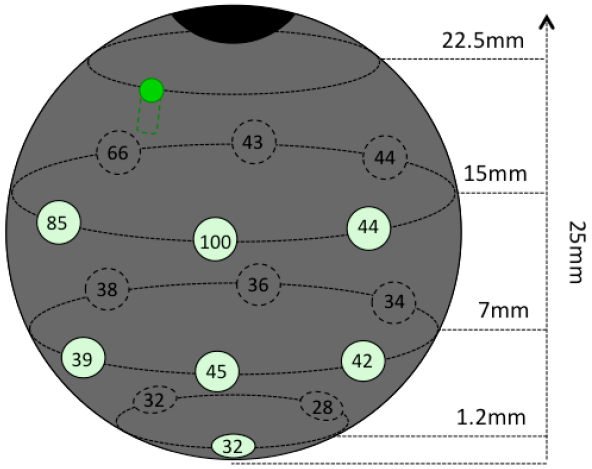

Figure 3.7: Retinal photon irradiance measured within an in vitro eye model from a GTLS (1.5 mm D × 6 mm L). Sampling ports are spaced evenly in circumferential bands as indicated. The absolute photon irradiance measured at each port is indicated (left), while the % of maximum is overlaid on the schematic (right). Position of the GTLS was at the pars plana and the device was affixed in a radial alignment.

Implant Site and Surgical Considerations

The pars plana was selected as a site for implantation given that it serves no major function in adult eyes and provides access into the posterior chamber of the eye with direct line-of-sight to the retina. Ophthalmological procedures commonly use the pars plana as an entry site for glaucoma drainage devices [126], [127]. The pars plana is approximately 4 mm wide and located around 3 mm from the corneal limbus, between the pars plicata and ora serrata.

Biocompatibility and Stability Considerations

There are major challenges in designing long term implants, especially with respect to: 1) biocompatibility, 2) degradation of active components, and 3) interfacial bond failure. The proposed design overcomes these challenges by utilizing borosilicate glass encapsulation of the active lighting system and a medical grade silicone anchoring system. Borosilicate glass encapsulation provides the highest level of protection to the internal components, as it is impermeable to all chemicals found in a biological system. Furthermore, it provides a hermetic package to maintain the tritium gas and phosphor inside the implant. Borosilicate glass also has the highest level of bioinertness [128], [129] and is frequently used as the negative control in biocompatibility testing. It provokes minimal if any host response. The medical grade silicone used was MED4-4210 (NuSil, CA), which is designed for long-term implantation in humans and already is in use in ocular implants [130]. Silicones can form irreversible bonds with glass, providing durable interfaces.

Scleral Anchoring System

Implantable devices were fabricated by securing a GTLS (mb-microtec ag, Switzerland) to a medical grade silicone anchoring system (MED4-4210 PDMS), Figure 3.8. The purpose of the anchoring system is to easily and reliably secure the device in the sclera while preventing leakage of vitreous humor transclerally around the implant.

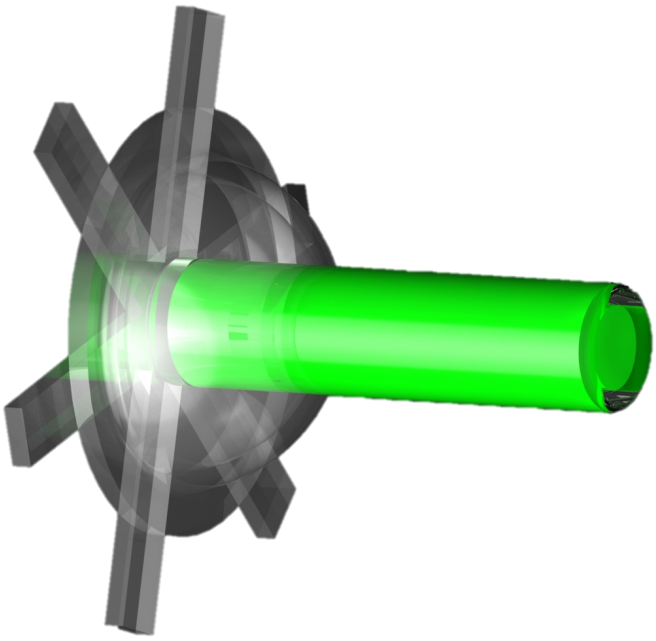

Figure 3.8: Rendering of transcleral phototherapy implant with PDMS acnhoring system and GTLS light source.

The anchoring system has a back-plate that sits on the surface of the sclera, preventing the device from falling into the eye, and a hemispherical skirt structure that creates a seal against the inside of the eye (ciliary body) to prevent the device from being pushed out of the eye and to block fluid leakage. The back-plate of the anchoring system was formed by casting PDMS in a 240 μm deep dry-film photoresist mold. It consists of 6 arms that provide a place for the surgeon to grip the device, which can be trimmed

following implantation. It is bonded to the bottom of the GTLS cylinder via PDMS gluing. The hemispherical skirt has a 2 mm radius to fit the pars plana and was created by spin coating PDMS (2.5 krpm, 1 min results in approximately 240 μm thickness) onto a hemispherical mold and trimming with a 5 mm diameter biopsy punch. A central 1.5 mm hole punched into the center of the skirt allows it to encircle the GTLS and a small bead of PDMS glues it securely. Upon implantation of the device, the hemispherical skirt compresses to accommodate the thickness of the sclera (approximately 0.5 mm at the pars plana [131]), ensuring a tight seal. Figure 3.9 summarizes the dimensions of the device components.

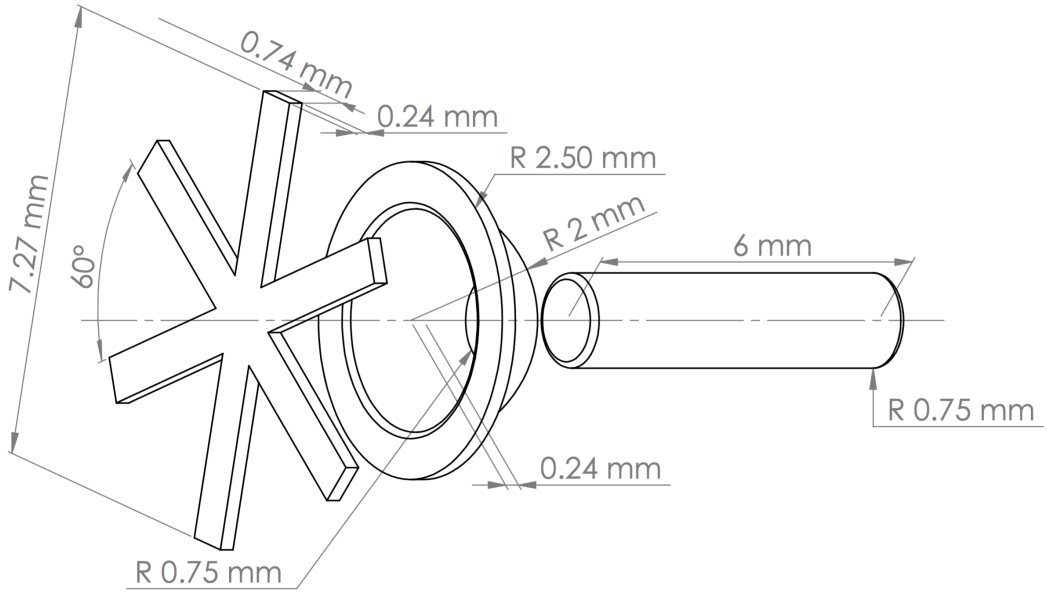

Figure 3.9: Component dimensions for the transcleral phototherapy implant: (left) Back-plate, (middle) hemispherical skirt, (right) GTLS. The back-plate is glued to the bottom of the GTLS with PDMS while the skirt encircles the GTLS and is bonded with a bead of PDMS around the interface.

Implantation Procedure

Development of the implantation procedure used an excised porcine eye model. Sierra Medical, Whittier, CA supplied fresh unscalded eyes, which were used immediately. Figure 3.10 summarizes this process.

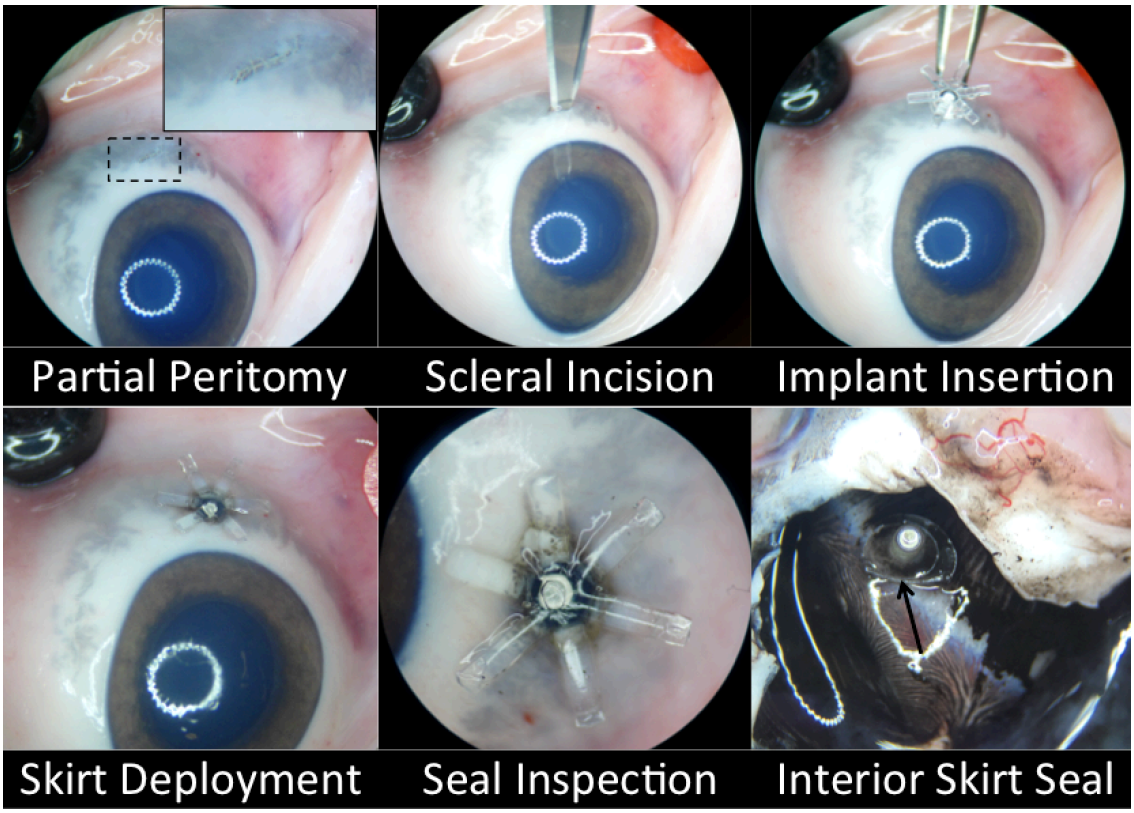

Figure 3.10: Implantation of device into porcine eye. A partial peritomy provides access through the conjunctiva to the sclera. A scleral incision of 2.5mm is made at the pars plana. The implant is inserted through the incision. The deployment of the skirt locks the device in place. The seal of the skirt prevents leakage of fluid from the eye. The tight seal of skirt against the inside of the eye can be visualized in a cut away of the eye.

The developed procedure involves an incision in the conjunctiva at the pars plana to provide access to the underlying sclera (*i.e.* partial peritomy). A 2.5mm linear incision

in the sclera made with a scalpel provides an entry that can expand to a diameter of 1.6mm – sufficient to accommodate the outer diameter of the GTLS (1.5mm) and skirt. The implant is then gripped firmly with forceps and inserted through the incision. To ensure the deployment of the skirt against the ciliary body, the arms of the device can be grasped with forceps and the device can be pushed further in. The successful deployment of the skirt is quite apparent with a tactile clicking sensation and robust anchoring of the device in place. The arms of the device can be trimmed down using surgical scissors if desired and covered with the conjunctiva to prevent infection of the implant site.

Leak Testing of the Anchoring Mechanism

The quality of the seal of the implant against the ciliary body is important since excessive transcleral leakage of fluid from the vitreous can cause conjunctival blebbing and hypotony. Leakage was evaluated by measuring the permeation rate of fluid from freshly enucleated porcine eyes (Sierra Medical, USA; used within 12 hrs of receipt) when subject to physiologic pressure (10-21 mmHg) with (n=3) and without an implant (n=3).

A syringe was inserted into each eyeball and connected to an elevated column of water, enabling pressure and flow rate to be monitored over time (Figure 3.11). The resultant plots of column height versus time were converted into an average permeability according to the following equations:

$$P = \rho g h$$

P is eye pressure [cmH_2O], ρis density of water [1 g/cm^3], g is gravitational acceleration [9.8 m/s^2], and h is the height of the water column [cm].

Figure 3.11: Experimental setup for permeation testing of enucleated porcine eyes with and without implants. Water columns of up to 28 cmH_2O were inserted via syringe into the eyeballs and monitored over time to simultaneously record pressure and flow rate.

By geometry, the height of the water column relates to the volume of water:

$$h = \frac{V}{\pi \cdot r^2}$$

Where r is the inner radius of the column tube. The loss of water from the eye is assumed to be a linear function of permeability K and pressure P, giving the relations:

$$\frac{dV}{dt} = -K \cdot P = -K \cdot \rho g \frac{V}{\pi \cdot r^2}$$

Or alternatively, in terms of the column height:

$$\pi \cdot r^2 \frac{dh}{dt} = -K \cdot \rho g h$$

This can be solved for the column height over time:

$$h(t) = h_0 e^{\frac{-K \cdot \rho g}{\pi \cdot r^2} t}$$

By fitting the data with the model, the value of the permeation constant K can be obtained with respect to the time constant τ:

$$K = \frac{\pi r^2}{\tau \rho g}$$

Error! Reference source not found. plots the measured permeation for eyes with and without implants. No significant difference was observed, suggesting a sufficiently robust seal. For comparison, human eyes have a permeation of 9.6 µl/hr/mmHg [132].

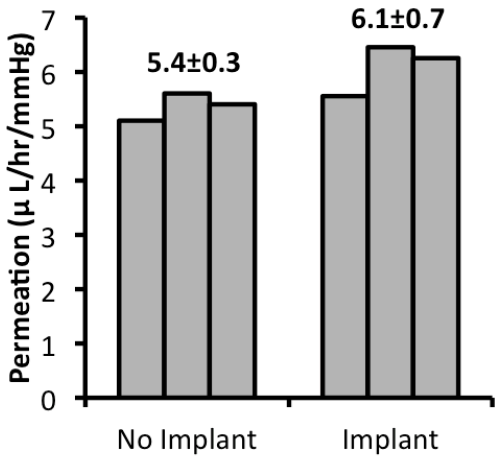

Figure 3.12: Permeation rates with and without implants (n=3) with overlaid standard deviation. The difference of 0.7 µl/hr/mmHg between the groups was not statistically significant by T-test (P > 0.05).

The enucleated porcine eye, with a measured permeation of 5.4 μl/hr/mmHg, provides a reasonable model. Specifically, the contribution of leakage around the device of 0.7 μl/hr/mmHg (*i.e.* the difference in permeation with and without the implant) is probably quite accurate since this permeation route is mechanical in nature and not dependent on cellular or physiological processes. Another factor that may have contributed to the differences in permeation rates is that the porcine model eliminated evaporative mechanisms of fluid loss, where as the human measurements would have had these occurring.

In Vivo Validation of GTLS Implant

In order to validate the safety of the implantation process, the efficacy of the skirt sealing in preventing leakage, stability of implant anchoring, and safety of constant phototherapy, in vivo testing was carried out. Devices were implanted into the eyes of young albino New Zealand rabbits (n=2). Animals were anesthetized by an intramuscular injection of Ketamine/Xylazine in conjunction with 1-2 eye drops of 0.5% Tetracaine to numb the ocular region. Eye drops of Tropicamide/Phenylephrine dilated the pupil. Partial peritomy was done on the temporal side of the conjunctiva before a 2.5mm sclerotomy was made at the pars plana (2.5mm away from the limbus); the tritium device was inserted into the incision. Once in position, the device was pressed gently to lock it in place via skirt deployment. The conjunctiva was subsequently used to cover the implant and closed with a 6-0 vicryl suture (Figure 3.13). All wounds were coated with antibiotic ointment. Surgery times were between 10-15min. The animals were monitored until they awoke and then returned back to their cages for recovery.

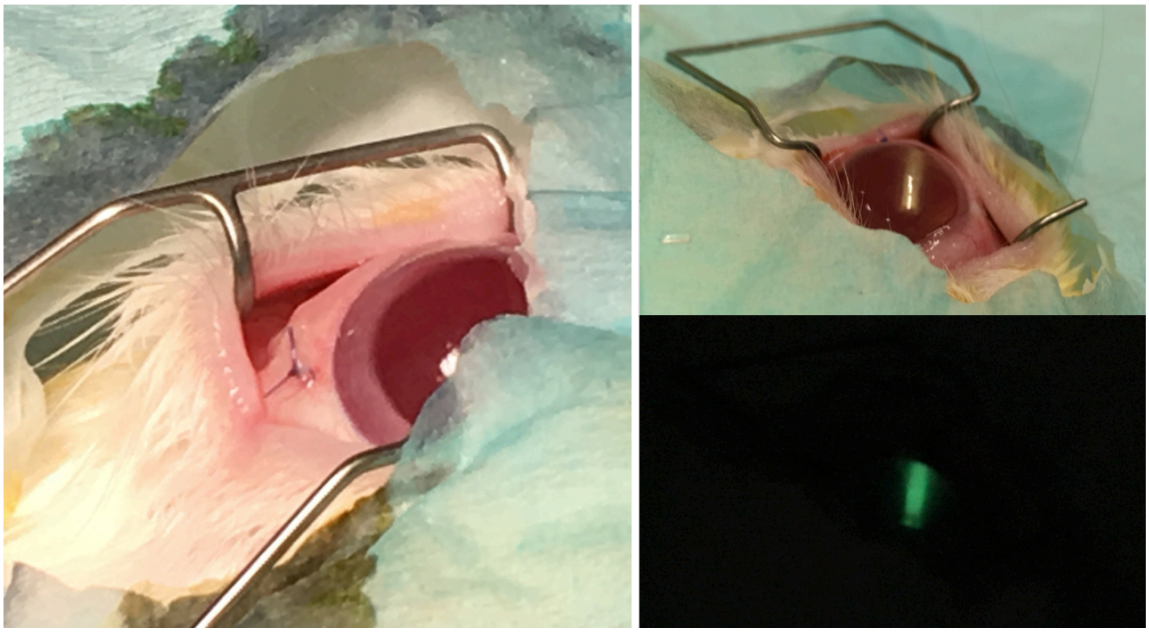

Figure 3.13: In vivo implantation of device into rabbit eye. A) Device back-plate arms have been trimmed and covered with the conjunctival flap then sutured closed. B) Side view of GTLS within the rabbit eye with lights on C) and with lights off to visualize the radioluminescence.

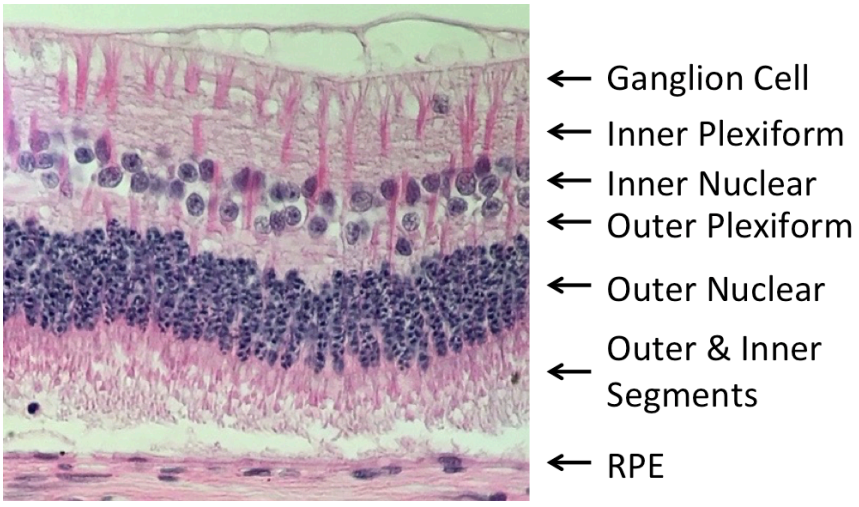

Figure 3.14: Histology of retina at 4 weeks post implantation using hematoxylin and eosin staining. Layers of the retina are observed to be normal and show no adverse changes to the retina.

A weekly follow-up revealed no adverse effects or changes in animal behavior. At 4 weeks post implantation the animals were euthanized by IV injection of pentobarbital. Histological examination of eyeballs stained with H&E found no adverse changes to the retina (Figure 3.14).

Intrinsically Photosensitive Retinal Ganglion Cells

Intrinsically photosensitive retinal ganglion cells (ipRGCs) signal ambient light levels and represent a third class of photoreceptors, distinct from rods and cones. These neural cells contain melanopsin, a light sensitive protein with a peak absorbance of 480 nm, which allows them to detect light. The role of ipRGCs includes: reporting length of day-night cycles for circadian rhythm, controlling pupillary state, and regulating melatonin production [133]. Irradiance response curves for ipRGCs have an IR_{50} of 3.25×10^{12} photons/cm^2/s for M1-phenotype and an IR_{50} of 3.44×10^{13} photons/cm^2/s) for M2-phenotype [134]. Given that phototherapy is on the order of 10^{10} to 10^{11} photons/cm^2/s, well below even the IR_{10}, it is unlikely that low-level phototherapy will have adverse effects on ipRGCs and their respective functions.

The shedding of photoreceptor outer segments is a critical process for maintaining vision that dependent on the circadian rhythm [135]. Shedding of rod cells peaks at onset of light, where as cone outer segments are shed at onset of darkness. Given that ipRGCs entrain circadian rhythm, the shedding of photoreceptors should proceed normally.

CHAPTER 4 – Phototherapy Contact Lenses

Key Take-Aways
• Phototherapeutic overnight contact lenses provide a non-invasive option for hypoxic retinal diseases like diabetic retinopathy. • Pupil constriction during sleep requires centering light sources on the optical axis • Radioluminescent contact lenses offer a long-term, reusable solution; chemiluminescent contact lenses offer a short-term, disposable solution

Towards Smart Lenses

Contact lenses have had a long history in medicine with the first glass lenses being fitted in the 1880s in Germany for the treatment of keratoconus and later myopia with the introduction of optically powered lenses [18]. The development of PMMA and discovery of its biocompatibility led to its use in contact lenses around the 1940s. Soft lenses first appeared in the 1960s based on poly-HEMA and silicone elastomers, providing improved comfort. Rigid gas permeable lenses developed in the 1970s marked a significant improvement over PMMA by providing oxygenation to the cornea, thereby enabling overnight orthokeratology lenses in the 1980s-1990s. Disposable lenses began to be market in the 1990s followed by the introduction of silicone hydrogel lenses around 2000. Myopia control lenses appeared in the 2010s. Since then researchers and companies have been experimenting with integrating diagnostic sensors (*e.g.* glucose

monitoring) and drug delivery into contact lenses in a push towards multifunctional smart lenses.

Contact lenses provide an excellent platform for phototherapy in that they are relatively non-invasive, well accepted, and can localize the light emitting elements directly into the optical path of the eye. This chapter summarizes the development of phototherapeutic contact lens options.

Choice of Light Source and Wear Considerations

There are several aspect that should be consider regarding the light source used in a phototherapeutic contact lens:

- Disposable or re-usable contact lens platform
- Passive or active lighting system
- Range and tunability of light intensity
- Risk of failure and safety
- Size of light source
- Impact on user routine
- Cost

From the available means of light production, three options were identified as feasible, namely gaseous tritium light sources (GTLS), chemiluminescence, and light emitting diodes. Table 4.1 describes the pros/cons and target application for each. Note that contact lenses based on light emitting diodes are developed in Chapter 5.

Table 4.1: Pros, cons, and use cases for GTLS, LED, and chemiluminescence lighting strategies in phototherapeutic contact lenses.

Radioluminescence / GTLS	
Pro	Provides constant light output for several years, obviating the need for recharging over the life of the lens. Manufacturers can produce sources in sizes down to 300 μm diameter, making them feasible for integration into a contact lens. The glass encapsulation provides optimal biocompatibility.
Con	The sources emit moderate light intensity and may require multiple elements to achieve sufficient retinal irradiance. The glass encapsulation is rigid and fragile at only 100 μm thick. The tritium is a radiation hazard if the sources are broken and requires proper disposal.
Use	May find application in a re-usable, rigid contact lens.

Chemiluminescence	
Pro	Provides medium light output for periods of hours, depending on geometry. Often in a two-component liquid system allowing flexibility in geometry.
Con	Chemicals are irritants. Irreversible reaction.
Use	May find application in disposable soft lenses.

Light Emitting Diode	
Pro	Provides variable and controllable light output in terms of both intensity and frequency with appropriate circuitry. Available in package sizes down to 0.65 mm × 0.35 mm × 0.2 mm, making them feasible for integration into a contact lens. Single LED can provide ample light output. Mechanically robust.
Con	Require electrical circuitry, which is susceptible to degradation. May contain toxic materials (*e.g.* heavy metals).
Use	May find application in disposable or short-term re-usable soft or hard lenses.

Pupillary Constriction During Sleep

The pupil constricts during sleep and with age. Since light entering the eye must pass through the pupil, a larger diameter is preferable for treatment with phototherapy. Two muscles control the size of the pupil: the iris sphincter muscle (constricts pupil under parasympathetic tone) and the iris dilator muscle (dilates pupil under sympathetic tone). The combination of reduced inhibition of the oculomotor nucleus

(parasympathetic) and reduced sympathetic tone during sleep and drowsiness leads to pupil constriction [103].

Through pharmacological intervention it is possible to overcome the sleep-induced miosis [136], [137]. Anticholinergic mydriatics (*e.g.* atropine, tropicamide) are a class of compounds that block parasympathetic activity and prevent constriction of the ciliary muscle leading to pupil dilation. Sympathomimetics (*e.g.* phenylephrine, 4-hydroxyamphetamine) are compounds that act as agonists to the sympathetic nervous system, inducing contraction of the iris dilator muscle and thereby pupil dilation. The use of these compounds separately or in conjunction provides a means of dilating the pupil to improve the phototherapeutic dose transmitted through the pupil unto the retina. Care should be taken to ensure complications are managed appropriately (*e.g.* elevated intraocular pressure is a known side-effect). Mydriatics are contraindicated for some patients [138].

Light Emission Measurements from GTLS Contact Lens

All measurements of light emission were carried out with a Newport Power Meter (Model 1936-R) with photosensor wand (918D-ST-UV). A contact lens containing 24× T-6915 GTLS (300 μm diameter, 2 mm length) with green phosphor arranged in a spoke pattern around a 3 mm central pupil was prepared as described subsequently in section, "2-Part Mold". Measurements of light intensity were made with and without a metallic reflector (aluminum foil) placed on the front of the lens both as a function of distance from the lens and as a function of angle.

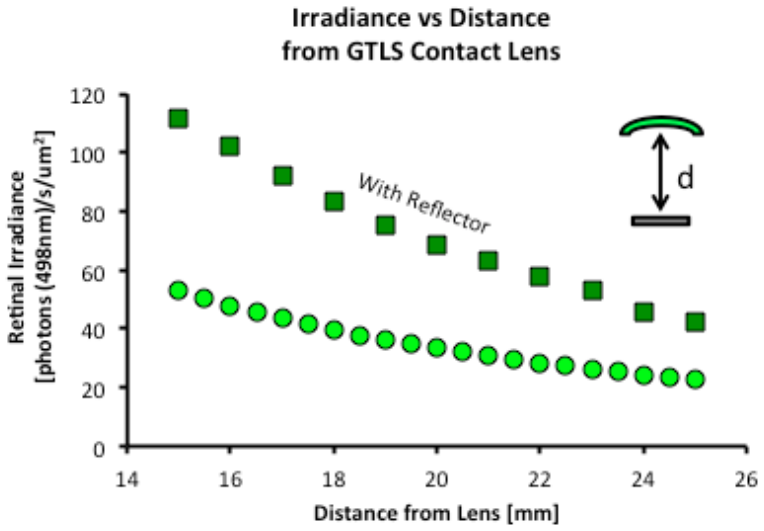

Figure 4.1: Photon irradiance on detector as a function of perpendicular distance from the GTLS lens, with (upper) and without (lower) metallic reflector. Ratio of intensity with and without reflector is approximately twice.

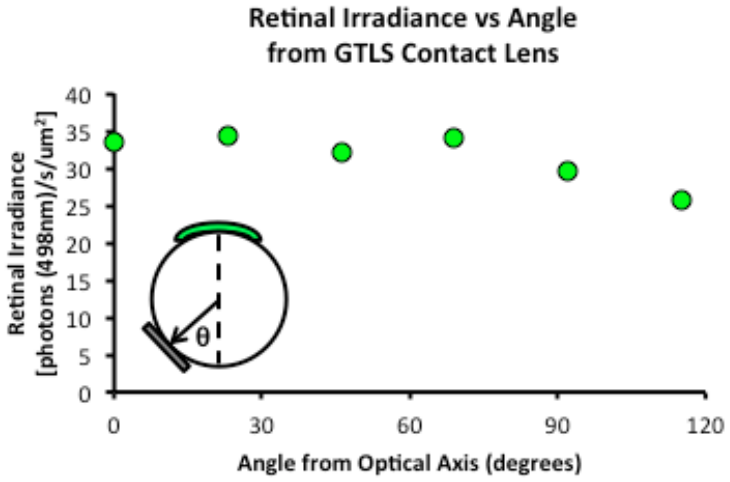

Figure 4.2: Photon irradiance on detector as a function of angular position from the optical axis around a 25 mm sphere produced by a GTLS lens with metallic reflector.

Measurement of irradiance versus distance was carried out in a similar setup as described in section, “Irradiance vs. Distance from GTLS”. To measure irradiance as a function of angle, the setup was modified slightly by affixing the lens to a pivot arm in such a way that its orientation angle could be adjusted. Utilizing a micrometer stage, and a 25 mm sphere centered over the photodetector, the lens was positioned tangentially around the sphere, the sphere was removed, and measurements were made (Figure 4.3).

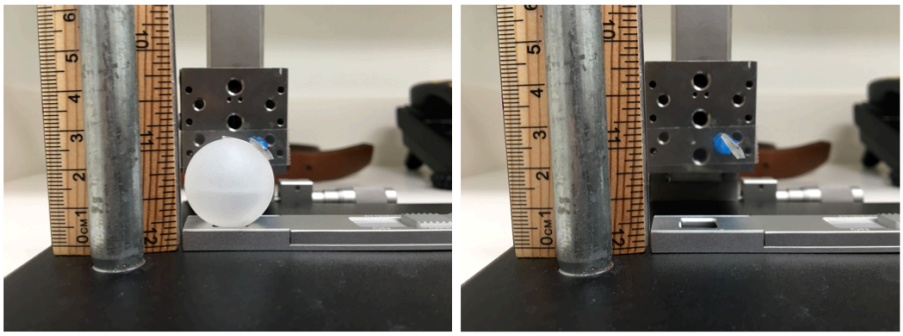

Figure 4.3: Setup to measure light intensity as a function of angle. (Left) The lens is positioned via a micrometer stage onto a 25mm sphere at various positions. (Right) The sphere is removed and the measurement is made with the photodetector.

Results indicate that the use of a metallic reflector effectively doubles the light directed towards the retina from the GTLSs. The design and geometry of the reflector is important though. In a separate set of experiments, titanium was deposited via electron-beam physical vapour deposition directly onto the back half of cylindrical GTLSs (Figure 4.8) to act as a reflector but no measureable improvement in light output was observed. In such geometry, most reflected light is directed back into the light source itself and may be lost due to absorbance within the phosphor. Generally, the irradiance as a function of angular retinal position is relatively constant, with proximity effects approximately balancing projected area effects.

Design & Fabrication of GTLS Lenses

2-Part Molding Process

A preliminary version of a phototherapeutic contact lens was fabricated by embedding 24 GTLS sources into medical grade PDMS (MED4-4210) through a two-step, two-part molding process (Figure 4.4). In the first step, the front face of the lens is cast with PDMS in mold B, with mold A imprinting alignment grooves, and partially cured (5 min, 100 °C). In the second step, the GTLS are positioned in alignment grooves and tacked in place with a dab of PDMS and partial cure (5 min, 100 °C). In the third step, with lens remaining in mold B, the back face of the lens is cast with PDMS by mold C and fully cured (12 hr, 100 °C). The lens in then removed from the mold and subject to acetone leaching (3×12 hr, 55 °C) to remove any unreacted monomer.

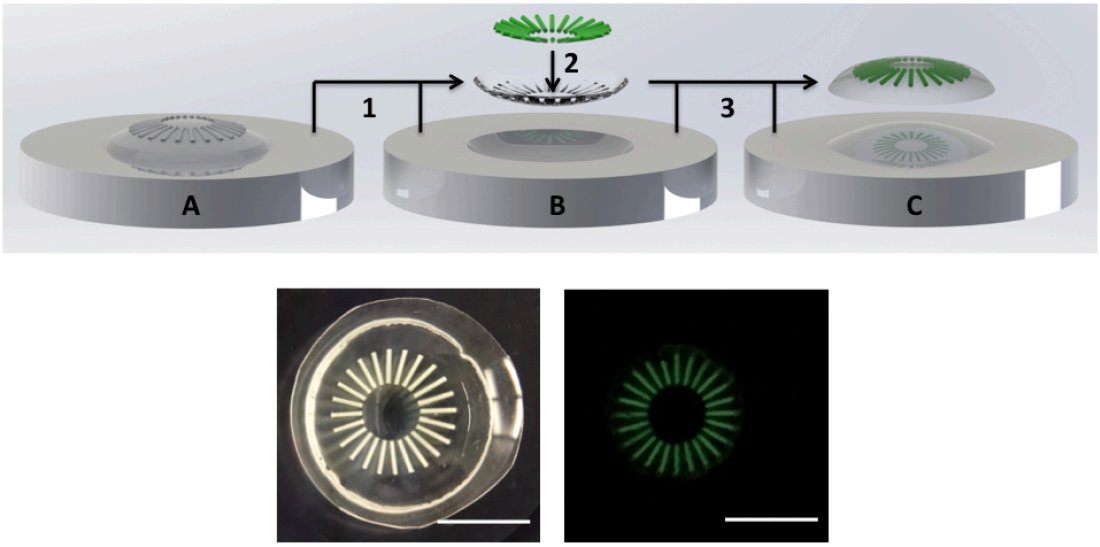

Figure 4.4: (Top) Phototherapeutic GTLS contact lens fabrication through 2-step, 2-part moulding process. (Bottom) Images of lens under light and dark conditions. Scale bar 5 mm.

The design places the GTLS in an evenly spaced radial pattern starting at r =1.5 mm and ending at r = 3.5 mm. This annular arrangement of light sources in the lens was intended to provide an unobstructed view during photopic vision when the pupil is contracted (<3 mm D), while directing the complete phototherapeutic dose through the dilated pupil (>7 mm D) under scotopic vision (Figure 4). The lens was 500 μm thick.

In Vivo ERG Results with GTLS Lens

The bioactivity of the GTLS lens was investigated through electroretinogram (ERG) flash response recordings in New Zealand rabbits. Animals were anesthetized by intramuscular injection of Ketamine/Xylazine and dark-adapted for 20 min prior to measurements. The ERG setup (HMsERG system, OcuScience LLC, USA) utilized DLT Plus Electrodes^{TM} (LKC Technologies, USA) and was designed for rabbit use. Scotopic ERG was performed with flash intensities of 0.1, 0.3, 1, 3, 10, and 25 cd·s/m^2, with no background illumination. The phototherapeutic contact lens was put in the eye of the rabbit with a control contact lens (no GTLS but otherwise identical) placed in the contralateral eye. Following the first set of recordings, the lenses were removed and swapped from each eye to the other, and then a second set of identical recordings was taken. This procedure ensured that observed differences between ERGs were genuine and not artifacts of system setup or animal.

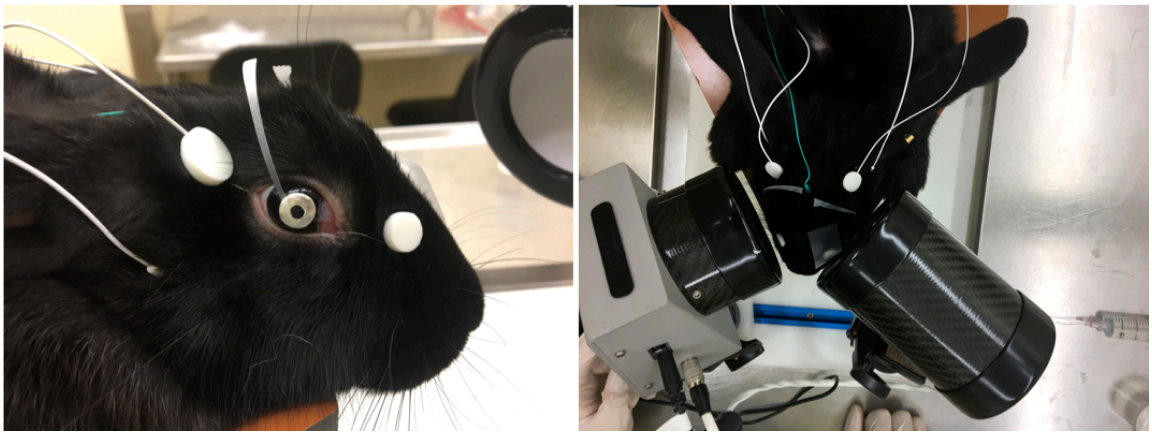

Figure 4.5: ERG of rabbit wearing GTLS contact lens with reflector and control lens.

The dark adapted ERG response arises from the closure of sodium channels in the rod outer segment in response to a flash of light [139]. Closure of channels reduces the circulating dark current and hence results in a negative deflection in the recording. For a given flash intensity, the magnitude of the a-wave is proportional to the dark-adapted state of the rod, since a less dark-adapted rod has a smaller circulating current to begin with. Thus comparison of the a-waves of ERGs gives information as to the magnitude of the circulating dark current and hence metabolic state of the rod. The hyperpolarization of the rod is transmitted downstream to the bipolar cells, which are mostly responsible for the b-wave due to the extrusion of potassium. The magnitude of the b-wave is generally much greater than that of the a-wave, which makes it more prominent and easier to measure. Not surprisingly, the magnitudes of the two waves are approximately proportional to one another ($\frac{\Delta b}{\Delta a}$ =0.8-1.2) [140] and so the b-wave can also be used as a proxy for rod metabolism.

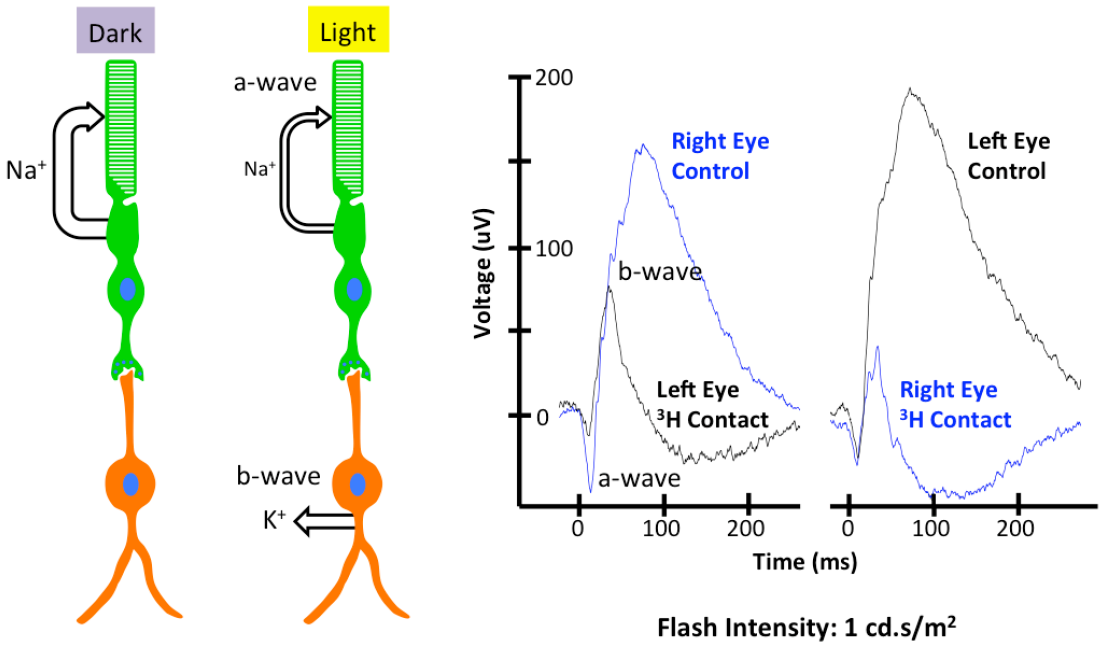

Figure 4.6: Electroretinogram with and without GTLS contact lens. (Left) Schematic of ERG origin. The circulating Na^+ current in rod outer segment is suppressed when incident photons cause the closure of ion channels in the outer segment. A negative deflecting a-wave is measured, which has a magnitude proportional to the number of channels closed in response to the flash. The hyperpolarization of the rod in response to light flash causes downstream signaling, which results in the positive deflecting b-wave, partly due to K^+ release from the rod bipolar cell. (Right) Pair of representative ERGs at a flash intensity of 1 cd·s/m^2 with GTLS contact lens and control lens in alternate eyes.

The ERG recordings were observed to be symmetrical across eyes, with notably suppressed b-wave amplitude in the eye treated with the phototherapeutic contact lens (Figure 4.6). The recordings were analyzed to extract salient features: both the amplitude and implicit time of the b-wave in the treated eye was found to be significantly shorter than in the untreated eye, a noted characteristic of suppressed dark adaptation [141].

Specifically looking at the difference in b-wave amplitude, the phototherapeutic contact lens induces an average suppression of rod cell dark adaptation to 32 ± 2 % of full dark adaptation.

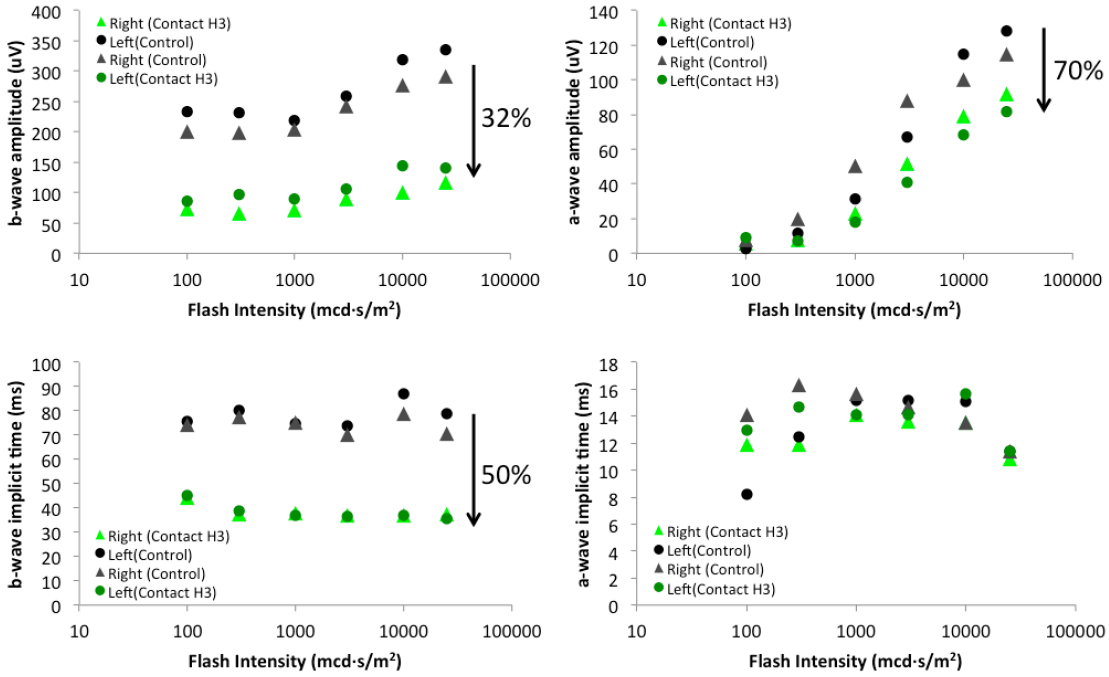

Figure 4.7: Quantification of ERG parameters (a-wave and b-wave amplitude and implicit time) as a function of flash intensity.

The expectation is for the degree of rod suppression to be larger in a rabbit model given the smaller size of the rabbit eye (18 mm axial length [142]) compared to a human eye (24 mm axial length [143]). Accounting for the anatomical differences, rabbit retinal irradiance from the phototherapeutic contact lens is approximately 2× that expected in a human. Given the logarithmic nature of vision, the expected rod cell suppression in human use would be approximately 50%, which exceeds the design specification but is well within a tunable range. Human ERG data will need to be collected in the future to validate these estimates.

Conversion of Flash Intensity to Photon Count

The electroretinogram is initiated through a flash of light, commonly reported in $\frac{cd \cdot s}{m^2}$. To make these numbers more meaningful in comparison to the background illumination provided by the light emitting contact lens, the flash intensity $F_v \left[\frac{cd \cdot s}{m^2}\right]$ can be converted to units of $\left[\frac{photons}{\mu m^2}\right]$ according to the following equations:

$$F_p \left[\frac{photons}{m^2}\right] = (1.02 \times 10^{15}) \frac{A_p F_v \left[\frac{cd \cdot s}{m^2}\right]}{{D_r}^2}$$

$$F_p \left[\frac{photons}{\mu m^2}\right] = (1.02) \frac{A_p F_v \left[\frac{mcd \cdot s}{m^2}\right]}{{D_r}^2}$$

For a 7 mm diameter pupil, eyeball diameter D_r = 9.9mm for rabbit [142], and unobstructed area fraction of lens 0.9:

$$F_p \left[\frac{photons}{\mu m^2}\right] \cong 0.36 \cdot F_v \left[\frac{mcd \cdot s}{m^2}\right]$$

Dry-Film Molded Lenses with Suture Anchors

A modification to the previous phototherapeutic contact lens was made to maintain lens centration in overnight rabbit experiments. The PDMS lens was created in two parts that were bonded together with PDMS glue. Dry film photoresist molds of the top and bottom PDMS lens were made containing GTLS alignment grooves as well as 4 suture anchors spaced around the lens. Given the dry film thickness of 120 μm per layer, the grooves in the top lens were made 120 μm deep and the grooves in the top lens were made 240 μm deep, thereby accommodating the 300 μm diameter GTLS. The top and bottom of the lens each have a 120 μm thick PDMS outer surface, producing a lens 600 μm thick.

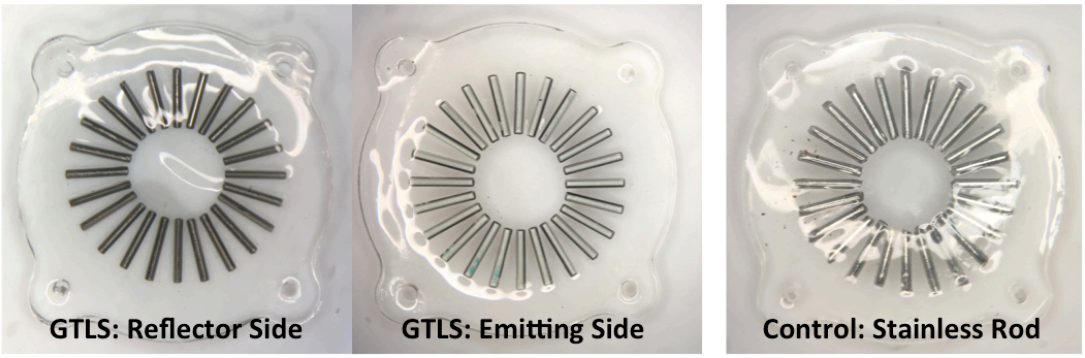

Figure 4.8: GTLS contact lens (left) and control lens (right) with suture holes to secure lens onto the rabbit eye for overnight studies.

To evaluate long-term wear, the lens was affixed to the cornea of a rabbit via suturing to the conjunctiva and left for 1 week (Figure 4.9). No problems with the contact lens were found following removal; however, tearing of the conjunctiva due to the sutures was observed. Additionally, the cornea was observed to have become cloudy and had significant loss of epithelium.

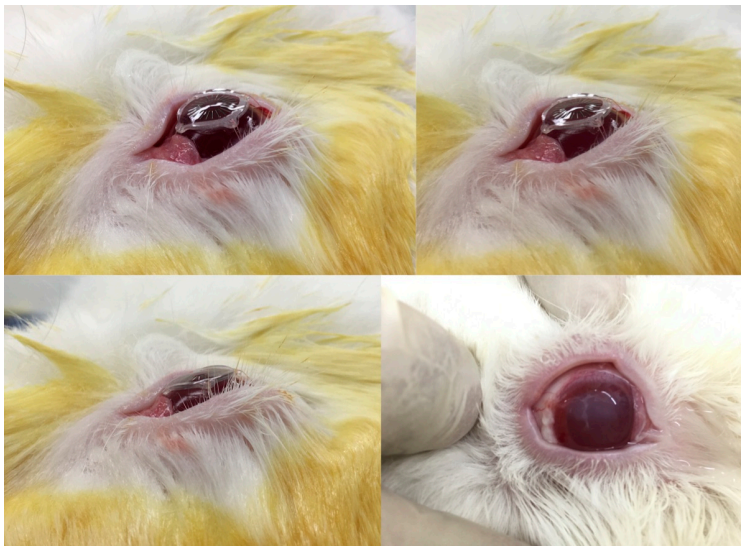

Figure 4.9: Weeklong contact lens wear via suturing to rabbit eye. (Bottom right) Corneal cloudiness observed underneath lens following removal.

The results of this study highlight the drawbacks of silicone-based contact lenses, which have a tendency to grip and cause traction on the cornea due to their innate hydrophobicity and compliance. These characteristics may have been the cause of the corneal cloudiness. While some of the challenges of long-term contact lens studies are unique to animal models (*e.g.* need to suture, unpredictable rubbing, lens hygiene), it is worthwhile investigating alternatives to silicone-based lenses.

Rigid Gas Permeable Lens Development

One of the concerns with PDMS-based lenses is that they are soft, which could lead to fracture of the encapsulated GTLSs. Furthermore, PDMS has a tendency to grip the eye due to its hydrophobic nature and this can lead to traction on the cornea. To overcome these drawbacks, rigid gas permeable (RGP) lens material was investigated, specifically HDS 100. RGP makes a trade-off in terms of oxygen permeability and compliance compared to silicone in order to achieve hydrophilicity. The material is relatively rigid compared to the compliance of the cornea but its innate hydrophilicity prevent it from gripping and therefore make it suitable for long term use.

A cavity-style hard contact lens, details of which are discussed in section "Cavity-Style Design for Smart Lens", was designed to be able to encase GTLSs and maintain a hydrophilic surface. Briefly, a pair of rigid-gas permeable lenses were designed such that they would form a cavity when stacked on top of each other. A 600 μm central cavity thickness was targeted to accommodate the 300 μm diameter cylindrical GTLSs within the curved lens geometry plus additional reflector and GTLS holder.

Table 4.2 summarizes the parameters of the lenses, which were turned by a certified lens manufacturer out of FDA approved RGP material. Optical coherence tomography scans of the stacked lenses with test wire (375 µm D × 2 mm L) verify the cavity geometry and fit (Figure 4.10). The cavity is >400 µm wide over a diameter of 7 mm, with a central width of 641 µm.

Table 4.2: Cavity-style contact lens parameters.

	Bottom Lens	**Top Lens**
Base Curvature Radius (BC)	8.39	6
Power (PWR)	+0.75	0
Diameter (DIA)	11.3	11.4
Back Optical Zone (BOZ)	6.2	7.3
Front Optical Zone (FOZ)	7.1	N/A
Central Thickness (CT)	0.18	0.18
Edge Thickness (ET)	0.15	0.15
Lens Material (MAT)	HDS 100	HDS 100

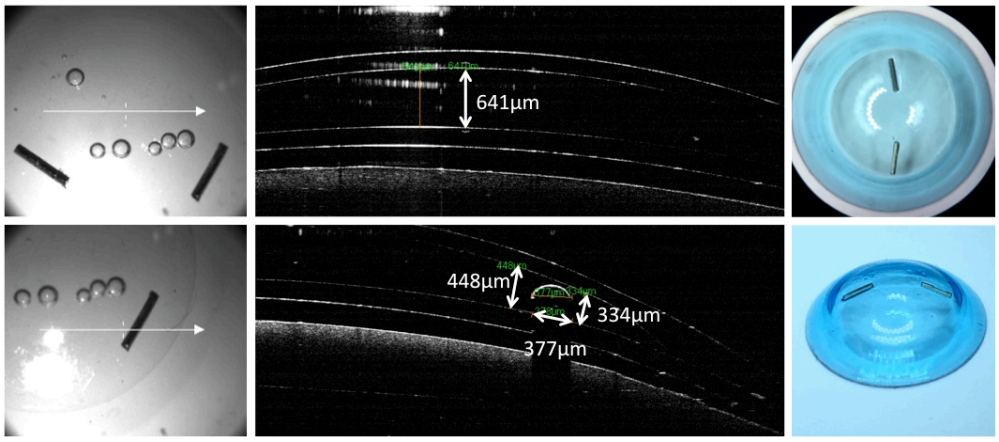

Figure 4.10: Optical coherence tomography of the cavity forming lens pair containing 375 µm D× 2 mm L wire pieces to validate fit. (Left) Optical image of top view of lens with overlaid OCT scan lines. (Center) Corresponding OCT scans with relevant dimensions overlaid. (Right) Images of paired lenses containing GTLS.

Overcoming Pupil Constriction During Sleep

Recent evidence that pupils constrict during sleep may undermine the effectiveness of the previous spoke-patterned GTLS design. To overcome this limitation, a new lighting arrangement was produced that concentrated the sources at the center of the lens with a small 500 μm pupil for vision.

In the limited studies that have looked at pupil size during sleep, one monitoring children ages 1 to 5 found that the average pupil diameter during deep sleep was 2.1 ± 0.5 mm while under dark-adapted awake conditions it was 6.1 ± 0.9 mm [103]. The pupil in older (61 ± 4.4 y) patients tends to be more constricted compared to younger (22.8 ± 4 y) individuals under both conditions of light-adaptation (65% relative area) and dark-adaptation (73% relative area) [105].

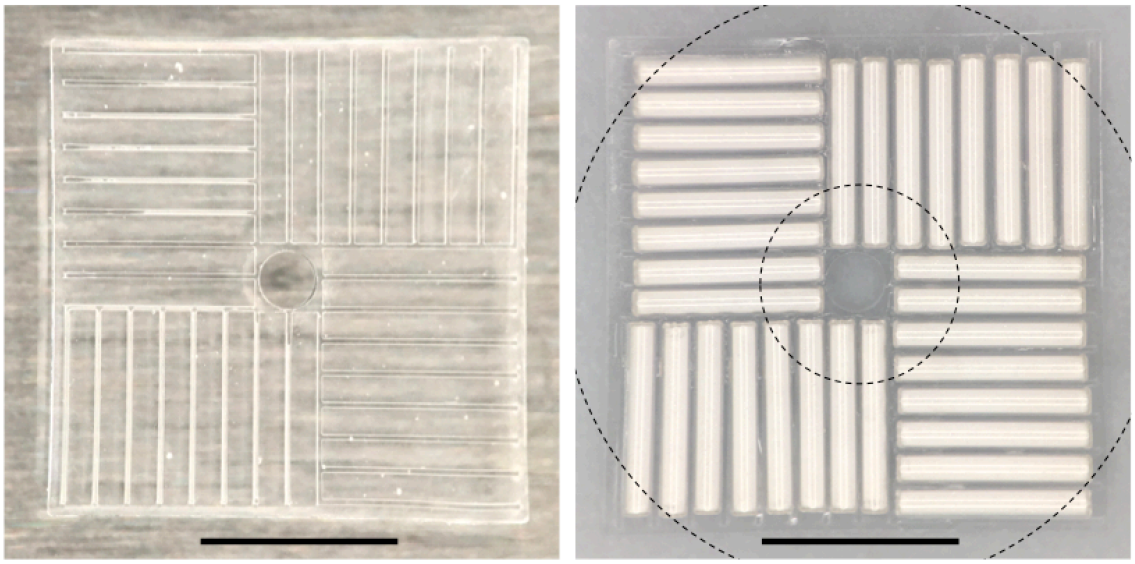

Figure 4.11: GTLS illumination element. (left) Microfabricated PDMS holder and spacer (right) with GTLS installed and overlaid average maximal (6 mm) and minimal (2 mm) pupil diameter during sleep.

The GTLS illumination element repositions light sources nearer the center of the lens so that the constricted pupil encircles a larger percentage of them. A 500 μm artificial pupil in the structure and corresponding reflector enables vision while wearing the lens. Under pupil dilation (6 mm D), almost all 32 sources are able to transmit light through the pupil, under partial dilation (4 mm D) the equivalent of 13 are able to, and under pupil constriction (2 mm D) the equivalent of 4 are able to.

The illumination element is composed of a PDMS aligner, which features spacing grooves to seat the GTLS evenly and ensure there is a path for gas diffusion between the sources. The aligner also has a 500 μm diameter hole in the center to maintain an optical path for vision and allow transmission of oxygen. GTLS are glued to the aligner on their inside end only, enabling the illumination element to be bent to fit the curved surface of the lens.

A reflector was electrochemically etched (detailed in section "Electrochemical Etching

Stainless Steel") out of stainless steel (0.001" thickness, 7 mm diameter) and shaped to match the curvature of the lens by forming over a stainless sphere (15 mm diameter). Tabs around the reflector pupil allow for it to be mechanically secured and centered on the PDMS aligner. Ruffles in the reflector prevent it from sealing off a portion of the lens cavity, thereby allowing gas to diffuse around it.

To form the completed cavity-lens, the light source assembly was first centered on the bottom lens. A bead of cyanoacrylate was applied along the inner surface of the top lens before bring the two lenses in contact, forming a peripheral bond between them

and a hollow gas cavity housing the GTLS lighting system. Figure 4.12 shows the completed lens under various illumination conditions.

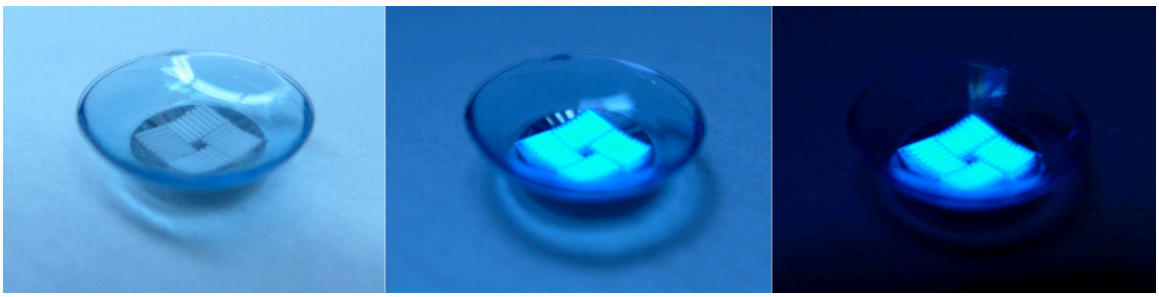

Figure 4.12: Cavity-style RGP lens with GTLS concentrated near the center of vision to maximize light entry through a constricted pupil, shown under various levels of illumination.

Orthokeratology for Improved Compliance

A major barrier to the success of preventative therapies is long-term patient compliance, which has plagued phototherapeutic sleep mask trials [95]. The same is likely to occur with phototherapeutic contact lenses without further modification. Patients may understand the long-term consequences of their disease and how nightly phototherapy can help treat it, but the disconnect between future benefits (*e.g.* preserved sight, reduced numbers of injections or rounds of laser treatment) and the nightly inconvenience they face putting in the lenses will gradually erode their compliance. Maintenance of such routines can be quickly jeopardized by even short-lived externalities (*e.g.* sickness, late-nights, travel), when it may be justified to stop utilizing the lenses temporarily, due to the slippery slope of procrastination. Generally, what is needed to sustain therapy is immediate feedback. There are three main types that play a role in medicine:

- External: A doctor, specialist, parent, or spouse monitors compliance with the therapy (*e.g.* a trainer motivating a patient to do exercises).
- Vitamins: Complying with the therapy provides an improvement to the quality of life of the patient. (*e.g.* feeling energized after a healthy meal)
- Painkillers: Complying with the therapy alleviates a negative symptom of the patient. (*e.g.* taking an anti-inflammatory pill for a sprain)

Studies have shown that compliance is almost always higher with the "painkiller" class of feedback [109], [110]. Therefore, I hypothesize what is needed to improve the compliance of phototherapy is the coupling of its preventive function to a painkilling function.

For contact lenses, the ability to correct vision (*e.g.* myopia) is an obvious painkilling function and the reason people tolerate the discomfort of putting in the lenses daily. However, phototherapy lenses provide no therapeutic benefit during the day when vision correction would be valued, and conversely vision-correcting lenses provide no benefit during sleep when phototherapy is valued. The coupling of preventative and painkilling functions requires that the vision-correcting feature occur during the night and last through the day. Miraculously, a little known means of vision correction known as orthokeratology does just that by utilizing specialized nightly contact lenses to reshape the cornea, providing patients with corrected vision daily even after lens removal [144]. Building on top of this platform could provide much improved patient compliance.

Orthokeratology has been around since the 1960s as a means of treating myopia, although only recent advances in lens materials and designs have seen it grow in popularity [145]. A practitioner prescribes the patient a pair of lenses with a central

curvature that is flatter than their corneal curvature such that some of the epithelial tissue is displaced peripherally, resulting in reduced corneal optical power (Figure 4.13). Reverse-curve geometry, with steeper mid-periphery secondary curve, allows the lens to come back into contact with the cornea and maintain centration of the lens. Modern orthokeratology lenses are worn during sleep to provide a sufficiently long period for corneal reshaping and are removed each morning. The corneal reshaping is transient and will revert back over 24 to 48 hours; however, with regular use corrected vision can be achieved.

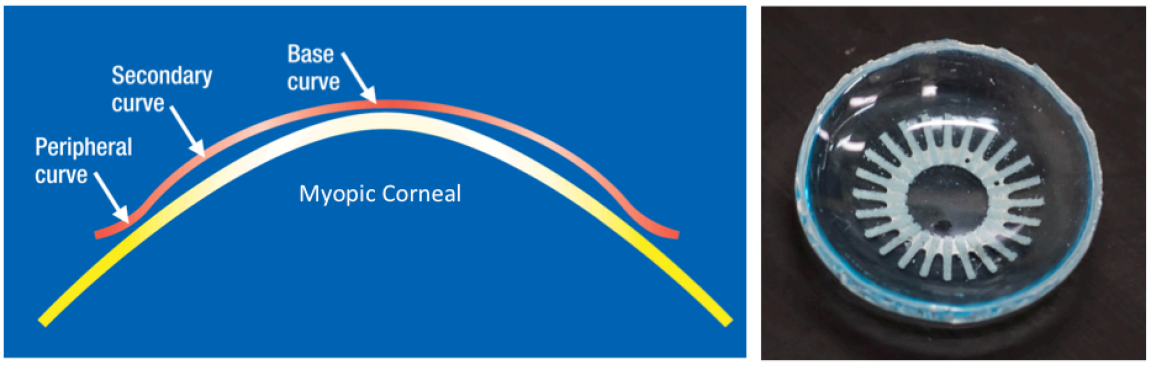

Figure 4.13: (Left) Orthokeratology lens profile, highlighting the relatively flat base curve and steep secondary curve. (Right) Phototherapeutic lens built on an orthokeratology lens platform.

The benefits (*e.g.* correct vision, no need for daily contacts/glasses) provided by orthokeratology provide strong incentive for patients to utilize them daily. In fact, orthokeratology has a >95% compliance rate among users [146]. By integrating phototherapy into an orthokeratology lens, it is likely that similar levels of compliance can be achieved within the sub-population of diabetics who are myopic (8.4 million in the USA, 1.4 million of which already wear contact lenses) [147]. As proof-of-concept, a prototype phototherapeutic orthokeratology lens was fabricated (Figure 4.13) by

encapsulating lighting elements and reflector in PDMS on a standard orthokeratology lens.

Evaluating Chemiluminescent Light Source

For short term and disposable applications, a chemiluminescent contact lens could be useful. This section presents a feasibility analysis and proof-of-concept.

A widely used chemiluminescent system involves (Figure 4.14) the oxidation of a phenyl oxalate ester with hydrogen peroxide under basic conditions to produce 1,2-dioxetanedione, which spontaneously decomposes to carbon dioxide, releasing energy that can excite a dye and thereby cause the emission of a photon [148]. Cyalume is the trade name of one such chemiluminescent system that is widely available and well characterized. Cyalume is composed of [149]:

- Phenyl oxalate ester (*e.g.* TCPO, CPPO)
- Dye (*e.g.* 9,10-Bis(phenylethynyl)anthracene)
- Solvent (*e.g.* alkyl phthalates, acetyl citrate esters, and alkyl benzoates)
- Base (*e.g.* sodium salicylate)
- Hydrogen peroxide

The safety of Cyalume has been evaluated in rabbits both by direct exposure of the nasolacrimal system and subcutaneous implantation for 30-40 days without toxic effects observed; however, subconjunctival, subtarsorrhaphic, and intra-aqueous exposure caused complications, although not at greater rates than commonly used contrast agents such as iophendylate [150]. Human response to Cyalume exposure has generally been found to be asymptomatic or transiently irritating [151]. Given the small volumes of chemiluminescent material anticipated, its isolation in a lens, and the low risk if exposure

does occur, it seems that a chemiluminescent lens could be feasible from a safety perspective.

For the present application, it is of interest to maintain a sufficient glow for a period of 8-10 hours. There are a couple of parameters that can be adjusted to tune the light intensity and duration:

- pH – Since the reaction involves base-catalyzed nucleophilic attack of the oxalate ester by hydrogen peroxide [149], making the solution more basic can accelerate the reaction while making the solution more acidic can retard the reaction.
- Mass Transport – Since the chemical components are separated into two parts, controlling the mixing of these components can be used to control the progression of the reaction.

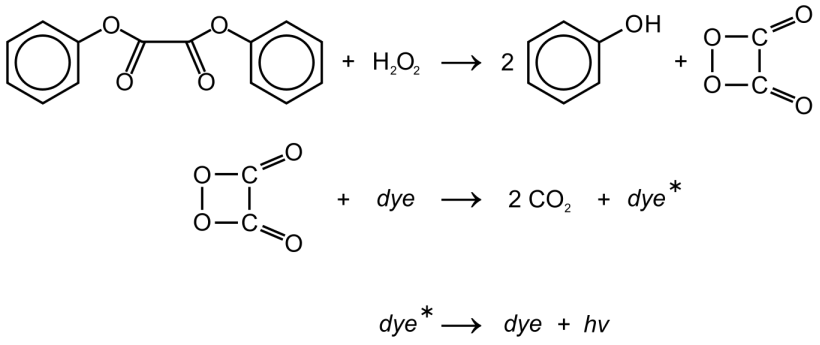

Figure 4.14: Chemiluminescent process in Cyalume system. Reprinted from [152]**.**

The light output kinetics of a Cyalume chemiluminescent system was investigated at 37 °C under different mixing ratios of Part A (fluorophore mixture) and Part B (peroxide mixture). Two different volumes were tested to evaluate the effect of self-absorbance on light output.

The components were measured, mixed, and added to a 6 well plate (15.3 mm diameter) as follows: 100 µL:100 µL, 67 µL:133 µL, 133 µL:67 µL, 200 µL:200 µL, 133

µL:267 µL, 267 µL:267 µL. The well plate was incubated at 37 °C between measurements. Measurements of light output were made using a Newport Power Meter (Model 1936-R) with photosensor wand (918D-ST-UV) by sequentially aligning each well over the detector area and recording the power at 498 nm. Figure 4.15 plots specific radiant power, which was converted from the raw data (in $\mu W/cm^2$), to compare the effectiveness of each mixture.

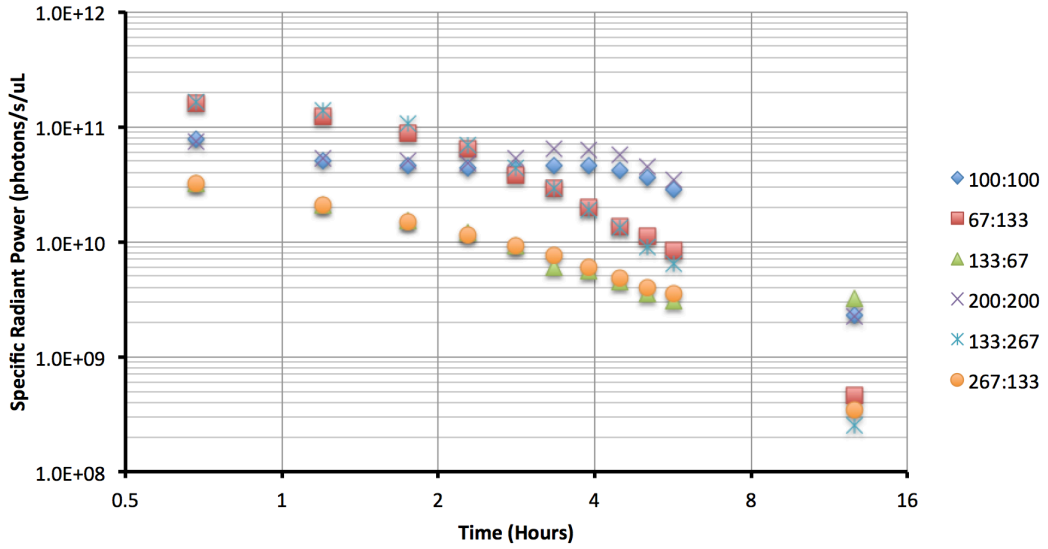

Figure 4.15: Evaluation of specific radiant power of Cyalume chemiluminescent system over time at 37°C. Legend indicates the volume ratio tested, µL Part A (fluorophore mixture) : µL Part B (peroxide mixture).

From a design perspective, an emission of 7×10^{11} photons/s/retina (600 photons/s/μm^2) is required to suppress rod dark current and maximally reduce metabolism. The 1:1 ratio is observed to provide the most uniform light output over time at approximately 5.6×10^{10} photons/s/µL over a 6 hour period. This puts the volume requirements of chemiluminescent components at around 12.5 µL, achievable within a

contact lens. One can also integrate the light output to calculate the photon energy emitted from the chemiluminescent components. For a 1:1 ratio, this is 600 μJ/μL.

The effect of self-absorbance on light output was found to be negligible, evidenced by the near overlap of curves (Figure 4.15) with the same ratio but different volumes (and hence thicknesses in the wells, 1.1 mm and 2.2 mm). Given that most contact lenses are <1 mm thick, self-absorbance will not constrain design even in the case of a reflector where path length could be doubled.

Prototype Chemiluminescent Lens

A prototype lens was fabricated to demonstrate proof-of-concept (Figure 4.16). The lens was composed of two PDMS halves, each with an annular reservoir, bonded to a circular thin (100 μm) glass septum. Part A (10 μL) and Part B (10 μL) of a Cyalume chemiluminescent system were separately loaded via syringe into the top and bottom reservoirs, respectively. Compression of the lens fractured the septum allowing the chemicals to mix and start the chemiluminescent reaction, which persisted over a 6hr period.

While this prototype provides proof-of-concept of the chemiluminescent lens, several additional aspects need to be addressed. Firstly, the septum preventing the mixture of chemiluminescent components should be fabricated out of a safer material than glass or utilize a different mechanism to reduce the hazard of a shard puncturing the lens. Secondly, the reservoirs should be made impermeable to the chemiluminescent chemicals. Thirdly, the kinetics of the light emission should be tuned to provide a more uniform emission over time. This could be accomplished using a diffusion-limited approach whereby the reservoirs are separated by a channel to slow mixing of the parts.

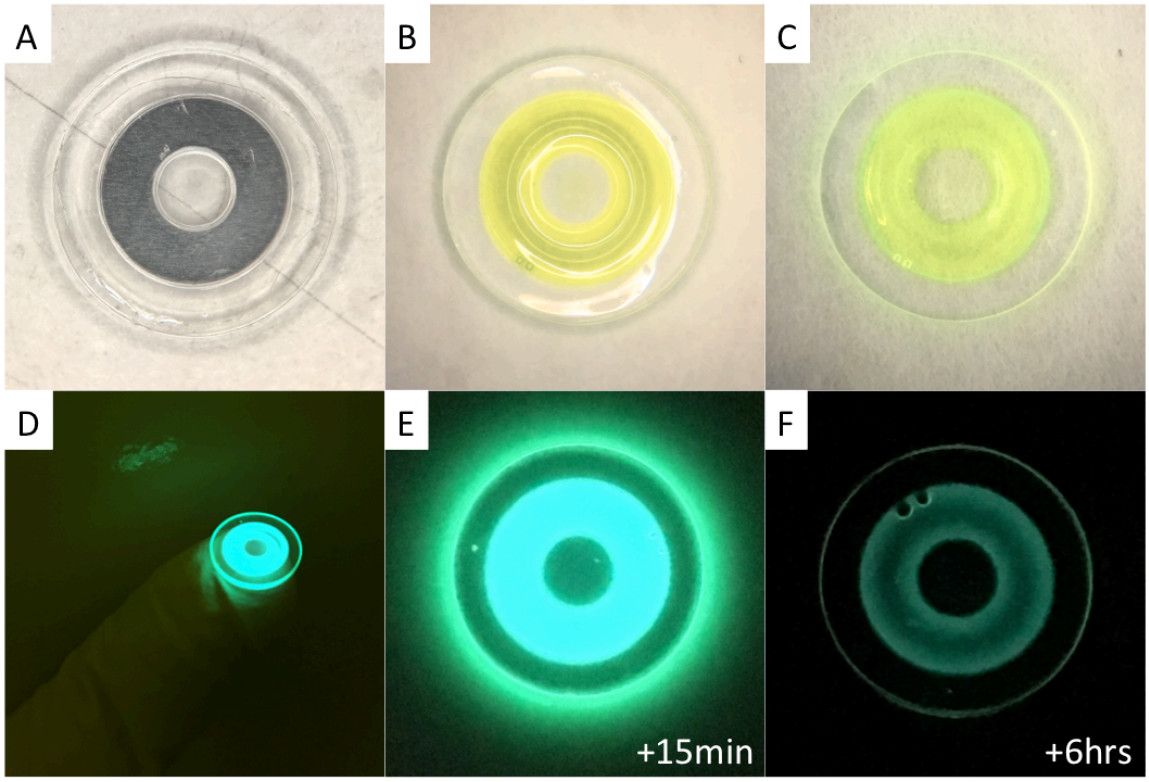

Figure 4.16: Chemiluminescent contact lens prototype. (A) Empty lens showing stainless reflector. (B) Reservoirs filled with chemiluminescent components. (C) Glass septum is broken allowing mixing and activation. (D) Activated lens on finger for scale. (E) Activated lens after 15min. (F) Activated lens after 6 hours.

CHAPTER 5 – Wirelessly Powered LED Contact Lens

The use of a light emitting diode as an illumination source could provide advantages over other schemes by allowing for active on/off/dimming control, reducing hazardous compounds, and having the benefits of an established ecosystem (*e.g.* manufacturing, hardware, software). Previous estimates of the operational power requirements (*e.g.* 280 nW of light divided by luminous efficiency) for the LED suggest that wireless powering, and optional onboard energy storage, would be appropriate. To this end, a prototype wirelessly powered contact lens was designed and built from stand-alone components as proof-of-concept. An application-specific integrated circuit (ASIC) could eventually be produced, miniaturizing, optimizing, and incorporating additional functionality.

LED Sourcing and Characterization

A 0201 green emitting LED, specifically the XZBGR155W5MAV LED (SunLED, CA, USA), was identified as a candidate light source due to its small profile (0.65×0.35×0.2 mm), peak wavelength (518 nm), wide viewing angle ($2\theta_{1/2}$ = 140°), luminous intensity (79 mcd @ I_F = 5 mA), and low toxicity profile (lead-free, InGaN emitter) [153]. The LED was soldered to 30 AWG tin-plated copper wire and embedded onto an ERG-Jet Contact Lens Electrode (Fabrinal Eye Care, Switzerland) using a 2-part epoxy (Figure 5.1).

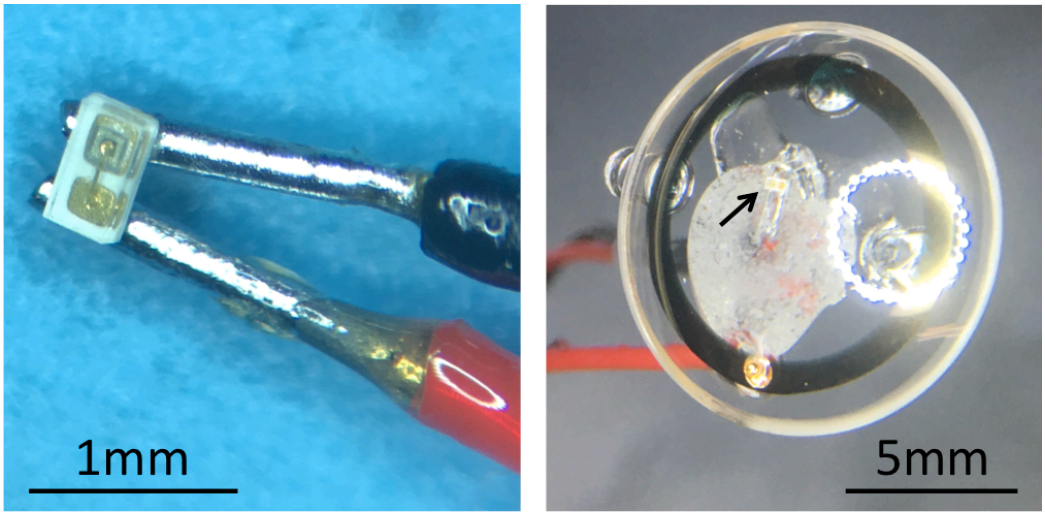

Figure 5.1: (left) XZBGR155W5MAV LED soldered to wire leads and (right) embedded onto ERG contact lens electrode with epoxy.

The light output from the LED was measured (Figure 5.2) at a distance of 25.4 mm from the photodetector under pulse width modulation driven at 5 V with a 27.39 kΩ current-limiting resistance in series (27 kΩ+390 Ω).

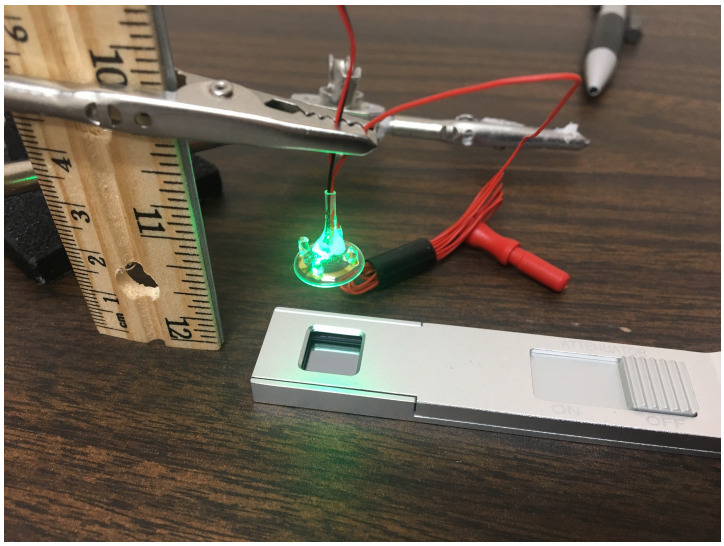

Figure 5.2: Experimental setup of light intensity measurements with irradiance from LED embedded contact lens measured by photodetector.

An Arduino Uno (Sain Smart, USA) was used to drive the LED with frequency 60 Hz and duty cycles ranging from 1 to 1/32768 = 0.5^{15}. The linearity of the response is observed in Figure 5.3, demonstrating control of photon irradiance over three orders of magnitude from 10 to 10,000 photons/μm^2/s. For a rabbit with a smaller eye diameter than the distance used in the measurements, the irradiance should be scaled by approximately $\left(\frac{D_{Measure}}{D_{Rabbit}}\right)^2 = \left(\frac{25.4\ mm}{18\ mm}\right)^2 \cong 2$.

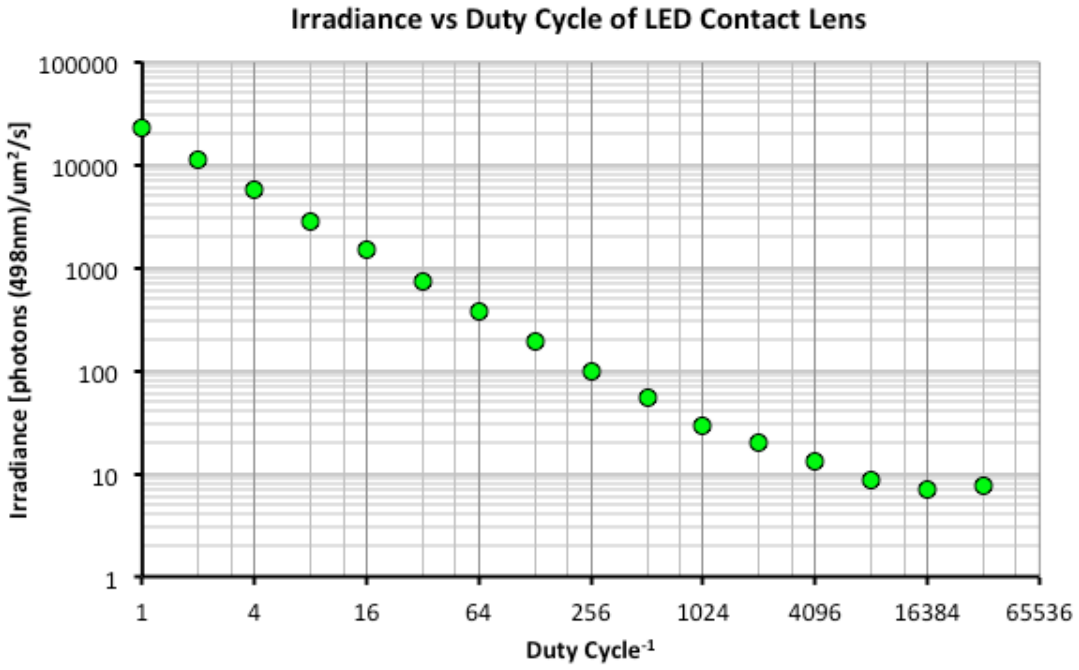

Figure 5.3: Irradiance from XZBGR155W5MAV LED at a distance of 25.4 mm. The LED is powered at 5 V with a 27.39 kΩ current-limiting resistance in series and driven via pulse width modulation using a microcrontroller.

In Vivo Characterization of Rod Suppression by LED

Similar ERG measurements were made using the LED contact lens setup to further understand the relationship between retinal irradiance and rod ERG, particularly b-wave suppression. The LED light intensity was varied using pulse width modulation with duty cycle of 0, 1/4096, 1/1024, 1/512, 1/256, 1/128, 1/32, 1/4, corresponding to approximate retinal irradiance of 0, 27, 59, 108, 198, 378, 1470, and 11446 photons/μm^2/s, respectively. The rabbit was dark adapted for 20 min prior to the start of the experiment. An unmodified ERG-Jet contact lens electrode served as a control in the right eye of the animal, while the LED modified ERG-Jet contact lens electrode was placed in the left eye (Figure 5.4).

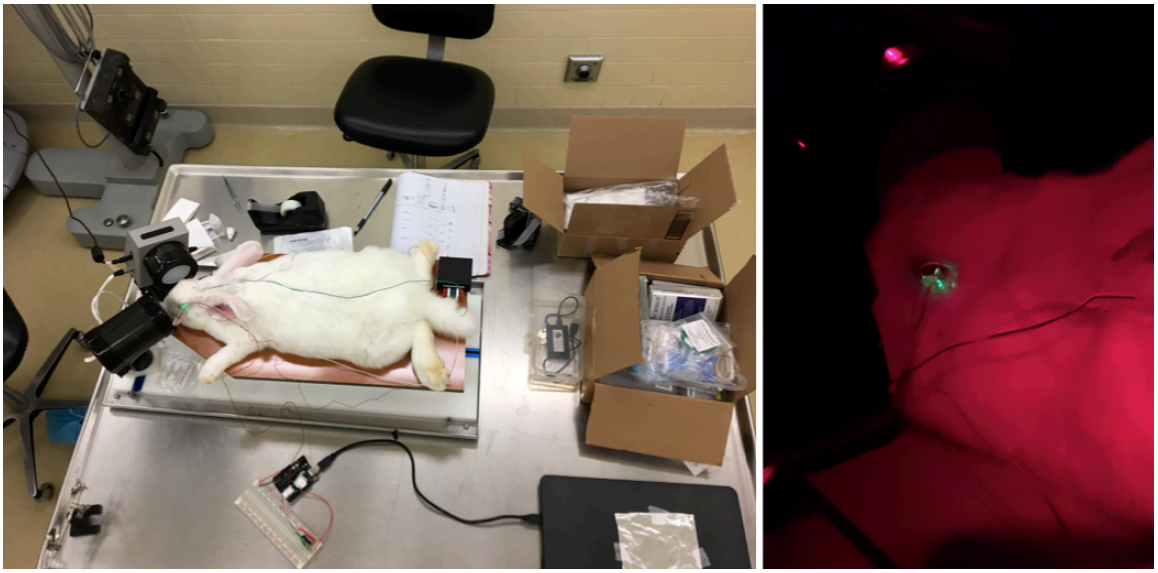

Figure 5.4: Experimental setup with rabbit, ERG, and LED contact lens used to determined the relationship between retinal illumination and rod dark current suppression.

A series of flash intensities were used over the experiment: 100, 30, 10, 3, and 1 mcd·s/m^2. Starting with the lowest flash intensity, a baseline ERG was taken (*i.e.* duty cycle = 0) with a pulse train of 5 flashes spaced 10 s apart. The LED duty cycle was increased to the next level and the pulse train was repeated. This was done for each level of LED intensity/duty cycle. Following a set of measurements, the animal was dark adapted for an additional 15min, the electrodes were repositioned if necessary, and the experiment was repeated with the next flash intensity. A representative series is depicted in Figure 5.5. This protocol was developed to ensure that steps in LED intensity could be compared. Previous protocols where flash intensity was stepped up within a series, while LED intensity was varied across series had too much variability due to animal motion, drift, and the need to reseat electrodes to allow for comparisons of LED intensity.

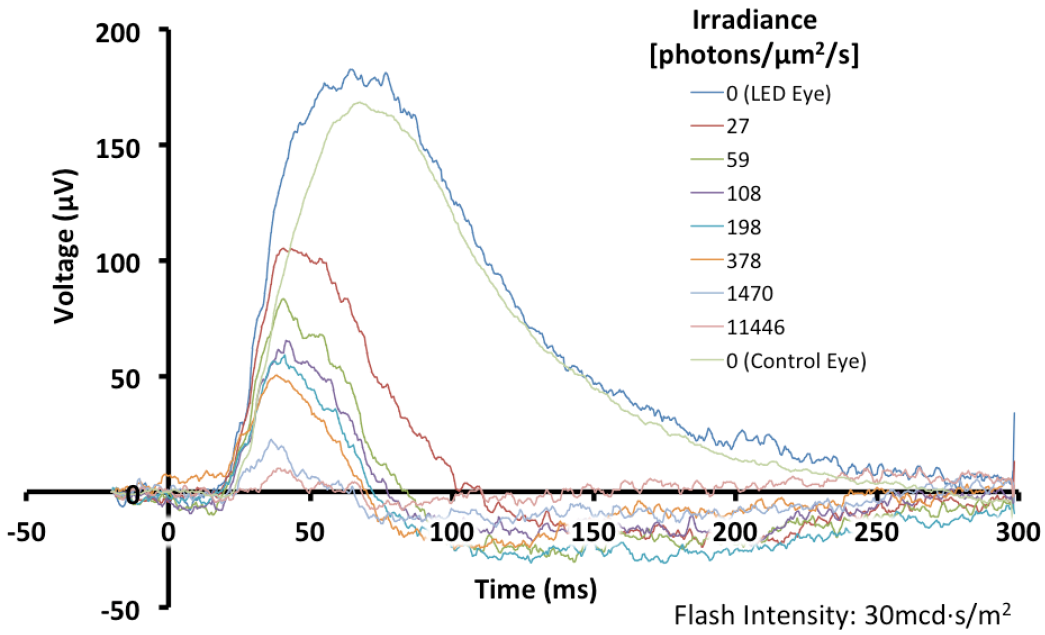

Figure 5.5: Representative series of ERGs with various LED irradiance at a flash intensity of 30 mcd·s/m^2.

From the series of ERG measurements, the b-wave amplitude was extracted and plotted as a function of LED duty cycle. On a semi-log plot the amplitude linearly decreases with duty cycle (Figure 5.6). For dim flash intensities of 1 or 3 mcd·s/m^2 the b-wave disappears at duty cycles of 1/1024 and 1/256, respectively as the flash is not sufficiently above noise.

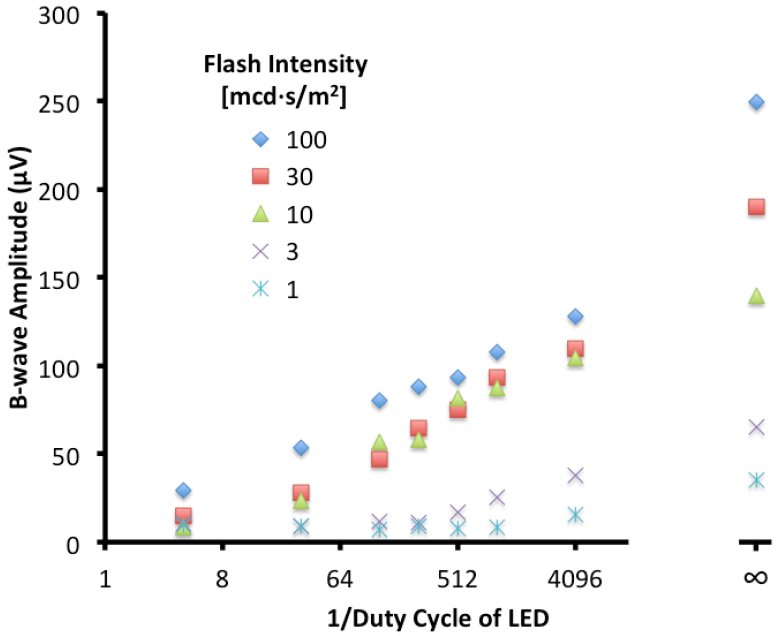

Figure 5.6: B-wave amplitude versus LED duty cycle over all flash intensities.

The retinal irradiance was estimated by converting the duty cycle from Figure 5.6 using data from Figure 5.3 and assuming an 18 mm rabbit eye diameter. Figure 5.7 plots the b-wave amplitudes, which were normalized by the amplitude of the b-wave with no irradiance. The calculated retinal irradiance for half-suppression of the b-wave was found by fitting a logarithmic curve to the data and calculating the y = 0.5 intercept, summarized in Table 5.1.

Table 5.1: Irradiance needed for 50% reduction in b-wave amplitude.

Flash Intensity [mcd·s/m^2]	Irradiance for 50% B-Wave [photons/µm^2/s]
100	26
30	60
10	144
3	44
1	24
Mean	60
Std. Dev.	50
SEM	20

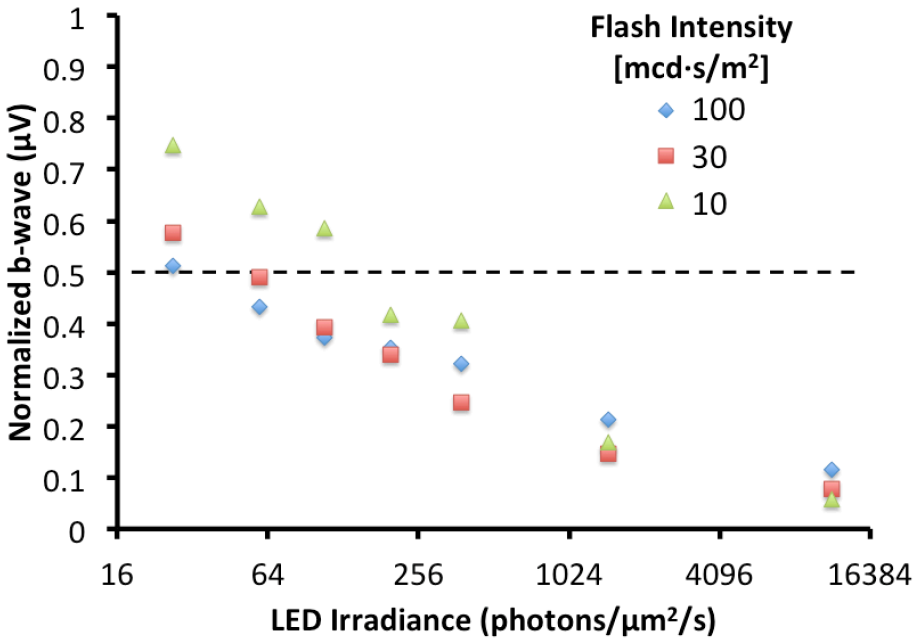

Figure 5.7: B-wave amplitude versus retinal irradiance from LED contact lens, normalized by the amplitude of the b-wave with no irradiance. Half-suppression of b-wave (dashed-line).

The necessary retinal irradiance for suppression of b-wave amplitude by 50% is therefore around 60 ± 20 (SEM) photons/µm^2/s in rabbit.

Wireless LED Contact Lens Development

For wireless power, there are specific frequency bands that are allowed/intended for industrial, scientific and medical (ISM) use. For example, a common band is 13.56 MHz, used often in near-field communication and radiofrequency identification. The band is attractive for wireless contact lens applications due to the simplicity of designing circuits to operate at this frequency, the availability of existing components and hardware, and the reasonable power that can be transferred.

For biological safety considerations, there are limits to the intensity of magnetic fields that humans can be continuously exposed to. The Federal Communications Commission regulations (47 CFR 1.13101.1310, radiofrequency radiation exposure limits) impose a limit of 4.89 [A/m] / f [MHz] for controlled exposure, specifically at 13.56 MHz: 0.36 [A/m] or 0.45 [μT].

Wireless power transfer systems commonly use inductive coupling between two resonant coils. Generally speaking, the design constraints on the primary, power-providing coil are minimal as it is external to the body. Primary coil design is well understood and summarized elsewhere [154], [155]. It is therefore assumed that such a coil system can be designed, built, and driven to achieve the maximum allowable magnetic field for powering the secondary coil.

Design Calculations and Considerations

On the secondary coil side, the goal is to produce a design able to develop the maximal voltage (or at least up to 3-4 V to power an LED) within the limits of a safe magnetic field strength. Faraday's Law states the voltage induced on a coil is

geometrically dependent on the number and cross sectional area of loops through which a time varying magnetic flux passes:

$$V_{pk} = -n \cdot \frac{d(B \cdot A)}{dt}$$

Clearly, maximizing number and size of loops will maximize induced voltage; however, there are geometrical, practical, and processing constraints that need to be considered. Firstly, the size of the coil needs to fit within a contact lens, limiting the coil geometry to a diameter around 6-10 mm diameter. Practically, single layer planar geometries are easiest to fabricate and preferable if they can satisfy the design requirements. From a process perspective, 100 μm features are robustly achievable, though smaller features could be made if necessary. Within these constraints, it is possible to produce a 10 mm outer diameter spiral coil with 10 turns composed of 100 μm wide traces with 100 μm spacing. A simple model for the inductance of a single-layer helical coil has been developed:

$$L = \frac{a^2 n^2}{9a + 10c}\ [\mu H]$$

where *a* is the average coil radius in inches, *c* is the span of the coil in inches, and *n* is the number of turns in the coil [156]. With these parameters, the resulting inductance is calculated to be 0.84 μH (Table 5.2) and the coil has a loop area of 5.25×10^{-4} m^2. At a frequency of 13.56 MHz, such a coil will generate a voltage of:

$$V_A = -n \cdot A \cdot 2\pi \cdot f \cdot B_0$$

$$V_A = (5.25\times10^{-4}\ m^2)(2\pi)(13.56\ MHz)(0.45\ \mu T) = 20\ mV$$

Table 5.2: Coil parameters used for calculation of inductance.

Parameter	Value
a	4mm (0.157”)
c	4mm (0.157”)
n	10.1
L	0.843μH

By combining the inductive coil in parallel with a suitable capacitor and the load, an RLC circuit is produced with a characteristic resonant frequency that is able to amplify this voltage significantly. The properties of this circuit (Figure 5.8) can be evaluated by nodal analysis.

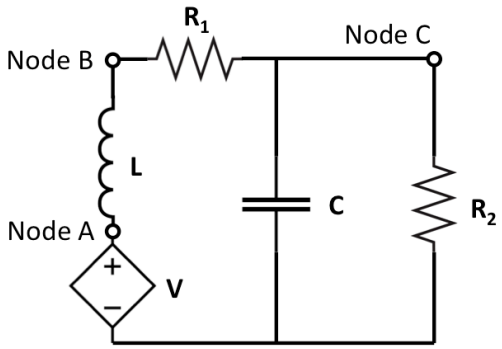

Figure 5.8: Circuit diagram of simple RLC model of a resonant coil with inductance L and resistance R_1 with parallel capacitor C and load R_2 in magnetic field inducing a voltage V.

Consider Kirchoff’s current law at each node:

$$\text{Node A: } V_A = -n \cdot A \cdot \omega \cdot B_0 \cdot \text{Re}\{e^{j\omega t}\}$$

$$\text{Node B: } \frac{V_A - V_B}{j\omega L} + \frac{V_C - V_B}{R_1} = 0$$

$$\text{Node C: } \frac{V_B - V_C}{R_1} - \frac{V_C}{\frac{1}{j\omega C}} - \frac{V_C}{R_2} = 0$$

Solving for V_B and V_C:

$$\frac{V_B}{V_A} = \frac{j\omega CR_1R_2 + R_1 + R_2}{R_1 + R_2 - CR_2L\omega^2 + j(\omega CR_1R_2 + \omega L)}$$

$$\frac{V_C}{V_A} = \frac{R_2}{R_1 + R_2 - CR_2L\omega^2 + j(\omega CR_1R_2 + \omega L)}$$

If we look at the voltage gain $\left|\frac{V_C}{V_A}\right|$ we have:

$$\left|\frac{V_C}{V_A}\right| = \frac{R_2}{\sqrt{C^2L^2R_2^2\omega^4 + C^2R_1^2R_2^2\omega^2 - 2CLR_2^2\omega^2 + L^2\omega^2 + R_1^2 + 2R_1R_2 + R_2^2}}$$

Which is maximized at ω for minimum denominator:

$$\frac{d}{d\omega}(C^2L^2R_2^2\omega^4 + C^2R_1^2R_2^2\omega^2 - 2CLR_2^2\omega^2 + L^2\omega^2 + R_1^2 + 2R_1R_2 + R_2^2) = 0$$

$$\omega_{resonance} = \frac{\sqrt{4CLR_2^2 - 2C^2R_1^2R_2^2 - 2L^2}}{2CLR_2}$$

In the limit that R_1 is small and the circuit is not loaded (*i.e.* $R_2 = \infty$), the resonance condition simplifies to:

$$\omega_{resonance} = \frac{1}{\sqrt{LC}}$$

Given an inductance of 0.83 μH for the coil as previously estimated, in order to achieve a resonant frequency of 13.56 MHz, a capacitor of the following value is required:

$$C = \frac{1}{(2\pi f)^2 L} = \frac{1}{(2\pi \cdot 13.56\ \text{MHz})^2 (0.843\ \mu\text{H})} = 163\ \text{pF}$$

Furthermore, the gain $\left|\frac{V_C}{V_A}\right|$ simplifies to:

$$\left|\frac{V_C}{V_A}\right| = \frac{1}{R_1}\sqrt{\frac{L}{C}} = \frac{\omega_{resonance} L}{R}$$

The assumption that R_2 is large so that loading is minimal is evaluated as follows. From earlier evaluation of the LED, we know that 1000 photons/μm^2/s is produced at 3.6 μA and consumes approximately 20 μW. For R_2 to consume a similar amount of power at 3 V, it would require a resistance of:

$$R_2 = \frac{\left(\frac{V}{\sqrt{2}}\right)^2}{P} = \frac{\left(\frac{3V}{\sqrt{2}}\right)^2}{20\ \mu W} = 225\ k\Omega$$

Therefore, the anticipated loading effect of an LED is minimal.

Regarding assumptions on R_1 being small it is important to consider the impact the skin effect has on trace resistance. Under alternating current conditions, current density skews towards the surface of a conductor due to opposing eddy currents arising from the alternating magnetic field induced by the alternating current. Current density drops off exponentially by a characteristic constant known as the skin depth, which is dependent on frequency [157]. The skin depth for copper at 13.56 MHz is around 17 μm (Table 5.3). For conductor dimensions greater than the skin depth, there are diminished returns with respect to conductance.

Table 5.3: Calculation of skin depth for copper.

Description	Symbol	Value
Resistivity of the conductor	ρ	16.78×10^{-9} Ω · m (20°C)
Frequency	f	13.56×10^{6} Hz
Absolute magnetic permeability of the conductor	$\mu = \mu_r\mu_0$	1.26×10^{-6} H/m
Skin Depth	$\delta = \sqrt{\frac{\rho}{\pi \cdot f \cdot \mu}}$	17.7 μm

The resistance R_1 of the coil due to skin effect under ac operation can be estimated from the equation [158]:

$$R_{AC}(f) = \frac{(2.16 \cdot 10^{-7})\sqrt{f\rho_R}}{2(w + d)}$$

Here, f is frequency [Hz], w and d are trace width and thickness [inch], and ρ_R is the relative resistance of the material compared to copper (*i.e.* Cu = 1). Given a coil length of roughly 250 [mm] (9.9”), and trace width of 100μm (0.0039”) and thickness of 35.5μm (0.0014” or 1oz Cu/ft^2), the resistance of the coil at 13.56 MHz can be estimated as:

$$R_{Coil}(13.56\ \text{MHz}) = \frac{(2.16 \cdot 10^{-7})\sqrt{13{,}560{,}000}}{2(0.0039'' + 0.0014'')} \cdot (9.9'') = 0.74\ \Omega$$

Therefore, the assumption that R_1 is small is reasonable. It follows that such a secondary coil, when operated under resonance will produce a voltage across the load of:

$$|V_C| = \left|\frac{V_C}{V_A}\right| \cdot |V_A| = \frac{\omega_{resonance} L}{R_1} \cdot (n \cdot A \cdot \omega_{resonance} \cdot B_0)$$

$$|V_C| = \frac{2\pi \cdot (13{,}560{,}000\ [\text{Hz}])(0.84\ [\mu\text{H}])}{0.74\ [\Omega]} \cdot (20\ [\text{mV}]) = 96 \cdot 20\ [\text{mV}] = 1.9\ [\text{V}]$$

In order to support an LED, the ac voltage can be rectified and boosted using a simple half-wave voltage doubling circuit (Figure 5.9). Under unloaded conditions, the output voltage is nominally $2\times(V_{pk}\text{-}V_d)$. Under intended operation the LED is expected to consume around 3.6 μA. The Shockley current equation for the diode states:

$$I = I_S\left(e^{n\frac{V_D}{\frac{kT}{q}}} - 1\right)$$

Assuming $I_S = 3 \cdot 10^{-7}$ A, $n = 2.2$, $\frac{kT}{q} = 0.026$ V, the expected voltage drop across the diodes can be calculated [159]:

$$V_D = n\frac{kT}{q}\ln\left(\frac{I}{I_S} + 1\right) = (2.2)(0.026\text{ V})\ln\left(\frac{3.6}{0.3} + 1\right) = 0.15\text{ [V]}$$

An output voltage of 2×(1.9 V-0.15 V) = 3.5 V is expected from the rectifier.

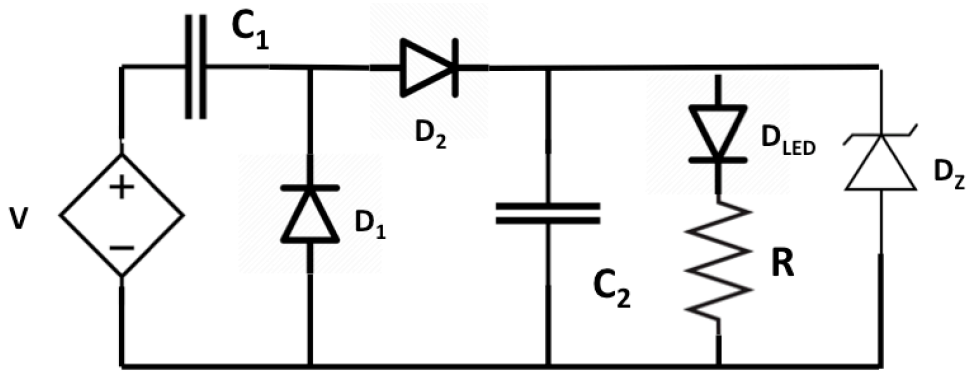

Figure 5.9: Circuit diagram of half wave voltage doubler circuit with parallel load branches consisting of the LED and voltage limiting Zener. During the negative voltage cycle, current flows through the diodes charging capacitors C_1 and C_2. During the subsequent positive cycle, charge on capacitor C_1 is boosted up to nearly $2\times V_{pk}$ and flows through diode D_2 to equilibrate voltage with C_2. With minimal loading, and over several cycles, a DC voltage of nearly $2\times V_{pk}$ (minus voltage drop over diodes) is established across capacitor C_2.

Additionally, in order to keep the output supply relatively stable, the time constant of capacitor discharge through the LED branch should greatly exceed the period of the circuit operation:

$$f^{-1} = 73\text{ nsec} \ll RC$$

$$C \gg \frac{1}{fR} = \frac{1}{(13.56\text{ [MHz]})(225\text{ k}\Omega)} = 327\text{ fF}$$

This condition is easily met given the small load imposed by the LED.

As a safety measure, a reverse-biased Zener diode can be put in parallel with the LED branch to limit the possible voltage developed in the circuit. Above V_{Zener}, breakdown causes the branch to act effectively as a short, drastically reducing the load resistance of the circuit and detuning it from resonance, thereby preventing additional power transfer.

Feasibility of Battery Power

Given the nightly energy requirements (8 hour @ 280 nW) for rod dark current suppression over the retina of 8 mJ, detailed in section "Energetics of Dark Current Suppression", it is possible to evaluate the feasibility of using a battery to power the LED. Assuming an LED luminous efficiency of 10%, this puts the LED power requirements at around 80mJ. Cymbet Corporation produces two rechargeable, solid-state, bare die batteries in their EnerChip™ series that closely meet this requirement both in terms of energy and physical size: CBC005 (72 mJ, 5 uAhr, 4 V, 1.7×2.25×0.200 mm) and CBC050 (720 mJ, 50 uAhr, 4 V, 5.7×6.1×0.200 mm). Combined with a low-power ASIC it appears feasible to battery power the contact lens from a rechargeable battery, obviating the need for continuous nightly powering.

Fabrication of Circuits and Lens

Based on the calculations in section "Design Calculations and Considerations", a single-sided circuit board layout was produced to accommodate the necessary circuit components (Figure 5.10). The boards were first produced out of FR-4 to facilitate testing and subsequently reproduced using a flexible copper on Parylene C approach to enable

integration into a contact lens. Further details of the circuit board fabrication are given in Chapter 7. Components were sourced from Digi-key (Minnesota, USA) unless otherwise noted and are summarized in Table 5.4.

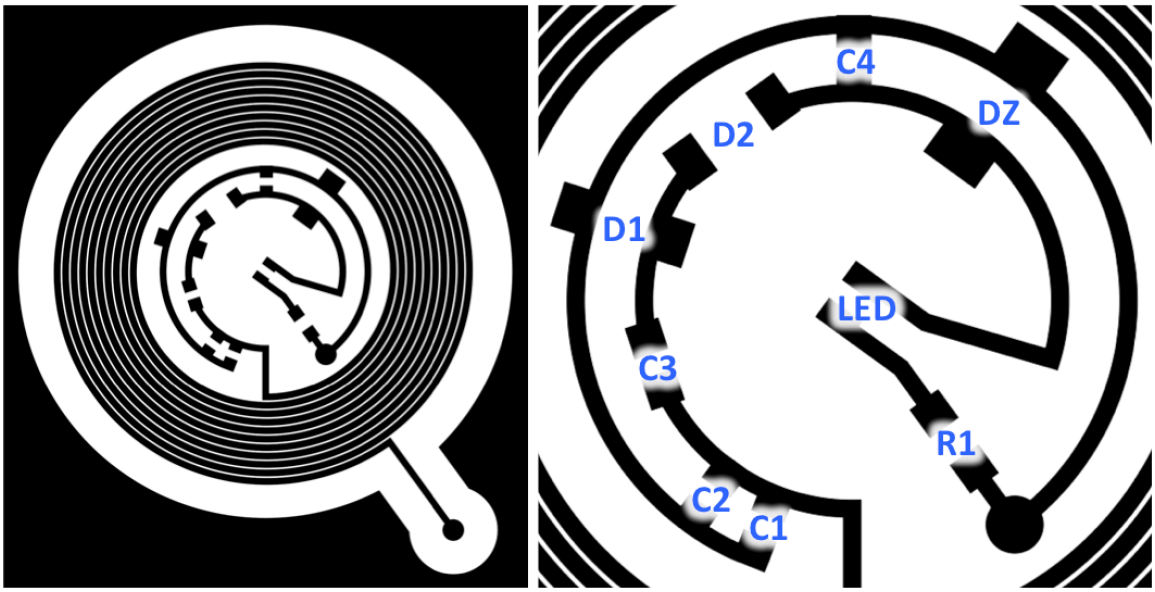

Figure 5.10: Traces for wireless LED contact lens and constituent components.

Table 5.4: Component specifications for wireless LED contact lens.

Name	Type	Value	Part #	Package	Purpose
C1	Ceramic Capacitor	100±1pF	GRM0335C1E101FA01D	0201	LC-tank primary
C2	Ceramic Capacitor	1-25 pF	Varies	0201	LC-tank tuning
C3, C4	Ceramic Capacitor	1 µF	GRM033R60J105ME11E	0201	Rectifier and Voltage Doubler
D1, D2	Schottky Diode	0.28 V @ I_F =1.0 mA	NSR0140P2T5G	SOD923	Rectifier and Voltage Doubler
DZ	Zener Diode	4.1V 200 mW	DZ9F4V1S92-7	SOD923	Voltage Regulation
LED	Green LED	518nm, 79mcd @ I_F = 5.0 mA	XZBGR155W5MAV	0201	Light Emission
R1	Resistor	20-100 kΩ 1/20 W	RC0603F104CS	0201	Current Limiting

Traces were produced by photolithographic patterning, etching, and photoresist removal. Solder paste (SMDLTLFP, Sn42 / Bi57.6 / Ag0.4, from Chipquik, NY) was applied to electrical pads and components were placed by hand under a microscope. Re-flow soldering (140 °C for 1 min, 190 °C for 30 s) was used to form electrical connections between components and the traces and carried out on a Voltera V-One PCB Printer (Voltera, ON, CA). The operation of the circuit was subsequently evaluated by application of a 13.56 MHz magnetic field, which was observed to induce LED emission.

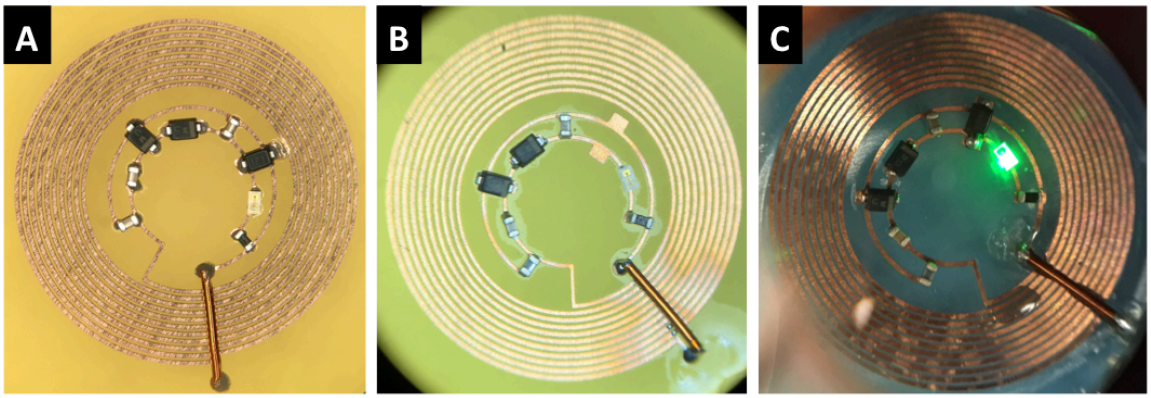

Figure 5.11: Assembly of FR-4 circuit. A) Solder paste was applied to electrical pads and components were placed by hand under a microscope. B) Re-flow soldering forms electrical connections between components and traces. C) Application of a 13.56 MHz magnetic field induces LED emission.

The properties of the circuit were further characterized by performing a frequency sweep. An Agilent 33120A Function Generator (50 Ω output impedance) was used to drive a primary coil (1.85 μH, 11 turns, 11 mm diameter, 3 mm height, 291 μm diameter wire) to produce a magnetic field. The wireless LED circuit was placed directly underneath the primary coil. The voltage and frequency of the function generator were

swept to see the relative behaviour of the wireless LED circuit, which was probed by an oscilloscope across the resonant capacitor and at the DC output (Figure 5.12).

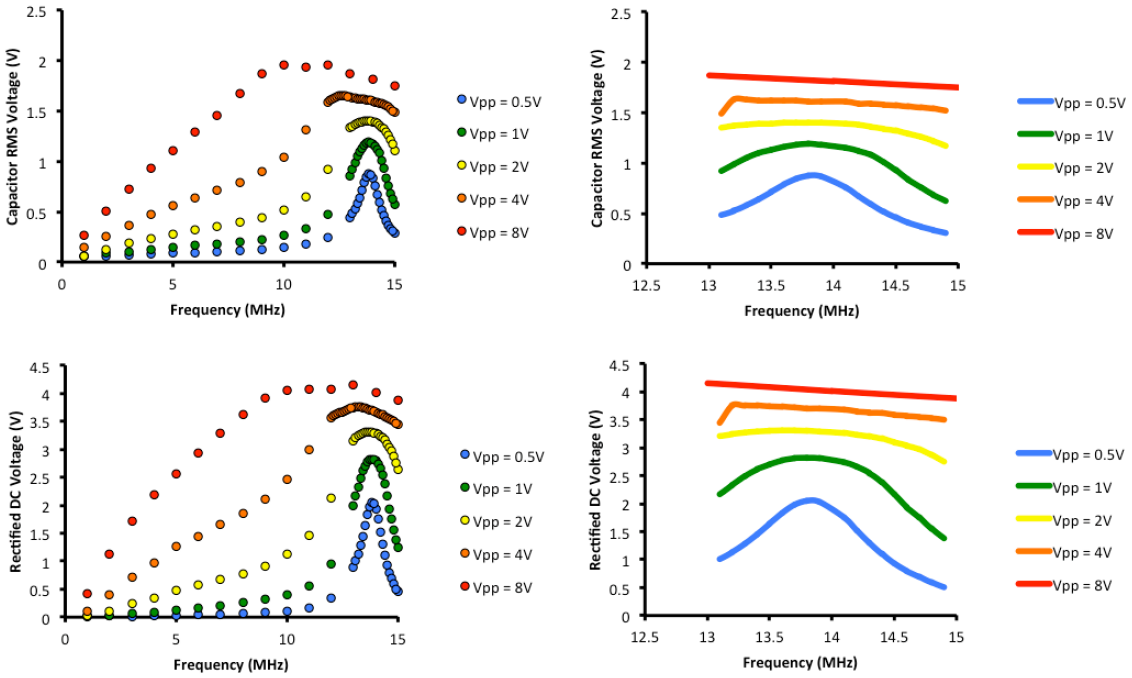

Figure 5.12: Frequency response of wireless LED circuit on FR-4 board. (Top) RMS voltage across the capacitor of the LC-tank. (Bottom) DC voltage at the circuit output available to drive the LED. Sweep of primary coil driving voltage indicated in legend. A 20 kΩ current-limiting resistor used in series with LED.

A Tektronix TBS 1064 oscilloscope was used to probe the frequency response of the circuit. This model of oscilloscope features an input impedance of 1 MΩ ±2% in parallel with 20 pF ± 3 pF and can therefore de-tune the circuit it is measuring due to the relatively small capacitance of the LC-tank (100 pF). To mitigate this, a 10× probe was used to reduce both de-tuning and loading. Loading of the LC circuit is effectively reduced by 10× to only 2 pF and thus the frequency deviation is expected to be maintained to 1%.

$$\frac{f_{Unloaded}}{f_{Loaded}} = \sqrt{\frac{C_{Loaded}}{C_{Unloaded}}} < \sqrt{\frac{102pF}{100pF}} = 1.01$$

The resonant frequency was measured to be 13.8 MHz, though accounting for the oscilloscope loading this is likely closer to 13.9 MHz. The value was deemed close enough to proceed with flexible circuit fabrication as slight variances due to curved coil geometry were anticipated to modify coil inductance and therefore shift the resonant frequency anyways.

The half wave voltage doubling circuit is shown to also function as intended, providing a rectified DC output of approximately double the tank RMS voltage. The effect of the reverse-biased Zener diode is observed once the rectified DC voltage approaches 4.1 V and results in a widening of the frequency response. It also effectively functions to limit the maximum rectified voltage.

Utilizing a copper-on-Parylene process, detailed in Chapter 7, flexible wireless LED circuits were produced suitable for integration into a curved geometry contact lens. Using photolithography, the copper-on-Parylene substrate (25.4 μm copper on 2.5 μm Parylene C) was patterned and etched to produce the desired traces. The trace geometry was modified slightly to position the LED within the center of the lens in order to ensure that light was transmitted through the pupil, despite constriction. The consequences of this are subsequently discussed in more detail. The circuit was then cut out and the jump wire was wrapped with Parylene to insulate it before being bent over and soldered to complete the loop. The circuit was then molded to a 20 mm diameter spherical cap in order to fit the geometry of the contact lens. Electrical components were soldered to the circuit via re-flow and the circuit resonance was measured and tuned by adding additional

capacitors as necessary to reach 13.56 MHz. The completed circuit was then encapsulated in silicone (Sylgaurd 184, Dow Chemical) via a 20 mm diameter mold.

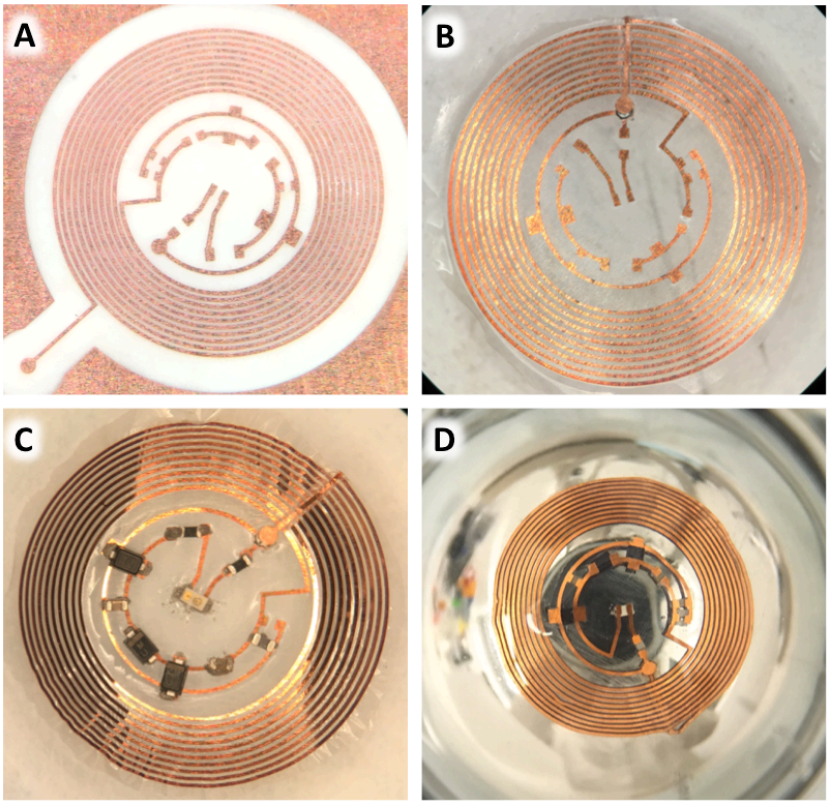

Figure 5.13: Fabrication of flexible copper on Parylene wireless LED circuit and integration into contact lens. (A) Copper traces etched from copper on 2.5 µm Parylene C substrate. (B) Copper trace is cut out, jump wire is soldered to complete loop, and the circuit is molded to a 20 mm diameter spherical cap. (C) Electrical components are soldered to the circuit via re-flow. (D) The completed circuit is encapsulated in a silicone contact lens.

The tuning of the contact lens was carried out using a similar setup to the FR-4 board, featuring a primary coil driven by a signal generator. The resonant frequency was measured by sweeping the field frequency and monitoring the LED light output. This

avoided concerns with oscilloscope loading. The peak frequency response of the complete circuit was measured to be 14.1 MHz with the 100 pF capacitor. This is slightly higher than the 13.9 MHz for the FR-4 circuit as expected due to the reduced inductance of the coil as a result of shaping it to a spherical curvature. The necessary capacitor value to achieve 13.56 MHz is calculated as:

$$C_{tuned} = \frac{(f_{measured})^2}{(f_{desired})^2} C_{initial} = \frac{(14.43\ MHz)^2}{(13.56\ MHz)^2} 100\ pF = 113\ pF$$

Therefore, additional capacitance of 12.5 pF (closest achievable with available components) was added to the circuit, shifting the resonant frequency to 13.6 MHz. The circuit was then encapsulated in silicone as described. Operation of the contact lens was demonstrated using a 13.56 MHz RFID reader (Figure 5.14).

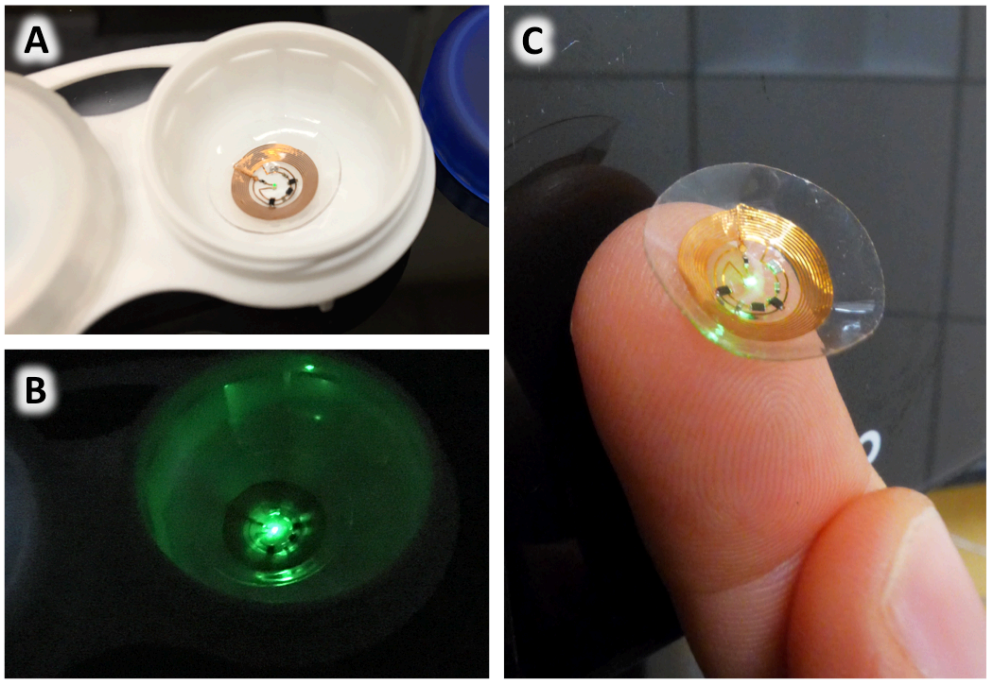

Figure 5.14: Completed wireless LED contact lens (A) under illumination and (B) in the dark. (C) Lens on finger for scale.

CHAPTER 6 – Permeability of Contact Lenses

Key Take-Aways
• Lens oxygen transmissivity is critical for corneal health. • Cavity-style lenses with high permeability filler allow for encapsulation of active components while maintaining high oxygen transmissivity. • Shelling impermeable components in highly permeable material allows oxygen to shunt around them, preventing localized corneal hypoxia.

Historical and Future Perspectives on Gas Permeable Lenses

As we have learned from the historical development of contact lenses a major impediment to their adoption has been comfort and safety. In these regards, the importance of oxygen delivery to the cornea cannot be overstated. While today's lens materials (rigid gas permeable and silicone hydrogel) have overcome the problem of oxygen delivery in conventional lenses, next generation "smart lens" concepts will introduce new challenges. Most active components are based on silicon and metal, both gas impermeable materials, and so embedding them into lenses poses a challenge with respect to oxygen delivery. This chapter will explore the importance of oxygen transport to the cornea through the contact lens and methods of incorporating active components into the lens while maintaining sufficient oxygen delivery.

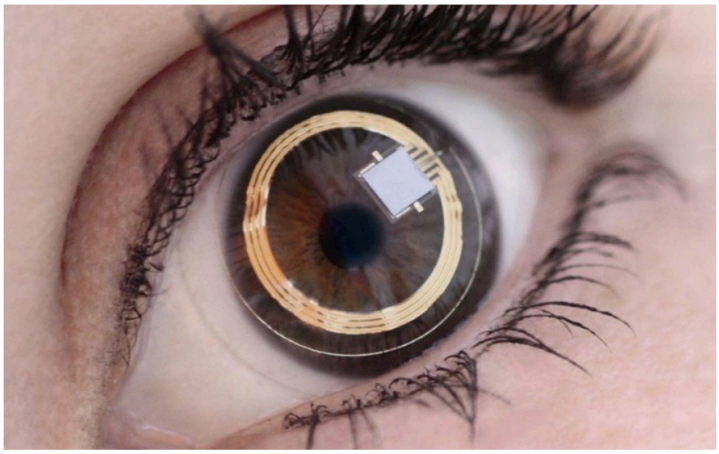

Figure 6.1: Samsung's smart lens for augmented reality features a large oxygen impermeable chip [160].

Corneal Anatomy

The cornea is the clear, central, fibrous tissue on which the contact lens sits. Consideration of key anatomical features of the cornea is important for safe contact lens design. Significantly, the cornea is avascular receiving much of its oxygen supply from atmospheric gas exchange through the tear film and relying on diffusion through its 500μm thickness. The cornea is composed of 3 primary layers (and 2 interfacial boundary layers), from anterior to posterior: epithelium, (Bowman's layer), stroma, (Descemet's layer), and endothelium [18]. The epithelium is a non-keratinized, stratified squamous layer of 5-6 cells undergoing constant shedding/replacement to act as a permeability barrier to water and infection, and presenting an extensive glycocalyx to interact with the tear film. The stroma is composed of intricately arranged layers of collagen for optical clarity that is maintained by dispersed keratocytes (3-5% by volume) and provides the mechanical integrity of the cornea. The endothelium is a single layer of squamous cells important in the maintenance of corneal transparency and is located on the posterior side of the stroma.

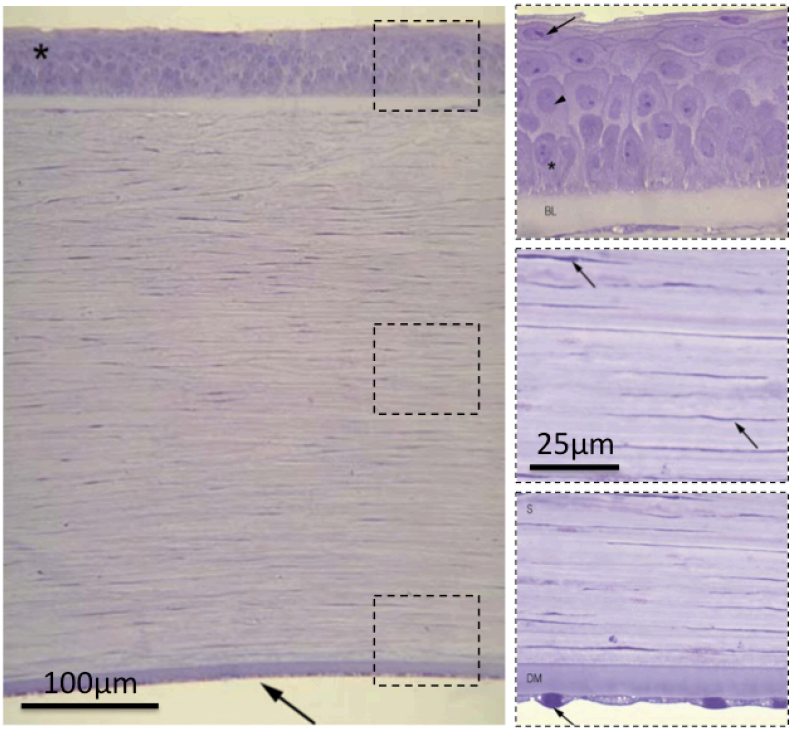

Figure 6.2: Corneal cross-section with zoom-ins of epithelium (top), stroma (mid), and endothelium (bottom). Reprinted from [18].

From a metabolic perspective, oxidative metabolism of glucose is the primary source of energy for the cornea [161]. While 85% of glucose is consumed through anaerobic glycolysis, only 2 ATP molecules are produced (along with 2 lactate molecules) compared to the 36 ATP from the Kreb cycle. Thus energy is produced roughly in a ratio of 1 anaerobic : 3 aerobic. Under normal conditions, the excess lactate diffuses across the endothelium into the anterior chamber. However, under hypoxic conditions significantly more lactate must be produced to maintain energy demands and this increases the tonicity of the fluid, leading to swelling [162]. Total oxygen flux into the cornea under normal conditions measures 6 $\mu L/hr/cm^2$ and is distributed 40% epithelial, 39% stromal, 21% endothelial [163]. The aqueous humor, while the primary source of nutrients to the cornea, is only moderately oxygenated at roughly 55mmHg

(range of 24-72mmHg reported) [164]. Thus most corneal oxygen is derived from the atmosphere or palpebral vasculature. During sleep the tear film is in equilibrium with the palpebral vasculature (55 mmHg) and while eyes are open with atmosphere (155 mmHg).

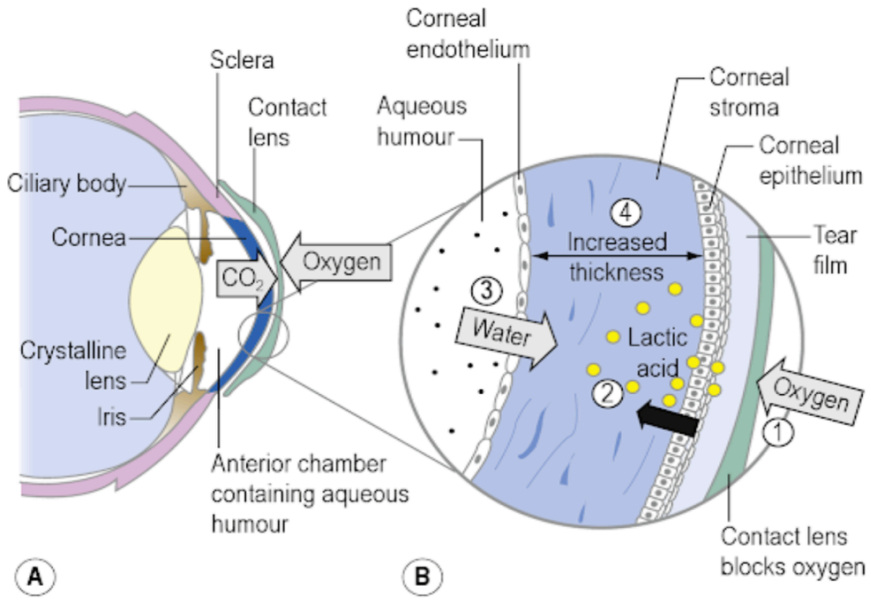

Figure 6.3: Contact lenses can induce corneal hypoxia by retarding oxygen transport from the atmosphere. Lactic acid produced under anaerobic metabolism draws water into the tissue contributing to corneal swelling. Reprinted from [18].

Target Permeability to Mitigate Corneal Swelling

The introduction of a contact lens over the cornea reduces the diffusional transport of oxygen from the atmosphere/eyelid to the anterior corneal tissue, which can result in hypoxia and swelling. Even when a patient sleeps without contact lenses the reduced oxygen available under the closed eyelid (palpebral conjunctiva: 55 mmHg) versus open eyelid (atmosphere: 155 mmHg) [165] results in central corneal swelling of around 4% [166]–[169]. This provides a physiological baseline from which to compare contact lenses of varying degrees of oxygen permeability.

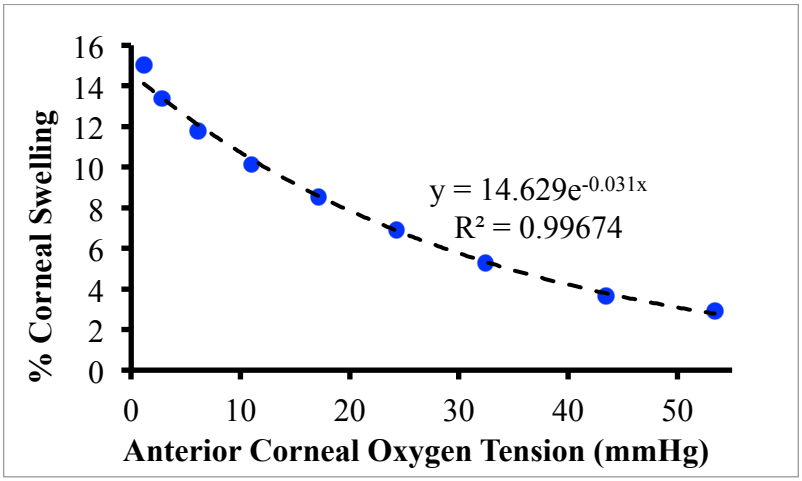

Figure 6.4: Effect of hypoxia on corneal swelling in an eye adapted to overnight contact lens wear. Adapted from [18].

The most commonly used metric to compare contact lenses is the oxygen transmissibility Dk/t, where D is the diffusion coefficient of oxygen in the contact lens, k is the solubility of oxygen in the contact lens, and t is the thickness of the contact lens. This comes from the solution of Fick's Law (in combination with Henry's Law) when applied to a slab of permeable material with a pressure gradient across it. Consider a slab of thickness t, with a solubility k and diffusivity D for a given gas in the slab material, that has a partial pressure difference of ΔP across it. Henry's law of gas solubility states:

$$C = k \cdot P$$

The concentration of gas at the interfaces of the material are then:

$$C(0) = k \cdot P(0)$$

$$C(t) = k \cdot P(t)$$

By conservation of mass, the flux of gas through the slab must be constant. Fick's law of diffusion states:

$$J = -D\frac{dC}{dx}$$

This can be integrated and solved using boundary condition from Henry's Law to give:

$$C(x) = C(0) - \frac{Jx}{D}$$

$$C(0) - C(t) = k \cdot \Delta P = \frac{Jt}{D}$$

$$J = \frac{Dk}{t} \cdot \Delta P$$

Higher transmissibility means the lens imposes a lower barrier to oxygen diffusion and therefore has less effect on the oxygenation of the cornea. The utility of this metric can be appreciated by analogy to electrical circuits in Table 6.1.

Table 6.1: Electrical analogies of gas diffusive transport.

Parameter	Oxygen System	Electrical System
Potential	ΔP, Partial Pressure	ΔV, Voltage
Sheet Conductance	Dk/t, D is the diffusion coefficient of oxygen in the contact lens, k is the solubility of oxygen in the contact lens, and t is the thickness of the contact lens	G/A = σ/L, where L is the length of the conductor, A is the cross-sectional area of the conductor, σ is the electrical conductivity, G is the conductance
Flux/Current density	J, the molar flux of oxygen	J = I/A, where I is the current, A is the cross-sectional area of the conductor, J is the current density
Ohm's Law	J = (Dk/t)•ΔP	J = (σ/L)• ΔV

Since diffusional oxygen transport has an analogous form to Ohm's law, the treatment and interpretation of transmissibility is straightforward. As a first approximation, the contact lens can be considered as an additional diffusional resistance in series with the corneal tissue resistance to oxygen (R_{cornea}):

$$R_{total} = \frac{R_{cornea} \cdot (Dk/t)^{-1}}{R_{cornea} + (Dk/t)^{-1}}$$

In the case that $(Dk/t)^{-1} >> R_{cornea}$, oxygen flux is limited by the lens; in the case that $(Dk/t)^{-1} << R_{cornea}$, oxygen flux is limited by the tissue. Historically, Dk/t was used as a

metric for comparison of lenses because early lenses operated in the lens-limiting regime and hence a lens of 20 Fatt would be twice as good as a lens of 10 Fatt; however, as lens transmissibility has improved, the regime is closer to cornea-limiting and hence a 200 Fatt lens is not twice as good as a 100 Fatt lens [170]. With respect to corneal hypoxia, higher transmissibility lenses are superior but the therapeutic benefit diminishes as the lens transmissibility exceeds that of the corneal tissue.

The transmissibility at which corneal swelling is kept within acceptable ranges (4%, *i.e.* same levels as without lens under closed eye conditions) was determined to be 87 Barrer/cm [166] and little to no additional benefit has been demonstrated for lenses beyond this transmissibility. For prevention of anoxia throughout the entire corneal thickness under closed eye conditions, a slightly higher transmissibility of 125 Barrer/cm is needed [171]. Another concept commonly used in the discussion of contact lens transmissibility is the equivalent oxygen percentage (EOP), which is the resulting oxygen level at the anterior surface of the cornea when a lens is worn. For a completely permeable lens, an EOP of 20.9% is expected in an open eye [166], [172]; empirically, $EOP\ (\%) = 6.195 \ln (Dk/L \times 10^9) - 9.778$. Figure 6.5 plots the relationship between EOP and Dk/L.

The consequences of corneal swelling depend on the degree and duration of hypoxia. In the acute situation, visible striations and folds begin to form on the cornea at 4-6% corneal swelling; at around 13% corneal swelling visual disturbances occur. The recommended limit for swelling has been proposed as 8%, which allows for rapid deswelling of the open eye following sleep [166]. In the chronic situation, hypoxia induced by overnight contact wear causes a number of physiological changes, including:

epithelial microcysts, corneal neovascularization, endothelial polymegethism (higher than normal variation in cell size), slowed epithelial healing, increased bacterial binding and corneal infection, among others.

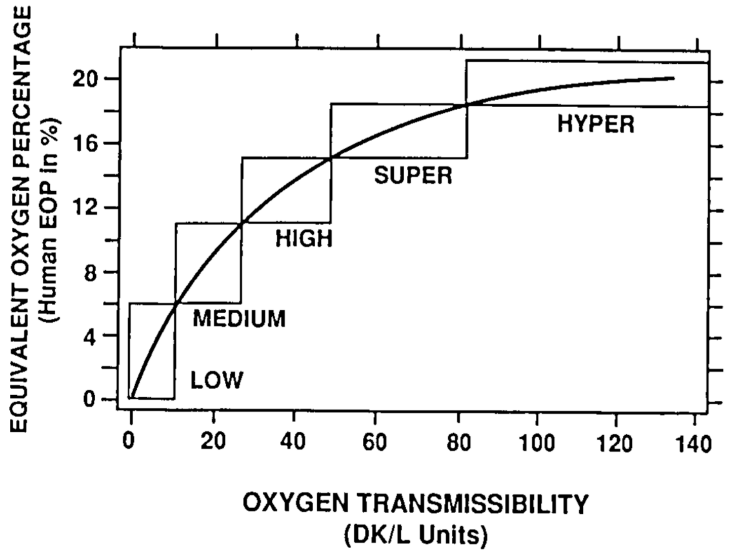

Figure 6.5: EOP versus transmissibility of contact lenses. Reprinted from [173].

Gas Permeable Materials for Contact Lenses

In the 1960's, the importance of oxygen transmissibility in contact lenses became appreciated and efforts to develop replacement materials for PMMA took off. Silicone rubbers were identified as one candidate due to their higher oxygen permeability, in excess of 1000× that of PMMA. Unfortunately, the hydrophobicity and elasticity of the polymer causes it to stretch and de-wet the tear film during blinking, leading to binding of the lens to the cornea. Methods of surface treatment such as oxygen plasma and grafting to render the lenses hydrophilic are temporary due to the tendency of the highly mobile chains to reorient.

Another class of materials known as rigid gas permeable polymers was developed by successive modification of PMMA to improve oxygen permeability. While the specific composition of RGP lenses vary, they are generally composed of tris(trimethyl-siloxy)-methacryloxy-propylsilane (TRIS), a fluoroalkyl methacrylate, and methyl methacrylate. The hydrophilic co-monomers imbue hydrophobicity to the polymer while the siloxy and fluoralkyl methacrylates improve oxygen permeability. The resulting material is quite stiff but achieves oxygen permeability on the order of 100× PMMA, while maintaining superior wettability compared to silicone rubbers.

Permeability of PDMS and Rigid Gas Permeable Materials

The permeability of clinically relevant RGP and silicone rubbers are indicated in Table 6.2 with comparisons made to air and water.

Table 6.2: Permeability of common contact lens materials.

Polymer System	Permeability (Dk)	Comment
HDS 100	100	[174]
MED4-4210	~650	Measured
Menicon Z	163	[175]
Water	99	[165]
Air	25000000	[176]

Conventionally, permeability Dk is given in units of Barrer, where:

$$1\ \text{barrer} = 10^{-10}\ \frac{\text{cm}^3_{\text{STP}} \cdot \text{cm}}{\text{cm}^2 \cdot \text{s} \cdot \text{cmHg}}$$

Transmissibility Dk/t is given in units of Fatt, where:

$$1\ \text{fatt} = 10^2 \frac{\text{barrer}}{\text{cm}} = \frac{1\ \text{barrer}}{100\mu\text{m}} = 10^{-8}\ \frac{\text{cm}^3_{\text{STP}}}{\text{cm}^2 \cdot \text{s} \cdot \text{cmHg}}$$

Measurement of Silicone Dk/t

To measure the permeability of silicone, MED4-4210 PDMS was cast into a uniform 120 μm film and placed in a custom apparatus that measures the oxygen permeability of membranes. The membrane seals a small compartment of known volume and cross-section that contains an oxygen probe. Oxygen gas is blown over the exterior surface of the membrane while the interior oxygen concentration of the compartment is monitored. From the resulting plot, the permeability of the MED-4210 membrane was computed to be 650 Barrer.

Design of Gas Permeability Apparatus

Assume a well-mixed volume of gas (V) surrounded by impermeable walls/bottom and covered with a permeable membrane of given thickness (L) and surface area (A). From the ideal gas law:

$$PV = NRT$$

Differentiating with respect to time:

$$\frac{dP}{dt}V = \frac{dN}{dt}RT$$

From membrane permeation theory and conservation of mass:

$$\frac{dN}{dt} = -J \cdot A = -\left(-D \cdot \frac{k \cdot (P_{ext} - P)}{L}\right) \cdot A = -\left(\frac{Dk}{L}\right) \cdot (P - P_{ext}) \cdot A$$

Combining equations:

$$\frac{dP}{dt}V = -\left(\frac{Dk}{L}\right) \cdot (P - P_{ext}) \cdot A \cdot RT$$

$$\frac{dP}{dt}V = -\left(\frac{Dk}{L}\right) \cdot (P - P_{ext}) \cdot A \cdot RT$$

Solving the differential equation:

$$P(t) = (P_i - P_f) \cdot e^{\frac{-t}{\left(\frac{LV}{DkART}\right)}} + P_f, \text{ where } \tau_{permeation} = \frac{V}{\left(\frac{Dk}{L}\right)ART}$$

Verifying well-mixed condition for a membrane of permeability Dk:

$$\tau_{mix} = \frac{L_{reservoir}^2}{D_{O_2:Air}} \ll \tau_{permeation}$$

$$\frac{(3.2mm)^2}{17.6\frac{mm^2}{s}} = 0.58s \ll \frac{543mm^3}{\frac{Dk\,[barrer]}{0.12mm} \cdot 184mm^2 \cdot \left(\frac{2476J}{mol}\right)} = \frac{426886\ s}{Dk\,[barrer]}$$

$$Dk \ll 736000 \text{ barrers}$$

Thus the setup is appropriate for characterizing virtually all known materials.

An embedded needle-type, fluorescence-based oxygen probe (FOXY-AL300 from Ocean Optics, FL; refurbished by White Bear Photonics, MN) recorded oxygen concentration (Reader Model NEOFOXGT-NFG0739 from Ocean Optics, FL) within the apparatus volume during a step from atmosphere to nitrogen gas blowing over the exterior surface of the tested membrane. The resulting data was fit with an exponential equation in MATLAB using the *nlinfit* function of the form:

$$f(t) = a \cdot e^{b \cdot t} + c$$

For calculation/conversion to permeability, the following formula is used:

$$Dk\,[Barrer] = \frac{b\,[s^{-1}] \cdot V\,[cm^3] \cdot L\,[cm]}{A\,[cm^2]} \cdot \left(\frac{1}{R[cm^3 \cdot atm \cdot mol^{-1}] \cdot T[K]}\right) \cdot \left(22400\left[\frac{cm_{STP}^3}{mol}\right] \cdot \frac{1}{76}\left[\frac{atm}{cmHg}\right]\right) \cdot 10^{10}$$

$$Dk\,[Barrer] = \frac{b\,[s^{-1}] \cdot V\,[cm^3] \cdot L\,[cm]}{A\,[cm^2]} \cdot \left(\frac{1}{82\,[cm^3 \cdot atm \cdot mol^{-1} \cdot K^{-1}] \cdot 293[K]}\right) \cdot \left(22400\left[\frac{cm_{STP}^3}{mol}\right] \cdot \frac{1}{76}\left[\frac{atm}{cmHg}\right]\right) \cdot 10^{10}$$

$$\mathrm{Dk\ [Barrer]} = \frac{\mathrm{b\ [s^{-1}] \cdot V\ [cm^3] \cdot L\ [cm]}}{\mathrm{A\ [cm^2]}} \cdot \left(1.23 \cdot 10^8 \left[\frac{\mathrm{cm^3_{STP}}}{\mathrm{cmHg \cdot cm^3}}\right]\right)$$

For calculation/conversion to transmissibility, the following formula is used:

$$\frac{\mathrm{Dk}}{\mathrm{L}}\mathrm{[Fatt]} = \frac{\mathrm{b\ [s^{-1}] \cdot V\ [cm^3]}}{\mathrm{A\ [cm^2]}} \cdot \left(\frac{1}{\mathrm{R[cm^3 \cdot atm \cdot mol^{-1}] \cdot T[K]}}\right) \cdot \left(22400 \left[\frac{\mathrm{cm^3_{STP}}}{\mathrm{mol}}\right] \cdot \frac{1}{76}\left[\frac{\mathrm{atm}}{\mathrm{cmHg}}\right]\right) \cdot 10^8$$

$$\frac{\mathrm{Dk}}{\mathrm{L}}\mathrm{[Fatt]} = \frac{\mathrm{b\ [s^{-1}] \cdot V\ [cm^3]}}{\mathrm{A\ [cm^2]}} \cdot \left(\frac{1}{\mathrm{82\ [cm^3 \cdot atm \cdot mol^{-1} \cdot K^{-1}] \cdot 293[K]}}\right) \cdot \left(22400 \left[\frac{\mathrm{cm^3_{STP}}}{\mathrm{mol}}\right] \cdot \frac{1}{76}\left[\frac{\mathrm{atm}}{\mathrm{cmHg}}\right]\right) \cdot 10^8$$

$$\frac{\mathrm{Dk}}{\mathrm{L}}\mathrm{[Fatt]} = \frac{\mathrm{b\ [s^{-1}] \cdot V\ [cm^3]}}{\mathrm{A\ [cm^2]}} \cdot \left(1.23 \cdot 10^6 \left[\frac{\mathrm{cm^3_{STP}}}{\mathrm{cmHg \cdot cm^3}}\right]\right)$$

Table 6.3: Measurement and calculation of silicone oxygen transport properties

Sample	|b|	Area	Volume	Thickness	Dk/L [Fatt]	Dk [Barrer]
PDMS	0.00152	1.84cm^2	0.543cm^3	0.012cm	550	662

Cavity-Style Design for Smart Lenses

Smart lenses look to integrate functionality beyond vision correction into the contact lens. However, most active components (*e.g.* sensors, LEDs, microchips) are based on silicon and metal, both gas impermeable materials, and so embedding them into lenses poses a challenge with respect to oxygen delivery. What is needed is a contact lens platform that enables easy encapsulation of active components without affecting the oxygen transmission of the overall lens.

In this work, a cavity style lens is developed that may act as such a platform. By bonding two lenses with slightly different curvatures together along their peripheral

edges, one can produce an internal cavity to house active components. The cavity may be filled with a highly-gas permeable filler material for structural reasons or to prevent accumulation of fluid. Two filler materials are considered in this work: PDMS, well known for its high oxygen permeability and hydrophobized Vycor, a new material developed in the MEMS lab with exceptional gas transport properties. This novel lens geometry and corresponding design considerations are outlined in the following section. In particular, the mechanism by which the composite lens overcomes oxygen transmissibility concerns is developed.

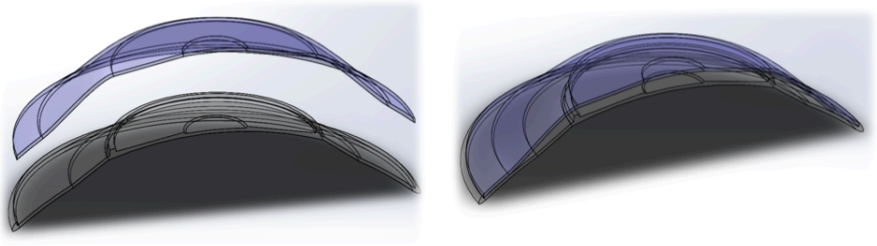

Figure 6.6: Cavity style contact lens formed by bonding two lenses of different curvature along a complimentary peripheral edge.

Simulations of Cavity-Style Lens Gas Transmissibility

To understand the design space, a 3D COMSOL model was made of such a composite contact lens with an inner 400 μm cavity, housing 24 GTLS (300 μm D x 2 mm) as a relevant example. Top and bottom lens thicknesses, RGP material, and cavity filler material (*e.g.* air, hydrophobized Vycor, or PDMS) were varied and the resultant transmissibility of the lens were measured. Figure 6.7 depicts this geometry (note: corneal tissue was excluded from this modeling). The results are summarized in Table 6.4 and are color-coded according to hyper, super, high, or medium gas transmissibility based on the standards set by [173].

Table 6.4: Transmissibility of cavity style lens of various lens thickness and filler material. Hyper (green), Super (yellow), High (orange), and Medium (Red) transmissivity indicated.

Lens Thickness [µm]	RGP Material Dk [Barrer]	Cavity Filler Material	Transmissibility Dk/t [Fatt]
50	163	Air	161
50	163	Vycor	155
50	100	Air	99
50	100	Vycor	97
50	163	PDMS	83
100	163	Air	81
100	163	Vycor	80
50	100	PDMS	63
100	163	PDMS	55
150	163	Air	54
150	163	Vycor	53
100	100	Air	50
100	100	Vycor	49
150	163	PDMS	41
100	100	PDMS	38
150	100	Air	33
150	100	Vycor	33
150	100	PDMS	28

The analysis demonstrates that it is possible to design high transmissibility contact lenses suitable for overnight wear by utilizing a cavity-style design. Oxygen is able to shunt around the gas impermeable components within the lens, thereby mitigating their effect. For comparison, a similarly sized lens of solid Menicon Z would have an oxygen transmissibility of less than 33 Fatt, unsuitable for overnight use.

Experimental Validation of Cavity-Style Lens Approach

Using the RGP lenses from Chapter 4 and a similar setup and approach to section "Measurement of Silicone Dk/t", the transmissibility of cavity style lens prototypes was carried out. The transmissibility of the top lens, bottom lens, an empty paired set of lenses, and a paired set of lenses containing a GTLS lighting system was measured and the results are summarized in Table 6.5.

Table 6.5: Oxygen transmissibility of cavity-style contact lenses and related components. (*) Accounting for effect of setup on paired lenses.

Sample	|b| [s^{-1}]	Area [cm^2]	Volume [cm^3]	Thickness [cm]	Dk/L [Fatt]
Top Lens	0.0005618	0.341	0.0299	0.018	60
Bottom Lens	0.000721	0.328	0.036	0.018	97
Empty Pair	0.0004089	0.341	0.0299	0.096	44, 37*
GTLS Pair	0.000282	0.341	0.0299	0.096	30, 26*
PDMS	0.00470 0.00776	0.316	0.0534	0.012	975 1610
PDMS + diX-A	0.000607 0.000635	0.316	0.0534	0.012	126 132

Briefly, the lens sat on top of an o-ring and was gently compressed against an acrylic plate, with a small hole for the oxygen probe, to form a sealed gas test volume. Oxygen was blown over the outside of the lens and the change in the interior oxygen concentration was measured. The volume of the gas compartment was measured by filling it with water and measuring the mass change of the system to account for slight variations in geometry due to different lens curvatures. The area of the lens interfacing with the gas compartment was calculated from the known diameter of the o-ring seal and the base curvature of the contact lens, which enable the spherical cap area to be

calculated. Oxygen profiles were fit with an exponential function and the rate constant *b* was extracted and used to calculate transmissibility based on the known geometry of the setup.

In the setup, due to the hollow cavity the entire bottom lens is exposed to oxygen, while only the indicated area of the top lens interfaces with the test volume. Consequently, the transmissibility of the lens is measured higher than reality. This is accurately predicted by scaling the transmissibility of the bottom lens by its relative exposed surface area compared to the top lens and then calculating the series transmissibility:

$$\left(\frac{\mathrm{Dk}}{\mathrm{t}}\right)_{\mathrm{predicted}} = \left(\frac{1}{\frac{\mathrm{A_{bottom}}}{\mathrm{A_{top}}}\left(\frac{\mathrm{Dk}}{\mathrm{t}}\right)_{\mathrm{bottom}}} + \frac{1}{\left(\frac{\mathrm{Dk}}{\mathrm{t}}\right)_{\mathrm{top}}}\right)^{-1} = \left(\frac{1}{\frac{0.562}{0.341}\cdot 97} + \frac{1}{60}\right)^{-1} = 44$$

This is in agreement with what is measured by the setup. In reality, the series transmissibility of the paired lenses should be:

$$\left(\frac{\mathrm{Dk}}{\mathrm{t}}\right)_{\mathrm{theoretical}} = \left(\frac{1}{\left(\frac{\mathrm{Dk}}{\mathrm{t}}\right)_{\mathrm{bottom}}} + \frac{1}{\left(\frac{\mathrm{Dk}}{\mathrm{t}}\right)_{\mathrm{top}}}\right)^{-1} = \left(\frac{1}{97} + \frac{1}{60}\right)^{-1} = 37$$

The measured values can then be corrected by scaling accordingly:

$$\left(\frac{\mathrm{Dk}}{\mathrm{t}}\right)_{\mathrm{corrected,GTLS}} = \frac{\left(\frac{\mathrm{Dk}}{\mathrm{t}}\right)_{\mathrm{theoretical,empty}}}{\left(\frac{\mathrm{Dk}}{\mathrm{t}}\right)_{\mathrm{measured,empty}}} \cdot \left(\frac{\mathrm{Dk}}{\mathrm{t}}\right)_{\mathrm{measured,GTLS}} = \frac{37}{44}\cdot 30 = 26$$

Corrected values are indicated by (*) in Table 6.5.

Note that the lenses used in this experiment have a central thickness of 180 μm, which is quite thick, compared to what is technically achievable, and thus the absolute transmissibilities measured are relatively low compared to overnight wear lenses.

However, the relative performance of the cavity style lens concept can still be evaluated with the understanding from earlier simulations in Table 6.4 that transmissibility will scale nearly linearly with lens thickness.

The cavity-style lens filled with a GTLS lighting system is observed to have a transmissibility within 70% of the empty cavity-style lens, despite it containing gas impermeable components occupying >99% of the lens area over which transmissibility was measured. This result demonstrates that oxygen is able to transport around the impermeable components within the lens cavity, thereby mitigating their impact on overall lens transmissibility.

Modeling Oxygen Profiles in Cornea

As a metric, transmissibility is useful in its simplicity. However, what ultimately matters is the oxygenation of the underlying corneal tissue. As lens geometries become more complex, including the encapsulation of impermeable components, it is important to have a more detailed picture of oxygen transport.

To this end, the 3D COMSOL model of the phototherapy contact lens was extended to include a corneal layer composed of epithelium, stroma, and endothelium (Figure 6.7). Standard Michaelis-Menten kinetics for oxygen consumption are utilized with tissue parameters collected from literature and summarized in Table 6.6.

Table 6.6: Parameters of oxygen transport in the cornea. (*) Indicates primary source in cases where references are daisy-chained. Where multiple independent sources were found for a given parameter, the one used in the simulations is indicated in bold. Note, Dk for corneal tissue is decomposed using $k_{O2,water}$.

Parameter	Value [unit]	Reference	Comment
$Dk_{O2,endothelium}$	5.3 [barrer]	[170], [177]*	
$Dk_{O2,stroma}$	29.5 [barrer]	[170], [177]*	
$Dk_{O2,epithelium}$	18.8 [barrer]	[170], [177]*	
$Dk_{O2,tear}$	78 [barrer]	[170]	
$Dk_{O2,water}$	99 [barrer]	[165]	
$Dk_{O2,cornea}$	86 [barrer]	[165]	
Dk_{HDS100}	100 [barrer]	[174]	
$Dk_{MeniconZ}$	163 [barrer]	[175]	
$k_{O2,water}$	**1.12 [mol/m^3/atm]**	[165]	
$k_{O2,water}$	1.09 [mol/m^3/atm]	[178]	
$D_{O2,PDMS}$	3.4E-9 [m^2/s]	[179]	
$k_{O2,PDMS}$	8 [mol/m^3/atm]	[179]	
$D_{O2,Vycor}$	7.36E-8 [m^2/s]	Measured	
$k_{O2,Vycor}$	9.22 [mol/m^3/atm]	[180]	
$D_{O2,Air}$	2.2E-5 [m^2/s]	[181],[182]	
$k_{O2,Air}$	8 [mol/m^3/atm]	Ideal Gas Law	
$L_{tear\ film}$	3 [μm]	[170]	
$L_{tear\ film}$	150 to 350 [μm]	[165]	
$L_{epithelium}$	**50 [μm]**	[170], [165]	
$L_{epithelium}$	40 [μm]	[163]	Rabbit
L_{stroma}	**480 [μm]**	[170], [165]	
L_{stroma}	359 [μm]	[163]	Rabbit
$L_{endothelium}$	1.5 [μm]	[170], [165]	
$L_{endothelium}$	4 [μm]	[163]	Rabbit
$L_{endothelium}$	**5** [μm]	[183]	Human
$P_{open\ eye}$	155 [mmHg]	[170], [165]	
$P_{closed\ eye}$	61.5 [mmHg]	[170], [165], [184]*	
$P_{aqueous\ humor}$	24 [mmHg]	[170], [165]	
$P_{aqueous\ humor}$	55 mean, 24-72 [mmHg]	[164], [185]*	
$Q_{O2,\ endothelium}$	-2.13E-2 [mol/m^3/s]	[170], [171]	
$Q_{O2,\ endothelium}$	**-6.29E-2 [mol/m^3/s]**	[163]	**Rabbit**
$Q_{O2,\ stroma}$	-1.02E-3 [mol/m^3/s]	[170], [171], [163]*	
$Q_{O2,\ epithelium}$	-1.16E-2 [mol/m^3/s]	[170], [171], [163]*	
$Q_{O2,\ corneal}$	-4.69E-3 [mol/m^3/s]	[165]	
$Q_{O2,\ corneal}$	-2.57E-3 [mol/m^3/s]	[186]	
$Q_{O2,\ corneal}$	-2.68E-3 [mol/m^3/s]	[187]	
$T_{cornea,\ eye\ open,\ 25°C}$	32 [°C]	[188]	
$T_{cornea,\ eye\ closed,\ 25°C}$	34 [°C]	[188]	
K_m	**20 [mmHg]**	[189]	

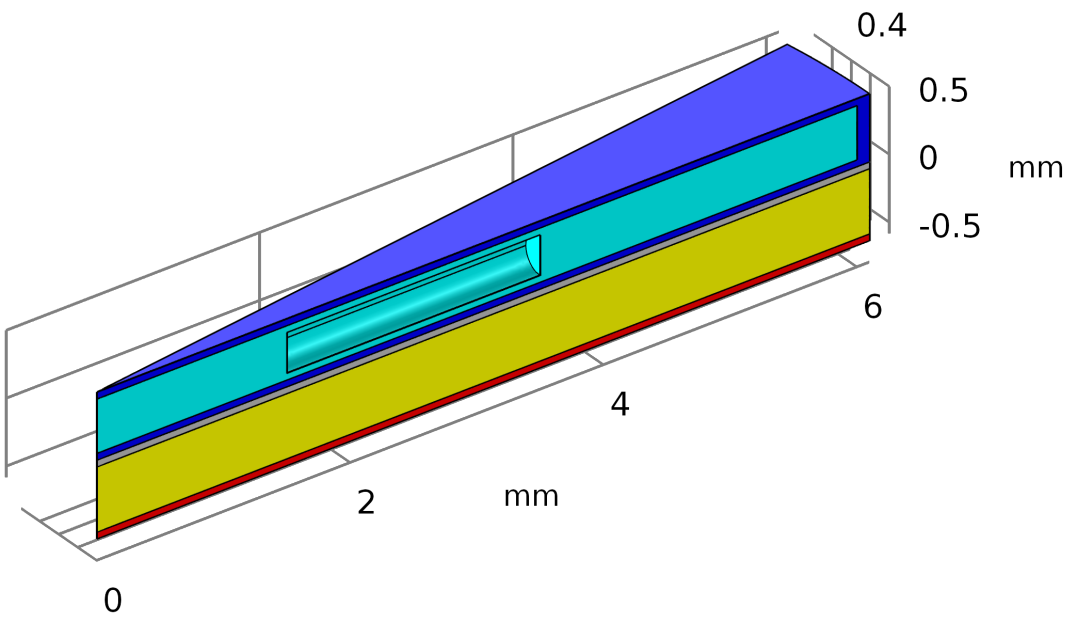

Figure 6.7: Model of composite contact lens on top of cornea used for simulations. Lens consists of an upper and lower lens of RGP (blue), filler material within the lens cavity (cyan), and GTLS (clear cylinder). Cornea consists of epithelium (grey), stroma (yellow), and endothelium (red, note: 10× thickness for visualization). Symmetry conditions on front and back face of model are applied to simplify computation.

The model allows for investigation of profile heterogeneity due to inclusion of impermeable components, edge effects, *etc*. Figure 6.8 compares three lenses: a monolithic PDMS lens and two cavity style lenses (50 μm top/bottom RGP lenses) with air and PDMS filler, respectively. Oxygenation is observed to be consistent over the contact lenses despite the inclusion of the impermeable GTLS, highlighting the effectiveness of cavity style designs. The monolithic PDMS lens provides superior oxygenation of the cornea.

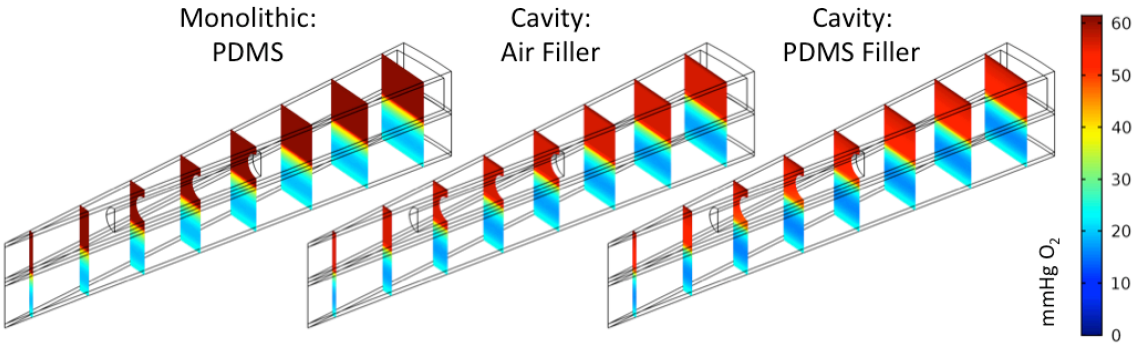

Figure 6.8: Slices of oxygen tension throughout contact on cornea COMSOL model for a monolithic PDMS lens and two cavity style lenses (50 µm top/bottom RGP lenses) with air and PDMS filler, respectively.

Effect of Embedding Impermeable Components in Lenses

When an impermeable component is embedded into a contact lens it obstructs oxygen transmission, especially if its dimensions are at least comparable to the lens thickness. In these cases, the effective transmissibility is reduced to $\left(\frac{Dk}{t}\right)' = \left(\frac{Dk}{t}\right)\left(\frac{A_{lens}-A_{obstruction}}{A_{lens}}\right)$, which can become significant for large or numerous components.

A strategy for overcoming this problem is to design a high permeability shell around the impermeable component to shunt oxygen. This can be accomplished by oversizing the cavity slightly to leave an air path or by encapsulating the component in a high permeability material like silicone. The relationship between component size, shape, shell thickness, and shell permeability are computed numerically.

Two geometries are considered and modeled in 2D: a rectangular (3 mm wide × 300 µm thick) and cylindrical (300 µm diameter) obstruction. The lens is composed of a

top and bottom portion, each 50 μm thick. The lenses are separated by a 400 μm void space of filler. The obstruction has a 50 μm shell around it. The composition/permeability of the filler and shell material are varied to understand the implications on overall lens performance.

Rectangular Obstruction in Lenses

A rectangular obstruction would include a silicon chip embedded in a contact lens and is therefore of interest. Figure 6.9 summarizes the simulation results for a rectangular obstruction as a function of shell and filler materials.

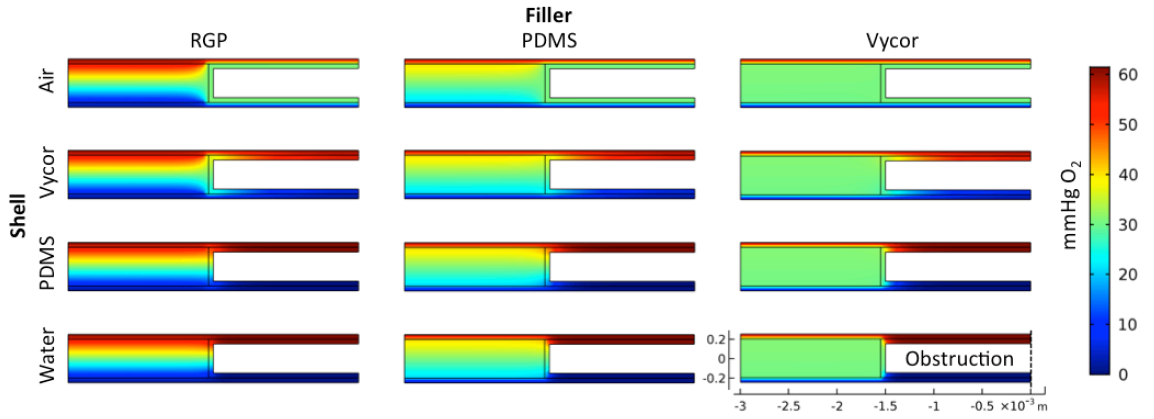

Figure 6.9: Oxygen profiles of lenses containing a 3 mm wide × 300 μm thick rectangular obstruction (white) with symmetry about right edge indicated by dashed mirror line. Upper and lower lenses are RGP; filler as indicated: Vycor, PDMS, RGP; and shell as indicated: air, Vycor, PDMS, water.

The obstruction can be modeled as a reduction in the effective surface area of the lens by comparing transmissivity with and without the obstruction:

$$A_{obstruction} = A_{lens}\left(1 - \frac{\left(\frac{Dk}{t}\right)'}{\left(\frac{Dk}{t}\right)}\right)$$

Note that the transmissivity of the unobstructed lens $\left(\frac{Dk}{t}\right)$ should be for a geometry with the minimum void width to enclose the obstruction, not the obstruction and shell. Otherwise, the metric biases towards the addition of a shell despite the fact that adding the shell can increase overall void width and hence the decrease the transmissivity of the rest of the lens that would otherwise have been higher.

To measure the effectiveness of the shell in shunting oxygen around the obstruction, a useful metric is to compare the effective obstruction area, $A_{obstruction}$, to the projected area of the obstruction, $A_{projected}$. For $A_{obstruction}/A_{projected} < 1$, the shell acts to reduce the obstruction; at $A_{obstruction}/A_{projected} = 0$ the shell completely eliminates the obstruction; for $A_{obstruction}/A_{projected} < 0$ the shell is shunting oxygen more effectively than transmission through the unobstructed lens, thereby increasing the effective surface area of the lens. Figure 6.10 plots this metric for the various lens combinations.

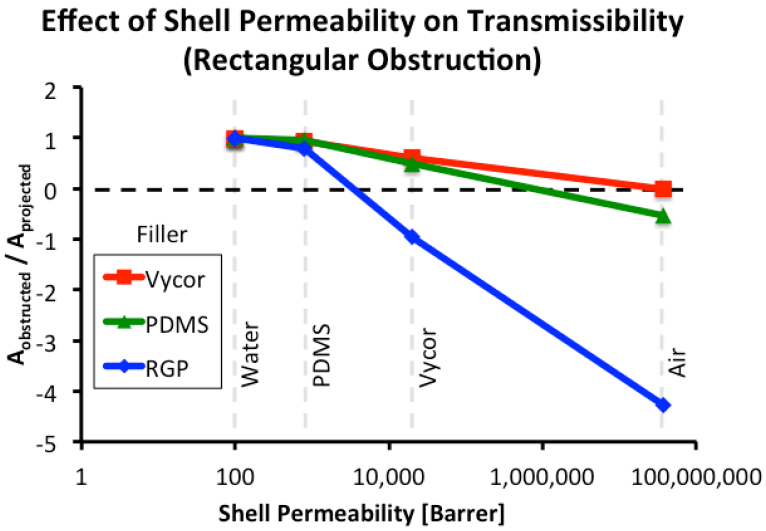

Figure 6.10: Effect of shell permeability (air, Vycor, PDMS, water) on effective obstruction area for a rectangular object.

As can be observed, for relatively large obstructions (*e.g.* 3 mm width) it is necessary to include an air shell (50 μm) around the object in order to avoid reductions in transmissivity; smaller air shells could be utilized but achieving such tolerance at these scales becomes challenging.

Cylindrical Obstruction in Lenses

Similarly, a cylindrical obstruction is considered as it models the inclusion of GTLS elements within the lens. Figure 6.11 summarizes the simulation results for a cylindrical obstruction as a function of shell and filler materials.

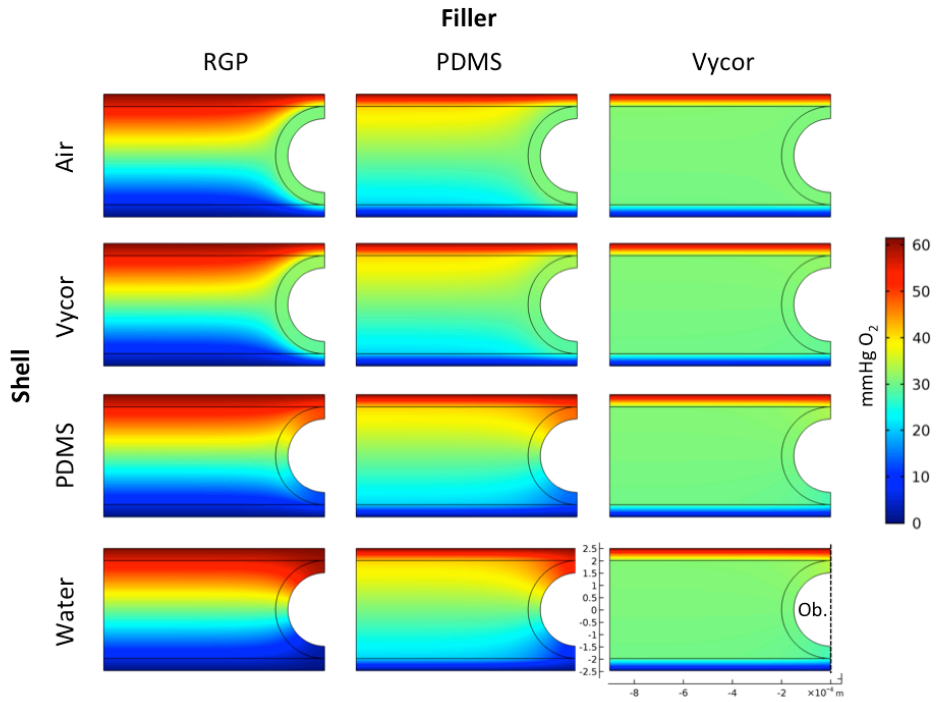

Figure 6.11: Oxygen profiles of lenses containing a 300 μm diameter cylindrical obstruction (symmetry about right edge, dashed mirror line). Upper and lower lenses are RGP, filler as indicated (Vycor, PDMS, RGP), and shell as indicated (air, Vycor, PDMS, water).

A similar analysis as performed in section "Rectangular Obstruction" can be done to measure the effectiveness of the shell in shunting oxygen around the cylindrical obstruction. Figure 6.12 plots this metric for the various lens combinations. Given the smaller dimensions of the obstruction, lower permeability shell material can be effective.

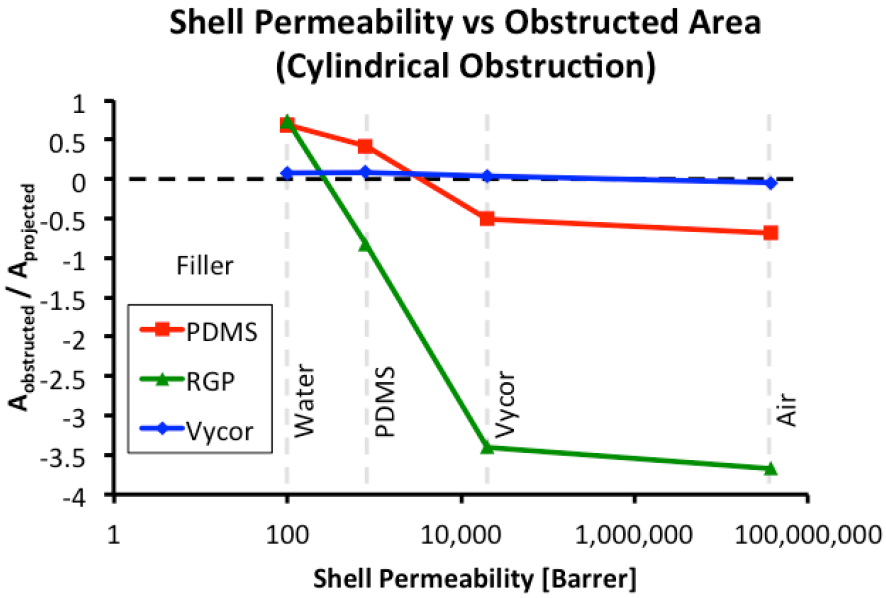

Figure 6.12: Effect of shell permeability (air, Vycor, PDMS, water) on effective obstruction area of a cylindrical object.

Min and Max Values of Transmissivity and Overall Lens Design Optimization

Lens design should be optimized to maximize lens oxygen transmissibility with possible constraints on *minimum local transmissibility*. The constraint is not well established in the literature as most lenses have a thick central region without obstructions and this is taken as the transmissibility of the lens. However, the encapsulation of impermeable components into the lens could cause underlying corneal oxygenation to be low, since lateral diffusion of oxygen is negligible over component length scales. This necessitates consideration of local transmissivity, which is taken as the

local flux through the bottom surface of the lens divided by the partial pressure difference across the lens, $\left(\frac{Dk}{t}\right)(x) = J(x)/\Delta P$.

While clinically acceptable levels of localized corneal hypoxia have not been characterized, the previous guidelines of corneal flux (6 μl/hr/cm^2 [163]) or Michaelis-Menten constant for corneal oxygen uptake (20 mmHg [189]**)** may be considered. The COMSOL simulations of rectangular obstructions are extended here to include underlying corneal tissue oxygenation (Figure 6.13), from which corneal flux is also calculated (Figure 6.14). Regions of the cornea below the 20 mmHg threshold are indicated by a contour line.

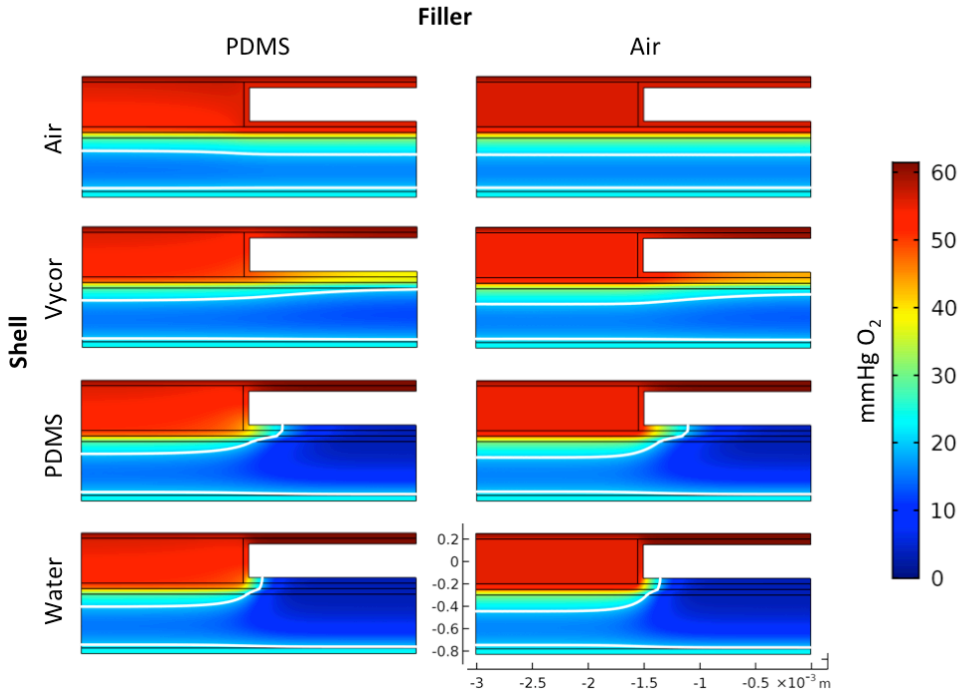

Figure 6.13: Effect of rectangular obstruction in contact lens on corneal oxygenation. Shell and filler materials are indicated for the composite lens. White contour lines demarcate regions below Michaelis-Menten constant of cornea, K_m = 20 mmHg.

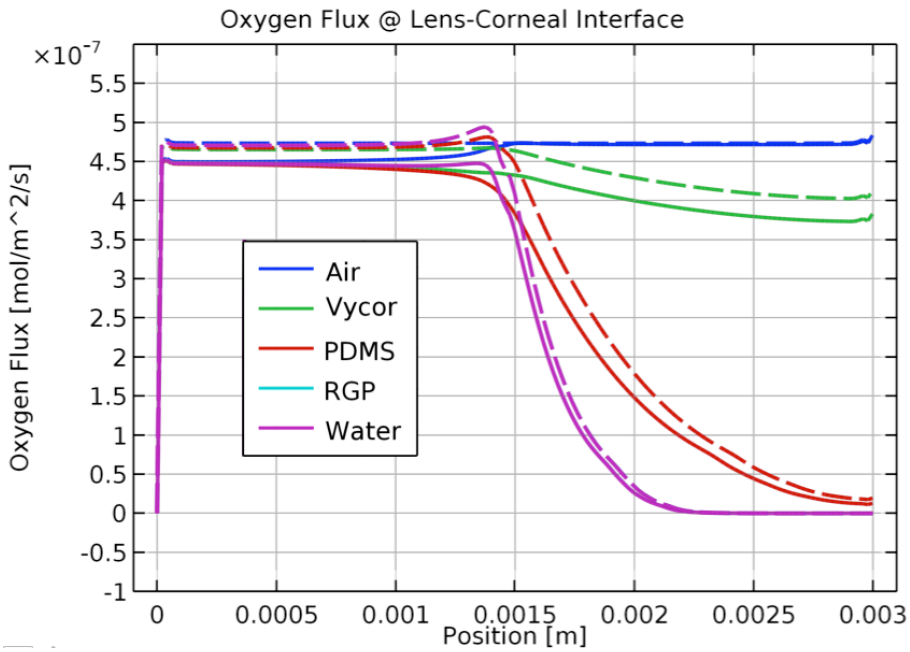

Figure 6.14: Effect of rectangular obstruction in contact lens on corneal oxygen flux to underlying corneal tissue. Shell materials are indicated in the legend with filler materials of either PDMS (solid) or air (dashed).

Compared to the regular oxygen profile under homogenous contact lenses, where hypoxia increases through the tissue depth, an embedded obstruction can cause the most severe hypoxia to occur in the epithelium. This may exacerbate corneal edema since it increases the diffusional distance lactate must travel for clearance into the aqueous humor. Another consideration is that local corneal edema may change the profile of the cornea resulting in poor lens fitting. Lifting of the lens may result in a tear film forming underneath which further decreases the oxygen permeability of the other portions of the lens. Consideration of local oxygen transmissibility will be important in future contact lens designs featuring embedded components.

CHAPTER 7 – Fabrication Techniques

Key Take-Aways
• High resolution molds for casting PDMS parts can be fabricated utilizing a dry-film photoresist process • Electrochemical etching provides a rapid means of producing high resolution metal parts

Dry Film Photoresist Molding

Need for High Resolution Molds

The rapid fabrication of high-resolution molds is of great utility in MEMS, especially for the casting of silicone parts (*e.g.* contact lenses, intraocular lenses, implants). Conventional approaches for mold making include CNC milling, lathing, and electrical discharge machining. However, these approaches are generally slow and expensive for high-resolution molds. An alternative method is to produce molds using negative photoresists (*e.g.* SU-8 epoxy), which involves the alternating steps of depositing a resist layer followed by UV exposure to pattern the layer [190]. For relatively thin molds, such as those used in microfluidics, this process is quite reliable, quick, and provides good resolution. However, for parts requiring relatively thick molds (*i.e.* >100-200 μm) or large molds, SU-8 can prove challenging due to its sensitivity to the processing parameters [191].

This need led to the initial development by Nicholas Scianmarello and Jun Park of an analogous photo-patterned negative photoresist process utilizing dry-film photoresist

instead. Dry-film photoresists generally consist of a photosensitive layer of negative resist sandwiched between a polyester film carrier layer and a polyethylene film protective layer [192]. Monomer, photo initiator, adhesion promoter, binder, and dye comprise the photosensitive layer. Exposure of the photosensitive layer to UV results in the production of free radicals via the photo initiator, which induces polymerization of the monomer. Unexposed regions can be removed with a developer that dissolves the monomer and binder. Dry-film is available in thickness from 1-150 μm and is typically laminated onto a substrate, providing a uniform thickness of resist, free of edge-bead. Sequential lamination and exposure of dry film layers followed by development allows for the facile production of high-resolution molds.

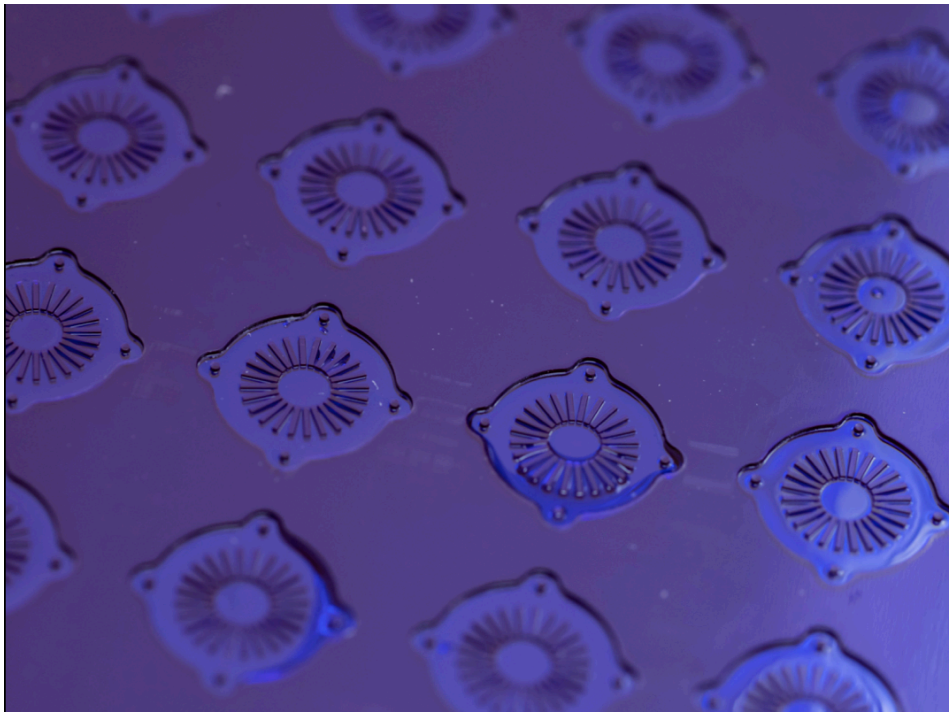

Figure 7.1: High-resolution dry film photoresist mold for PDMS contact lens fabrication.

Over the course of this thesis work, the dry film photoresist molding process has been used extensively and several optimizations to the process have been made, resulting in better mold fidelity and yield. The point of this chapter is to outline this optimized process and explain the rational behind it.

Optimized Process for Dry Film Molds

A flat substrate (*e.g.* silicon wafer or glass slide) is thoroughly cleaned. A Piranha bath (3 H_2SO_4 : 1 H_2O_2, 120 °C, >10 min) followed by an extensive rinse in DI water is generally advised, although rinsing with acetone, IPA, DI water may be sufficient. The substrate should be dried prior to use under nitrogen.

A laminator (Eagle 35 from GBC, IL) was used in this process along with WBR 2000 Series dry film photoresist of 120 μm thickness (WBR2120 from DuPont, USA) [193]. The dry film is installed on the laminator such that the polyester carrier film is peeled away, leaving only the polyethylene layer and resist layer going over the heated roller with the resist layer facing outwards. The roller temperature should be set to 95°C, the pressure lever set in the 3rd position, and the speed set to 1.

The substrate is placed on a carrier sheet to help pull it through the laminator as well as to prevent the dry-film from laminating itself to the bottom roller. Lint-free cleanroom paper or waste polyester sheeting from previous runs works well. It is recommended that an initial layer of dry film photoresist is applied to the wafer, trimmed with a fresh razor blade around the edge of the substrate, and exposed (260-520 mJ/cm^2/120 μm), excluding a small peripheral border, to provide strong adhesion to the substrate as well as provide an ideal surface for the bonding of small features on

subsequent layers. If this is not done, such features are liable to release from the substrate during the final development step.

Additional layers of dry film resist are laminated similarly, making sure to remove the protective polyethylene film between successive laminations. The desired thickness of the layer is achieved through multiple laminations prior to exposure.

When constructing a mold composed of multiple layers, there are two approaches each with strengths and drawbacks. In the first approach, all lamination and exposure steps are done sequentially without intermittent soft baking as is recommended by the manufacturer (65 °C, 20 min) to improve adhesion to the substrate. The rationale is that during soft baking there is contraction of the resist layer, which induces a tensile stress in the resist. Repeated lamination and soft baking causes this stress to add with each layer, leading to significant wafer bowing and increased risk of delamination. Another consideration is the 20 min dwell time significantly slows down the process. One of the drawbacks of this approach is that the resist has not contracted prior to exposure so the fidelity between mask and mold geometry is not perfect. In most cases, the slight difference is acceptable due either to the fact that all parts are similarly scaled, that the elasticity of the PDMS cast in the molds can accommodate slight mismatches in geometry, or that the contraction of PDMS during curing (*e.g.* to 98% of designed linear dimensions in Sylguard 184) is more significant. For a cleaned substrate, it is generally unnecessary to perform a soft bake and the adhesion between successive layers of photoresist is sufficiently strong; however, if one is having adhesion problems to the substrate itself, performing a soft bake after the initial resist layer is laminated may alleviate these problems.

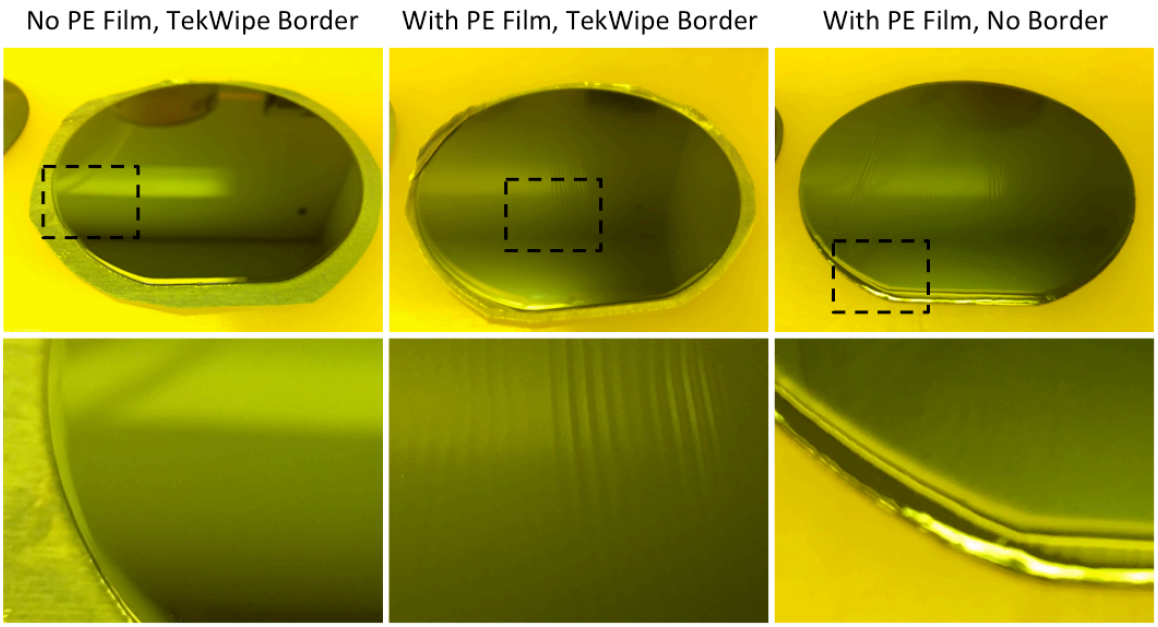

Figure 7.2: Optimization of soft baking conditions for dry film photoresist. (Left) Edge-to-edge mirror flat surface achieved after soft bake with PE film removed and carrier border remaining. (Middle) Waves appear in the resist film if PE film is left on during soft baking. (Right) Contraction of photoresist film occurs if carrier border is removed prior to soft bake.

In the second approach, the dry film is soft baked (65 °C, 20 min) after each (set of) lamination(s). If this is done, it is critical to remove the protective polyethylene film before baking otherwise differential thermal expansion between the polyethylene and the photoresist layer will compromise flatness. The advantage of this approach is that the film has constricted prior to exposure so that the fidelity of the mold and mask is optimal; however, the multiple soft bakes required slow down the process. Additionally, the removal of the polyethylene film now introduces the risk of resist adhesion to the mask glass during exposure. The user can either reapply the removed polyethylene layer or pre-

coat the mask with >1 μm of Parylene (*e.g.* C). Pre-coating masks with Parylene results in a superior top surface finish of the layer compared to reapplying polyethylene, which tends to imprint texture as observed in Figure 7.3.

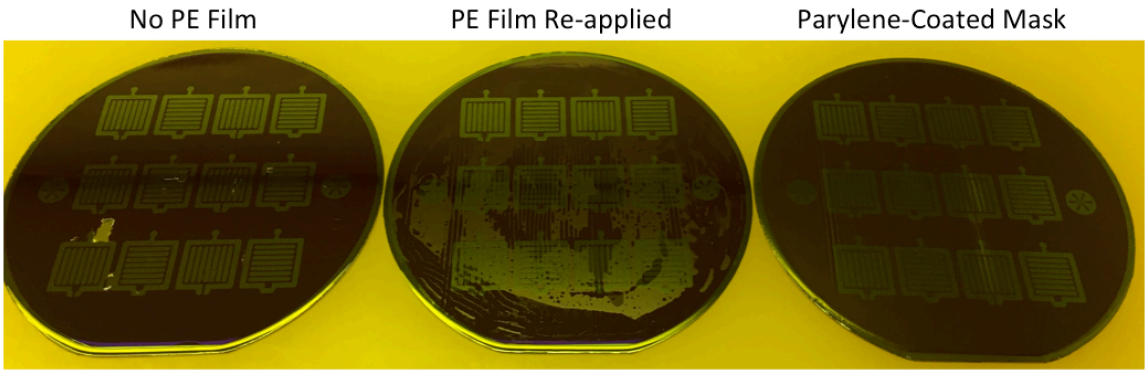

Figure 7.3: Considerations for exposure. (Left) Adhesion of photoresist to glass mask during exposure can lead to delamination of mold. (Middle) Re-application of PE film prevents adhesion but imprints film surface. (Right) Coating mask with Parylene prevents adhesion and maintains a smooth top surface.

For molds composed of multiple layers, it is necessary to perform alignment with marks on the photoresist. Unfortunately, the contrast between exposed and unexposed dry film is very subtle and the transparency of thick dry film is low making the process of alignment difficult or impossible. If alignment is needed, it is recommended that a piece of polyethylene film be placed over the alignment marks of the bottom layer prior to lamination of the next layer, locally preventing adhesion. Then with a razor blade, the overlaying dry film can be cut and peeled away to reveal the alignment pattern, as shown in Figure 7.4. If needed, a drop of developer can be placed on the alignment mark to locally develop it to improve contrast during the alignment process.

Figure 7.4: Removal of overlaying dry film resist ensures that alignment marks are visible.

Once the lamination and exposure of the various layers is complete, the mold should be post-exposure baked to complete polymerization of exposed regions (85 °C, 25 min) and allowed to cool gradually to room temperature. Development of the dry film photoresist is carried out in a solution of 1 part AZ 340 to 4 parts DI-water under agitation. It is convenient to carry this out in a cylindrical dish with a stir bar (~300 rpm is sufficient) and wafer holder. Place the wafer in a wafer holder so that the dry film photoresist side is facing down and is high enough that it will not contact the stir bar. Tilt the dish to ensure there are no air bubbles under the wafer. Development takes approximately 5 min per layer. Development can be accelerated by running the wafer under DI-water once the unexposed dry film photoresist has turned milky in color. This reduces the amount of time that the wafer is in developer and hence reduces the

likelihood of delamination. Since delamination occurs due to developer attack at the dry film resist and substrate interface, it is recommended that an unexposed periphery be left on the bottom most layer to act as a sacrificial region, preventing infiltration of developer. Alternatively, a specialized dish can be used that seals against the mold to contain the developer directly over regions to be developed and away from the peripheral edge of the dry film resist and substrate. Either approach practically eliminates the mold delamination, which is otherwise a significant cause of low yield.

Once development is complete, the mold should be thoroughly rinsed in DI-water, spin dried, and allowed to equilibrate at room temperature and humidity. This is necessary to prevent warping and delamination from occurring during subsequent exposure to vacuum if Parylene coating is carried out as a mold release layer for PDMS. A 5-10 μm coating of Parylene is sufficient to allow the mold to be reused several times.

Dry film photoresist molds coated with Parylene can be used to cast PDMS parts. The PDMS is prepared according to the manufacturer's instructions and degassed under vacuum. It is then poured into the mold and squeegeed to achieve a relatively flat surface. The PDMS-filled mold can then be degassed a second time to ensure infiltration of PDMS into small features of the mold. A smooth surface is finally achieved by squeegeeing with a fresh razor blade (at an approximately 45° angle) over the mold surface. This is particularly effective because it cleanly removes PDMS from the peripheral edge of the molds, eliminating the need to manually remove flash after curing. Dry film photoresist molds can withstand temperatures of up to 120 °C allowing them to be used for rapid thermal curing of PDMS.

Electrochemical Etching

Stainless Steel

The production of fine metal structures can be accomplished utilizing a galvanically-enhanced etching process, known as electrochemical etching. The advantage of the process is that relatively mild etchant can be used (*e.g.* saline) and the etching speed can be accelerated. The substrate to be etched is patterned with a protective resist and connected to the anode of a DC power supply while an electrode of similar material to that being etched acts as the cathode. An electrolyte solution, composed either of ions of the metal to be etched or otherwise, completes the circuit. The application of electrical potential extracts electrons from the metal to be etched, producing soluble ions that can dissolve away into the electrolyte solution (Table 7.1).

Table 7.1: Standard electrode potentials of major components of stainless steel.

$Fe^{2+} + 2e^- \xrightarrow{-0.44V} Fe$
$Cr^{3+} + 3e^- \xrightarrow{-0.74V} Cr$
$Ni^{2+} + 2e^- \xrightarrow{-0.25V} Ni$

A custom setup was assembled composed of a DC power supply (TP343A from Power Designs, NY), alligator-to-banana leads, stainless steel cathode, substrate anode, etching container, and brine (electrolyte). The metal to be etched (*e.g.* 304 stainless steel, 0.001” thick, #63045 by Trinity Brand Industries, IL) was adhered to a substrate wafer (*e.g.* with a thin film of photoresist or with copper tape) and patterned with AZ 1518 photoresist (2.5 μm thick). The wafer was then installed into a container that seals up

against the wafer to form a reservoir for the electrolyte while allowing external access to the metal substrate for connection to the anode lead.

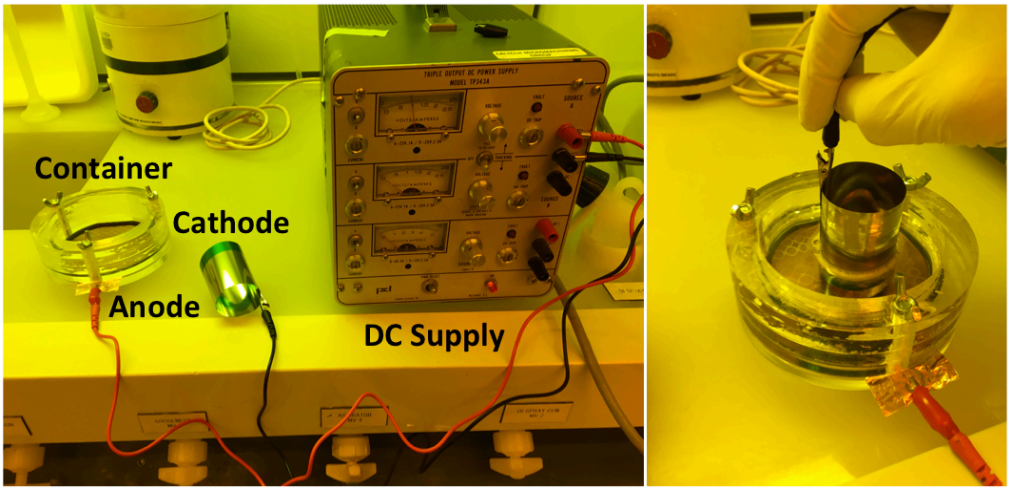

Figure 7.5: Electrochemical etching setup comprised of DC power supply, stainless steel cathode, substrate anode, and etching container.

The power supply was operated at 5-10 V and the etching process was controlled manually by inserting/removing the cathode. Due to the evolution of chlorine and hydrogen gas during the process, it was carried out in a fume hood. Progression of the etching was monitored using a microscope.

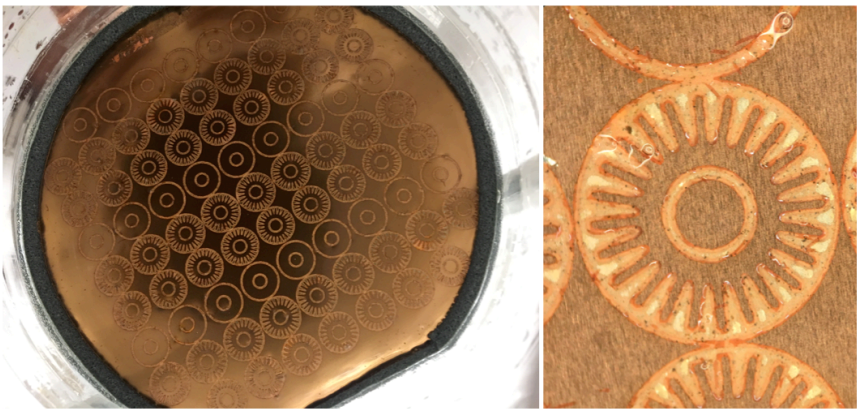

Figure 7.6: Etched stainless steel reflectors on copper backing.

Copper Etching

Copper traces can be easily formed through a chemical etching process. Traces were etched from copper shim (Alloy 110 Annealed Temper, 0.001" thick, CUX-1 by Lyon Industries, IL) according to an established recipe, utilizing AZ 1518 positive photoresist as a mask [194]. The etchant solution was composed of 70 mL hydrochloric acid (12.1 M) and 30 mL hydrogen peroxide (30%) in 900 mL deionized water and achieves an etch rate of ~1 μm/min at room temperature under mild agitation.

Flexible Copper-on-Parylene Circuit Boards

Techniques for flexible circuits continue to be developed to accommodate requirements in non-planar applications such as wearable electronics [195]. Many approaches are based on lamination of copper to a thin, flexible polymer substrate such as polyimide or polyester via an adhesive. For biomedical applications, such polymers pose biocompatibility concerns, adhesives can undergo degradation, and substrates remain fairly stiff and lack transparency. Parylene, as a highly biocompatible, temperature/chemical resistant, and CVD polymer, has emerged as a candidate for flexible circuit applications. The typical processing strategy is to deposit a layer of Parylene onto a substrate coated with a release agent and then use photolithography, metal evaporation, and electroplating to produce traces on the Parylene, followed by a sealing layer of Parylene [196]. For certain applications this is suitable; however, it often requires a fairly thick film of Parylene (8-10 μm) in order to successfully peel from the substrate without tearing [197]. It also requires the multiple steps of metal evaporation and electroplating to achieve thick traces.

An alternative processing strategy was developed that simplifies the fabrication of flexible Parylene circuit boards and allows for significantly thinner Parylene substrate while allowing thick copper traces. In this approach, a copper sheet (0.001", 25.4 μm thick) was cleaned (acetone, isopropyl alcohol, deionized water) and then a release was applied to one side (2% Micro-90 in DI-water from VWR, PA) and allowed to dry. The sheet was then coated with 2.5 μm Parylene C (DPX-C from Specialty Coating Systems, IN; manufactured by Galentis, IT). Subsequently, the Parylene was peeled off the side with release, rinsed with deionized water, and dried under nitrogen. Photoresist was applied to the exposed copper face via spin coating (AZ 1518, 2000 rpm) to approximately 2.5 μm and soft baked (30 min, 100 °C). Photomasks of the traces were exposed under UV (80 s; 405 nm: 4.12 mW/cm^2, 365 nm: 1.63 mW/cm^2) on a contact aligner (MA-56 from Karl Suss, DE). The photoresist was then developed (1 part AZ 340, 4 parts deionized water, 60 s). The copper was etched (as above) through to the Parylene backing to produce the traces. Photoresist was stripped by rinsing with acetone, IPA, and deionized water.

Figure 7.7: Copper on Parylene flexible circuit board fabrication. (Left) Photoresist patterned and developed on exposed copper, (Middle) midway through copper etching, (Right) Completed traces after stripping photoresist.

Through such a process, flexible copper traces can easily be produced on a thin Parylene substrate. Given that it is a subtractive process, one may need to account for undercutting of the photoresist and scale feature widths according to the thickness of the copper substrate.

REFERENCES

[1] R. Lee, T. Y. Wong, and C. Sabanayagam, "Epidemiology of diabetic retinopathy, diabetic macular edema and related vision loss," *Eye Vis.*, vol. 2, no. 1, p. 17, 2015.

[2] R. Klein, B. E. K. Klein, S. E. Moss, M. D. Davis, and D. L. DeMets, "The Wisconsin Epidemiologic Study of Diabetic Retinopathy," *Arch. Ophthalmol.*, vol. 102, no. 4, p. 527, Apr. 1984.

[3] J. J. Kovarik, A. W. Eller, L. A. Willard, J. Ding, J. M. Johnston, and E. L. Waxman, "Prevalence of undiagnosed diabetic retinopathy among inpatients with diabetes: the diabetic retinopathy inpatient study (DRIPS)," *BMJ Open Diabetes Res. Care*, vol. 4, no. 1, p. e000164, 2016.

[4] N. Kourgialis, "Diabetic Retinopathy - silently blinding millions of people world-wide • IAPB Vision Atlas," *IAPB Vision Atlas*. [Online]. Available: http://atlas.iapb.org/vision-trends/diabetic-retinopathy/. [Accessed: 03-Dec-2017].

[5] Alliance, "The Silver Book : Diabetic Retinopathy," *Alliance aging Res.*, 2016.

[6] "The Caring for Diabetes Educational Forum." [Online]. Available: http://www.caringfordiabetes.com/Continuing-Education/. [Accessed: 03-Dec-2017].

[7] X. Zhang, S. Low, N. Kumari, J. Wang, K. Ang, D. Yeo, C. C. Yip, S. Tavintharan, C. F. Sum, and S. C. Lim, "Direct medical cost associated with diabetic retinopathy severity in type 2 diabetes in Singapore," pp. 1–11, 2017.

[8] T. Y. Wong, C. M. G. Cheung, M. Larsen, S. Sharma, and R. Simó, "Diabetic retinopathy," *Nat. Rev. Dis. Prim.*, vol. 2, p. 16012, Mar. 2016.

[9] D. M. Nathan, "The diabetes control and complications trial/epidemiology of diabetes interventions and complications study at 30 years: Overview," *Diabetes Care*, vol. 37, no. 1, pp. 9–16, 2014.

[10] ADVANCE Collaborative Group, A. Patel, S. MacMahon, J. Chalmers, B. Neal, L. Billot, M. Woodward, M. Marre, M. Cooper, P. Glasziou, D. Grobbee, P. Hamet, S. Harrap, S. Heller, L. Liu, G. Mancia, C. E. Mogensen, C. Pan, N. R. Poulter, A. Rodgers, B. Williams, S. Bompoint, B. E. de Galan, R. Joshi, F. Travert, and The ADVANCE Collaborative Group, "Intensive Blood Glucose Control and Vascular Outcomes in Patients with Type 2 Diabetes," *New Engl J Med*, vol. 358, no. 24, pp. 2560–2572, 2008.

[11] I. P. Chatziralli, "The Role of Glycemic Control and Variability in Diabetic Retinopathy," *Diabetes Ther.*, vol. 9, no. 1, pp. 431–434, 2018.

[12] D. S. W. Ting, G. C. M. Cheung, and T. Y. Wong, “Diabetic retinopathy: global prevalence, major risk factors, screening practices and public health challenges: a review,” *Clin. Exp. Ophthalmol.*, vol. 44, no. 4, pp. 260–277, 2016.

[13] T. Reinehr, “Type 2 diabetes mellitus in children and adolescents.,” *World J. Diabetes*, vol. 4, no. 6, pp. 270–81, Dec. 2013.

[14] A. P. Schachat, C. P. Wilkinson, D. R. Hinton, S. R. Sadda, and P. Wiedemann, *Ryan’s Retina*, 6th ed. Elsevier, 2017.

[15] R. Klein, B. Klein, S. Moss, M. Davis, and D. DeMets, “The Wisconsin Epidemiologic Study of Diabetic Retinopathy - II. Prevalence and Risk of Diabetic Retinopathy When Age at Diagnosis Is Less Than 30 Years,” *Arch. Ophthalmol.*, vol. 102, pp. 520–526, 1984.

[16] R. Klein, B. Klein, S. Moss, M. Davis, and D. DeMets, “The Wisconsin Epidemiologic Study of Diabetic Retinopathy- III. Prevalence and Risk of Diabetic Retinopathy When Age at Diagnosis Is 30 or More Years,” *Arch. Ophthalmol.*, vol. 102, pp. 527–532, 1984.

[17] G. Wyszecki and W. S. (Walter S. Stiles, *Color science : concepts and methods, quantitative data, and formulae*. John Wiley & Sons, 2000.

[18] N. Efron, *Contact lens practice*, 3rd ed. Elsevier, 2017.

[19] Jmarchn, “Schematic diagram of human eye multilingual,” *Wikimedia Commons*, 2016. [Online]. Available: https://commons.wikimedia.org/wiki/File: Schematic_diagram_of_human_eye_multilingual.svg. [Accessed: 19-Nov-2018].

[20] S. L. Polyak, *The Retina*. Chicago University Press, 1941.

[21] Danny Hope, “Macula,” *Wikimedia Commons*, 2014. [Online]. Available: https://commons.wikimedia.org/wiki/File:Macula.svg. [Accessed: 19-Nov-2018].

[22] J. P. Campbell, M. Zhang, T. S. Hwang, S. T. Bailey, D. J. Wilson, Y. Jia, and D. Huang, “Detailed Vascular Anatomy of the Human Retina by Projection-Resolved Optical Coherence Tomography Angiography.,” *Sci. Rep.*, vol. 7, p. 42201, 2017.

[23] G. L. Semenza, “Hydroxylation of HIF-1: Oxygen Sensing at the Molecular Level,” *Physiology*, vol. 19, no. 4, pp. 176–182, 2004.

[24] E. J. Duh, J. K. Sun, and A. W. Stitt, “Diabetic retinopathy: current understanding, mechanisms, and treatment strategies.,” *JCI insight*, vol. 2, no. 14, Jul. 2017.

[25] N. D. Wangsa-Wirawan and R. A. Linsenmeier, “Retinal Oxygen,” *Arch. Ophthalmol.*, vol. 121, no. 4, p. 547, Apr. 2003.

[26] D. Y. Yu and S. J. Cringle, “Oxygen distribution and consumption within the retina in vascularised and avascular retinas and in animal models of retinal disease,” *Progress in Retinal and Eye Research*, vol. 20, no. 2. pp. 175–208, 2001.

[27] G. Birol, S. Wang, E. Budzynski, N. D. Wangsa-Wirawan, and R. A. Linsenmeier, “Oxygen distribution and consumption in the macaque retina,” *Am J Physiol Hear. Circ Physiol*, vol. 293, no. 3, pp. H1696-704, 2007.

[28] D. De Brouwere and C. Dainty, *Retinal Oximetry*, no. June. 2012.

[29] J. Ahmed, R. D. Braun, R. Dunn, and R. A. Linsenmeier, “Oxygen distribution in the macaque retina.,” *Invest. Ophthalmol. Vis. Sci.*, vol. 34, no. 3, pp. 516–21, Mar. 1993.

[30] R. F. Gariano, M. L. Iruela-Arispe, and A. E. Hendrickson, “Vascular development in primate retina: comparison of laminar plexus formation in monkey and human.,” *Invest. Ophthalmol. Vis. Sci.*, vol. 35, no. 9, pp. 3442–55, Aug. 1994.

[31] R. M. Werkmeister, D. Schmidl, G. Aschinger, V. Doblhoff-Dier, S. Palkovits, M. Wirth, G. Garhöfer, R. A. Linsenmeier, R. A. Leitgeb, and L. Schmetterer, “Retinal oxygen extraction in humans,” *Sci. Rep.*, vol. 5, no. 1, p. 15763, Dec. 2015.

[32] M. Hammer, W. Vilser, T. Riemer, A. Mandecka, D. Schweitzer, U. Kühn, J. Dawczynski, F. Liemt, and J. Strobel, “Diabetic patients with retinopathy show increased retinal venous oxygen saturation,” *Graefe’s Arch. Clin. Exp. Ophthalmol.*, vol. 247, no. 8, pp. 1025–1030, Aug. 2009.

[33] S. H. Hardarson and E. Stefánsson, “Retinal oxygen saturation is altered in diabetic retinopathy,” *Br. J. Ophthalmol.*, vol. 96, no. 4, pp. 560–563, Apr. 2012.

[34] C. M. Jørgensen, S. H. Hardarson, and T. Bek, “The oxygen saturation in retinal vessels from diabetic patients depends on the severity and type of vision-threatening retinopathy,” *Acta Ophthalmol.*, vol. 92, no. 1, pp. 34–39, Feb. 2014.

[35] F. Tayyari, L.-A. Khuu, J. G. Flanagan, S. Singer, M. H. Brent, and C. Hudson, “Retinal Blood Flow and Retinal Blood Oxygen Saturation in Mild to Moderate Diabetic Retinopathy,” *Investig. Opthalmology Vis. Sci.*, vol. 56, no. 11, p. 6796, 2015.

[36] I. Leopold, “Capillary shunts in the pathogenesis of diabetic retinopathy.,” *Diabetes*, vol. 12, no. 4, pp. 349–50, Jul. 1963.

[37] S. I. Sherwani, H. A. Khan, A. Ekhzaimy, A. Masood, and M. K. Sakharkar, “Significance of HbA1c Test in Diagnosis and Prognosis of Diabetic Patients.,” *Biomark. Insights*, vol. 11, pp. 95–104, 2016.

[38] A. W. Stitt and T. M. Curtis, “Advanced glycation and retinal pathology during diabetes.,” *Pharmacol. Rep.*, vol. 57 Suppl, pp. 156–68, 2005.

[39] S. N. Jespersen and L. Østergaard, “The roles of cerebral blood flow, capillary transit time heterogeneity, and oxygen tension in brain oxygenation and metabolism.,” *J. Cereb. Blood Flow Metab.*, vol. 32, no. 2, pp. 264–77, Feb. 2012.

[40] L. Østergaard, N. B. Finnerup, A. J. Terkelsen, R. A. Olesen, K. R. Drasbek, L. Knudsen, S. N. Jespersen, J. Frystyk, M. Charles, R. W. Thomsen, J. S. Christiansen, H. Beck-Nielsen, T. S. Jensen, and H. Andersen, “The effects of capillary dysfunction on oxygen and glucose extraction in diabetic neuropathy.,” *Diabetologia*, vol. 58, no. 4, pp. 666–77, Apr. 2015.

[41] N. M. Holekamp, Y.-B. Shui, and D. Beebe, “Lower Intraocular Oxygen Tension in Diabetic Patients: Possible Contribution to Decreased Incidence of Nuclear Sclerotic Cataract,” *Am. J. Ophthalmol.*, vol. 141, no. 6, pp. 1027–1032, Jun. 2006.

[42] X. Chen, B. S. Modjtahedi, and L. H. Young, “Management of Diabetic Macular Edema,” *Int. Ophthalmol. Clin.*, vol. 55, no. 4, pp. 113–122, 2015.

[43] E. Stefánsson, “The Mechanism of Retinal Photocoagulation – How Does the Laser Work?,” *Eur. Ophthalmic Rev.*, pp. 76–79, 2008.

[44] L. P. Aiello, R. L. Avery, P. G. Arrigg, B. A. Keyt, H. D. Jampel, S. T. Shah, L. R. Pasquale, H. Thieme, M. A. Iwamoto, J. E. Park, H. V. Nguyen, L. M. Aiello, N. Ferrara, and G. L. King, “Vascular Endothelial Growth Factor in Ocular Fluid of Patients with Diabetic Retinopathy and Other Retinal Disorders,” *N. Engl. J. Med.*, vol. 331, no. 22, pp. 1480–1487, Dec. 1994.

[45] G. B. Arden and D. J. Ramsey, “Diabetic retinopathy and a novel treatment based on the biophysics of rod photoreceptors and dark adaptation,” pp. 1–57, 2015.

[46] K. Nishijima, Y.-S. Ng, L. Zhong, J. Bradley, W. Schubert, N. Jo, J. Akita, S. J. Samuelsson, G. S. Robinson, A. P. Adamis, and D. T. Shima, “Vascular endothelial growth factor-A is a survival factor for retinal neurons and a critical neuroprotectant during the adaptive response to ischemic injury.,” *Am. J. Pathol.*, vol. 171, no. 1, pp. 53–67, Jul. 2007.

[47] “Diabetic Macular Edema Market - Global Industry Analysis, Size and Forecast, 2017 to 2027,” *Future Market Insights*. [Online]. Available: https://www.futuremarketinsights.com/reports/diabetic-macular-edema-market. [Accessed: 03-Dec-2017].

[48] “Glaucoma Treatment Market Value Projected to Hit $3 Billion by 2023,” *Glaucoma Today*, 2015. [Online]. Available: http://bmcenews.com/GlaucomaToday/2015-06-15.html. [Accessed: 03-Dec-2017].

[49] N. Taylor, “Evolution of the Age-Related Macular Degeneration Market,” *DRG*, 2017. [Online]. Available: https://decisionresourcesgroup.com/drg-blog/evolution-age-related-macular-degeneration-market/. [Accessed: 03-Dec-2017].

[50] L. Woods, “Research and Markets: The Retinal Vein Occlusion Therapeutics Market is expected to grow Due to the Launch of First-in-Class Products,” *Business Wire*, 2011. [Online]. Available: http://www.businesswire.com/news/home/20110531005717/en/Research-Markets-Retinal-Vein-Occlusion-Therapeutics-Market. [Accessed: 03-Dec-2017].

[51] “Retinal Detachment treatment Market Research Forecast 2023,” *MRFR*, 2017. [Online]. Available: https://www.marketresearchfuture.com/reports/retinal-detachment-treatment-market-1640. [Accessed: 03-Dec-2017].

[52] A. Hellström, L. E. H. Smith, and O. Dammann, “Retinopathy of prematurity.,” *Lancet (London, England)*, vol. 382, no. 9902, pp. 1445–57, Oct. 2013.

[53] H. Kolb, *Facts and Figures Concerning the Human Retina*. University of Utah Health Sciences Center, 1995.

[54] G. B. Arden, J. E. Wolf, and Y. Tsang, “Does dark adaptation exacerbate diabetic retinopathy? Evidence and a linking hypothesis,” *Vision Res.*, vol. 38, no. 11, pp. 1723–1729, 1998.

[55] PolyPhotonix, “A New Approach to the Management of Diabetic Macular Edema - Media Pack,” Sedgefield, County Durham, 2018.

[56] I. B. Leskov, V. A. Klenchin, J. W. Handy, G. G. Whitlock, V. I. Govardovskii, M. D. Bownds, T. D. Lamb, E. N. Pugh, and V. Y. Arshavsky, “The gain of rod phototransduction: reconciliation of biochemical and electrophysiological measurements.,” *Neuron*, vol. 27, no. 3, pp. 525–37, Sep. 2000.

[57] E. N. Pugh and W. H. Cobbs, “Visual transduction in vertebrate rods and cones: a tale of two transmitters, calcium and cyclic GMP.,” *Vision Res.*, vol. 26, no. 10, pp. 1613–43, 1986.

[58] E. N. Pugh, “Variability in single photon responses: a cut in the Gordian knot of rod phototransduction?,” *Neuron*, vol. 23, no. 2, pp. 205–8, Jun. 1999.

[59] W. A. Hagins, R. D. Penn, and S. Yoshikami, “Dark Current and Photocurrent in Retinal Rods,” *Biophys. J.*, vol. 10, no. 5, pp. 380–412, May 1970.

[60] H. Okawa, A. P. Sampath, S. B. Laughlin, and G. L. Fain, “ATP consumption by mammalian rod photoreceptors in darkness and in light,” *Curr. Biol.*, vol. 18, no. 24, pp. 1917–21, Dec. 2008.

[61] G. C. Demontis, B. Longoni, C. Gargini, and L. Cervetto, “The energetic cost of photoreception in retinal rods of mammals.,” *Arch. Ital. Biol.*, vol. 135, no. 2, pp. 95–109, Mar. 1997.

[62] A. Ames, Y. Y. Li, E. C. Heher, and C. R. Kimble, “Energy metabolism of rabbit retina as related to function: high cost of Na+ transport.,” *J. Neurosci.*, vol. 12, no. 3, pp. 840–53, Mar. 1992.

[63] R. D. Braun, R. A. Linsenmeier, and T. K. Goldstick, “Oxygen consumption in the inner and outer retina of the cat.,” *Invest. Ophthalmol. Vis. Sci.*, vol. 36, no. 3, pp. 542–54, Mar. 1995.

[64] R. A. Linsenmeier and R. D. Braun, “Oxygen distribution and consumption in the cat retina during normoxia and hypoxemia.,” *J. Gen. Physiol.*, vol. 99, no. 2, pp. 177–97, Feb. 1992.

[65] E. A. Kimble, R. A. Svoboda, and S. E. Ostroy, “Oxygen consumption and ATP changes of the vertebrate photoreceptor.,” *Exp. Eye Res.*, vol. 31, no. 3, pp. 271–88, Sep. 1980.

[66] M. W. Roos, “Theoretical estimation of retinal oxygenation during retinal artery occlusion,” *Physiol. Meas.*, vol. 25, no. 6, pp. 1523–32, Dec. 2004.

[67] J. M. Vanderkooi, M. Erecinska, and I. A. Silver, “Oxygen in mammalian tissue: methods of measurement and affinities of various reactions,” *Am. J. Physiol. Physiol.*, vol. 260, no. 6, pp. C1131–C1150, Jun. 1991.

[68] J. Ahmed, M. K. Pulfer, and R. A. Linsenmeier, “Measurement of Blood Flow through the Retinal Circulation of the Cat during Normoxia and Hypoxemia using Fluorescent Microspheres,” *Microvasc. Res.*, vol. 62, no. 2, pp. 143–153, Sep. 2001.

[69] B. W. Pogue, K. D. Paulsen, J. A. O’Hara, C. M. Wilmot, and H. M. Swartz, “Estimation of oxygen distribution in RIF-1 tumors by diffusion model-based interpretation of pimonidazole hypoxia and eppendorf measurements.,” *Radiat. Res.*, vol. 155, no. 1 Pt 1, pp. 15–25, Jan. 2001.

[70] S. Silbernagl and A. Despopoulos, *Color atlas of physiology*. Thieme, 2009.

[71] B. Kavanagh, R. Steffen, D. Chan, and P. Cagnoni, “RSR13 Modulates Tumor Hypoxia and HIF-1-alpha Expression in H226 Xenografts In Vivo,” *Proc. 45th Annu. ASTRO Meet.*, 2002.

[72] R. Ganfield, P. Nair, and W. Whalen, “Mass transfer, storage, and utilization of O2 in cat cerebral cortex,” *Am. J. Physiol. Content*, vol. 219, no. 3, pp. 814–821, Sep. 1970.

[73] T. W. Kraft, M. Schneeweis, and J. L. Schnapf, “Visual Transduction in Human Rod Photoreceptors,” *J. Physiol.*, vol. 464, pp. 747–765, 1993.

[74] L. M. Haugh, R. A. Linsenmeier, and T. K. Goldstick, “Mathematical models of the spatial distribution of retinal oxygen tension and consumption, including changes upon illumination,” *Ann. Biomed. Eng.*, vol. 18, no. 1, pp. 19–36, Jan. 1990.

[75] E. Stefánsson, “The Mechanism of Retinal Photocoagulation – How Does the Laser Work?,” *Eur. Ophthalmic Rev.*, vol. 02, no. 01, p. 76, 2009.

[76] S. Yun and R. Adelman, “Recent developments in laser treatment of diabetic retinopathy,” *Middle East Afr. J. Ophthalmol.*, vol. 22, no. 2, p. 157, 2015.

[77] Y.-Z. Le, “VEGF production and signaling in Müller glia are critical to modulating vascular function and neuronal integrity in diabetic retinopathy and hypoxic retinal vascular diseases.,” *Vision Res.*, vol. 139, pp. 108–114, 2017.

[78] W. Eichler, H. Kuhrt, S. Hoffmann, P. Wiedemann, and A. Reichenbach, “VEGF release by retinal glia depends on both oxygen and glucose supply.,” *Neuroreport*, vol. 11, no. 16, pp. 3533–7, Nov. 2000.

[79] J. T. S. Brooks, G. P. Elvidge, L. Glenny, J. M. Gleadle, C. Liu, J. Ragoussis, T. G. Smith, N. P. Talbot, L. Winchester, P. H. Maxwell, and P. A. Robbins, “Variations within oxygen-regulated gene expression in humans,” *J. Appl. Physiol.*, vol. 106, no. 1, pp. 212–220, 2008.

[80] B. H. Jiang, G. L. Semenza, C. Bauer, and H. H. Marti, “Hypoxia-inducible factor 1 levels vary exponentially over a physiologically relevant range of O2 tension.,” *Am. J. Physiol.*, vol. 271, no. 45, pp. C1172–C1180, 1996.

[81] W. Eichler, H. Kuhrt, S. Hoffmann, P. Wiedemann, and A. Reichenbach, “VEGF release by retinal glia depends on both oxygen and glucose supply.,” *Neuroreport*, vol. 11, no. 16, pp. 3533–7, Nov. 2000.

[82] J. Pe’er, D. Shweiki, A. Itin, I. Hemo, H. Gnessin, and E. Keshet, “Hypoxia-induced expression of vascular endothelial growth factor by retinal cells is a common factor in neovascularizing ocular diseases,” *Lab. Invest.*, vol. 72, no. 6, pp. 638–45, Jun. 1995.

[83] J. K. Bowmaker and H. J. Dartnall, “Visual pigments of rods and cones in a human retina.,” *J. Physiol.*, vol. 298, pp. 501–11, Jan. 1980.

[84] D. A. Baylor, T. D. Lamb, and K. W. Yau, “Responses of retinal rods to single photons.,” *J. Physiol.*, vol. 288, pp. 613–34, Mar. 1979.

[85] F. I. Hárosi, “Absorption spectra and linear dichroism of some amphibian photoreceptors.,” *J. Gen. Physiol.*, vol. 66, no. 3, pp. 357–82, Sep. 1975.

[86] J. L. Schnapf, B. J. Nunn, M. Meister, and D. A. Baylor, “Visual transduction in cones of the monkey Macaca fascicularis.,” *J. Physiol.*, vol. 427, pp. 681–713, Aug. 1990.

[87] H. J. A. Dartnall, “Photosensitivity,” 1972, pp. 122–145.

[88] B. H. Crawford, “The scotopic visibility function,” *Proc. Phys. Soc. Sect. B*, vol. 62, no. 5, pp. 321–334, 1949.

[89] D. A. Baylor, B. J. Nunn, and J. L. Schnapf, “The photocurrent, noise and spectral sensitivity of rods of the monkey Macaca fascicularis.,” *J. Physiol.*, vol. 357, pp. 575–607, Dec. 1984.

[90] E. Boettner and J. Wolter, “Transmission of the ocular media,” *Invest. Ophthalmol. Vis. Sci.*, vol. 1, no. 6, pp. 776–783, 1962.

[91] S. Schlamminger, D. Haddad, F. Seifert, L. S. Chao, D. B. Newell, R. Liu, R. L. Steiner, and J. R. Pratt, “Determination of the Planck constant using a watt balance with a superconducting magnet system at the National Institute of Standards and Technology,” Jan. 2014.

[92] J. J. Mares, P. Hubik, V. Spicka, J. Stavek, J. Sestak, and J. Kristofik, “Shadows over the speed of light,” *Phys. Scr.*, no. T151, 2012.

[93] S. K. Shevell and Optical Society of America., *The science of color*. Elsevier, 2003.

[94] L. Grand, *Optique physiologie. La Dioptrique de l’oeil et sa correction. [Préface de Charles Fabry.]*, Tome 1er. Paris, 1946.

[95] S. Sivaprasad, J. C. Vasconcelos, A. T. Prevost, H. Holmes, P. Hykin, S. George, C. Murphy, J. Kelly, G. B. Arden, F. CLEOPATRA Study Group, A. Bhatnagar, N. Narendran, R. Chavan, A. Cole, R. Crosby-Nwaobi, N. Patrao, D. Menon, C. Hogg, G. Rubin, L. Leitch-Devlin, C. Egan, N. Shah, T. Mansour, T. Peto, H. Eleftheriadis, J. Gibson, A. Ghulakhszian, G. Vafidis, E. Hughes, A. Jafree, G. Menon, P. Prakash, M. Sandinha, R. Smith, P. Scanlon, S. Chave, S. Aldington, A. Dale, G. Hood, G. A. Hitman, D. Crabb, A. Denniston, D. Lewin, I. Grierson, S. Walker, J. Sturt, and D. Sahu, “Clinical efficacy and safety of a light mask for prevention of dark adaptation in treating and preventing progression of early diabetic macular oedema at 24 months (CLEOPATRA): a multicentre, phase 3, randomised controlled trial.,” *lancet. Diabetes Endocrinol.*, vol. 6, no. 5, pp. 382–391, May 2018.

[96] G. B. Arden, S. Jyothi, C. H. Hogg, Y. F. Lee, and S. Sivaprasad, “Regression of early diabetic macular oedema is associated with prevention of dark adaptation,” *Eye*, vol. 25, no. 12, pp. 1546–1554, 2011.

[97] D. J. Ramsey and G. B. Arden, “Hypoxia and Dark Adaptation in Diabetic Retinopathy: Interactions, Consequences, and Therapy,” *Curr. Diab. Rep.*, vol. 15, no. 12, p. 118, Dec. 2015.

[98] G. B. Arden, G. B. Arden, R. L. Sidman, R. L. Sidman, W. Arap, W. Arap, R. O. Schlingemann, and R. O. Schlingemann, “Spare the rod and spoil the eye.,” *Br. J. Ophthalmol.*, vol. 89, no. 6, pp. 764–9, 2005.

[99] G. Arden, M. Gündüz, A. Kurtenbach, M. Völker, E. Zrenner, S. Gündüz, B. Öztürk, and S. Okudan, “A preliminary trial to determine whether prevention of dark adaptation affects the course of early diabetic retinopathy,” *Eye*, vol. 24, no. October 2009, pp. 1149–1155, 2010.

[100] I. G. Pavel Kuchynka1 and Miroslav Veith1*and Duncan Hill3, “Patients with Diabetic Eye Disease using a Potentially Therapeutic Mask. Do Sufficient Patients Wear the Mask and For How Long?,” *Adv. Ophthalmol. Vis. Syst.*, vol. 7, no. 7, pp. 1–9, Dec. 2017.

[101] A. Bierman, M. G. Figueiro, and M. S. Rea, “Measuring and predicting eyelid spectral transmittance,” *J. Biomed. Opt.*, vol. 16, no. 6, p. 067011, 2011.

[102] R. H. Spector, *The Pupils*. Butterworths, 1990.

[103] H. Krastel, E. Alexandridis, and D. Rating, “[Sleep modifies anticholinergic mydriasis].,” *Ophthalmologe*, vol. 93, no. 4, pp. 476–8, Aug. 1996.

[104] Y. Zgeç, M. Prsa, R. Zimmermann, and D. Huber, “Pupil Size Coupling to Cortical States Protects the Stability of Deep Sleep via Parasympathetic Modulation,” *Curr. Biol.*, vol. 28, p. 392–400.e3, 2018.

[105] V. Daneault, G. Vandewalle, M. Hébert, P. Teikari, L. S. Mure, J. Doyon, C. Gronfier, H. M. Cooper, M. Dumont, and J. Carrier, “Does pupil constriction under blue and green monochromatic light exposure change with age?,” *J. Biol. Rhythms*, vol. 27, no. 3, pp. 257–64, Jun. 2012.

[106] L. Jacobs, M. Feldman, and M. B. Bender, “Eye Movements During Sleep,” *Arch. Neurol.*, vol. 25, no. 2, p. 151, Aug. 1971.

[107] W. L. Wolfe, *Introduction to radiometry*. SPIE Optical Engineering Press, 1998.

[108] J. T. Mosst, A. DeFosset, L. Gase, L. Baetscher, and T. Kuo, “A Framework for Implementing the National Diabetes Prevention Program in Los Angeles County,” *Prev Chronic Dis*, vol. 14, pp. 1–10, 2017.

[109] L. R. Martin, S. L. Williams, K. B. Haskard, and M. R. Dimatteo, “The challenge of patient adherence.,” *Ther. Clin. Risk Manag.*, vol. 1, no. 3, pp. 189–99, Sep. 2005.

[110] R. R. Rubin, “Adherence to pharmacologic therapy in patients with type 2 diabetes mellitus,” *Am. J. Med.*, vol. 118, no. 5 SUPPL., 2005.

[111] Y. S. Bonneh, T. H. Donner, A. Cooperman, D. J. Heeger, and D. Sagi, “Motion-induced blindness and Troxler fading: Common and different mechanisms,” *PLoS One*, vol. 9, no. 3, 2014.

[112] Troxler IPV, *Uber das Verschwinden gegeb- ener Gegenstande innerhalb unseres Gesichtskreises*, vol. II, no. 2. Ophthalmologische Bibliothek, 1804.

[113] C. a Burbeck and D. H. Kelly, “Role of local adaptation in the fading of stabilized images.,” *J. Opt. Soc. Am. A.*, vol. 1, no. 2, pp. 216–20, 1984.

[114] L. E. Arend and G. T. Timberlake, “What is psychophysically perfect image stabilization? Do perfectly stabilized images always disappear?,” *J. Opt. Soc. Am. A*, vol. 3, no. 2, pp. 235–241, 1986.

[115] H. J. M. Gerrits, B. D. Haan, and A. J. H. Vendrik, “Experiments with retinal stabilized images. Relations between the observations and neural data,” *Vision Res.*, vol. 6, no. 7–8, pp. 427–440, 1966.

[116] R. Teghtsoonian, “On the exponents in Stevens’ law and the constant in Ekman’s law.,” *Psychol. Rev.*, vol. 78, no. 1, pp. 71–80, Jan. 1971.

[117] I. Kang, R. E. Reem, A. L. Kaczmarowski, and J. G. Malpeli, “Contrast sensitivity of cats and humans in scotopic and mesopic conditions.,” *J. Neurophysiol.*, vol. 102, no. 2, pp. 831–40, Aug. 2009.

[118] K. Obayashi, K. Saeki, and N. Kurumatani, “Bedroom Light Exposure at Night and the Incidence of Depressive Symptoms: A Longitudinal Study of the HEIJO-KYO Cohort,” *Am. J. Epidemiol.*, vol. 187, no. 3, pp. 427–434, Mar. 2018.

[119] J. N. Sahni, G. Czanner, T. Gutu, S. A. Taylor, K. M. Bennett, S. M. Wuerger, I. Grierson, C. Murray-Dunning, M. N. Holland, and S. P. Harding, “Safety and acceptability of an organic light-emitting diode sleep mask as a potential therapy for retinal disease,” *Eye*, vol. 31, no. 1, pp. 97–106, 2017.

[120] R. Traub and G. Jensen, “Tritium Radioluminescent Devices Health and Safety,” 1995.

[121] RDPM and ST, “Specification trigalight ®,” Niederwangen, Switzerland, 2018.

[122] H. Gümüş, “Simple stopping power formula for low and intermediate energy electrons,” *Radiat. Phys. Chem.*, vol. 72, no. 1, pp. 7–12, 2005.

[123] M. J. Berger, J. S. Course, M. A. Zucker, and J. Chang, “Stopping-Power and Range Tables for Electrons, Protons, and Helium Ions,” *NIST*, 2017. [Online]. Available: https://www.nist.gov/pml/stopping-power-range-tables-electrons-protons-and-helium-ions. [Accessed: 11-Jul-2018].

[124] Particle Data Group, “Atomic and nuclear properties of borosilicate glass (Pyrex Corning 7740).” [Online]. Available: http://pdg.lbl.gov/2015/AtomicNuclearProperties/HTML/borosilicate_glass_Pyrex_Corning_7740.html. [Accessed: 18-Oct-2018].

[125] H. Bichsel, D. E. Groom, and S. R. Klein, “Passage of Particles Through Matter,” *Chinese Phys. Lett.*, pp. 1–42, 2013.

[126] A. E. Krieger, “The pars plana incision: experimental studies, pathologic observations, and clinical experience.,” *Trans. Am. Ophthalmol. Soc.*, vol. 89, pp. 549–621, 1991.

[127] M. de Frutos-Lezaun, I. Rodriguez-Agirretxe, F. Eder Labairu, and C. Irigoyen, “Vitrectomy combined with posterior-segment Ahmed valve implant: A case series study,” *Saudi J. Ophthalmol.*, vol. 32, no. 3, pp. 180–187, Jul. 2018.

[128] C. Jaboro, “An in vivo study of the biocompatibility of classic and novel device materials on the central nervous system,” Wayne State University, 2007.

[129] B. D. Ratner, A. S. Hoffman, F. J. Schoen, and J. E. Lemons, *Biomaterials science: an introduction to materials in medicine*, 2nd ed. Amsterdam; Boston: Elsevier Academic Press, 2004.

[130] C. Deboer, “Biomimetic Accommodating Intraocular Lens,” California Institute of Technology, 2012.

[131] S. Vurgese, S. Panda-Jonas, and J. B. Jonas, “Scleral Thickness in Human Eyes,” *PLoS One*, vol. 7, no. 1, p. e29692, Jan. 2012.

[132] T. L. Maus and R. F. Brubaker, “Measurement of aqueous humor flow by fluorophotometry in the presence of a dilated pupil.,” *Invest. Ophthalmol. Vis. Sci.*, vol. 40, no. 2, pp. 542–6, Feb. 1999.

[133] J. L. Ecker, O. N. Dumitrescu, K. Y. Wong, N. M. Alam, S.-K. Chen, T. LeGates, J. M. Renna, G. T. Prusky, D. M. Berson, and S. Hattar, “Melanopsin-expressing retinal ganglion-cell photoreceptors: cellular diversity and role in pattern vision.,” *Neuron*, vol. 67, no. 1, pp. 49–60, Jul. 2010.

[134] T. M. Schmidt and P. Kofuji, “Functional and morphological differences among intrinsically photosensitive retinal ganglion cells,” *J. Neurosci.*, vol. 29, no. 2, pp. 476–482, 2009.

[135] B. M. Kevany and K. Palczewski, “Phagocytosis of Retinal Rod and Cone Photoreceptors,” *Physiology*, vol. 25, no. 1, pp. 8–15, Feb. 2010.

[136] “List of Mydriatics,” *Drugs.com*, 2018. [Online]. Available: https://www.drugs.com/drug-class/mydriatics.html. [Accessed: 24-Jul-2018].

[137] K. Boyd and B. Pagan-Duran, “What Are Dilating Eye Drops?,” *American Academy of Opthamology*, 2017. [Online]. Available: https://www.aao.org/eye-health/drugs/dilating-eyedrops. [Accessed: 24-Jul-2018].

[138] J. M. Kim, K. H. Park, S. Y. Han, K. S. Kim, D. M. Kim, T. W. Kim, and J. Caprioli, “Changes in intraocular pressure after pharmacologic pupil dilation,” *BMC Ophthalmol.*, vol. 12, no. 1, p. 53, Dec. 2012.

[139] J. G. Robson and L. J. Frishman, “Dissecting the dark-adapted electroretinogram.,” *Doc. Ophthalmol.*, vol. 95, no. 3–4, pp. 187–215.

[140] I. Perlman, “Relationship between the amplitudes of the b wave and the a wave as a useful index for evaluating the electroretinogram.,” *Br. J. Ophthalmol.*, vol. 67, no. 7, pp. 443–8, Jul. 1983.

[141] A. Cameron, O. Mahroo, and T. Lamb, “Dark adaptation of human rod bipolar cells measured from the b-wave of the scotopic electroretinogram.,” *J. Physiol.*, vol. 575, no. Pt 2, pp. 507–526, 2006.

[142] A. Hughes, “A schematic eye for the rabbit,” *Vision Res.*, vol. 12, no. 1, pp. 123-IN6, Jan. 1972.

[143] M. F. Deering, M. F., Deering, and M. F., “A photon accurate model of the human eye,” *ACM Trans. Graph.*, vol. 24, no. 3, p. 649, Jul. 2005.

[144] Y. M. Liu and P. Xie, “The safety of orthokeratology - A systematic review,” *Eye Contact Lens*, vol. 42, no. 1, pp. 35–42, 2016.

[145] Polymer Technology, “A Guide to Overnight ORTHOKERATOLOGY,” 2004.

[146] “Paragon CRT Contact Lenses: Innovative Technology,” *Paragon Vision Sciences*, 2017. [Online]. Available: https://www.paragonvision.com/ecp/products/crt. [Accessed: 03-Dec-2017].

[147] B. A. Holden, T. R. Fricke, D. A. Wilson, M. Jong, K. S. Naidoo, P. Sankaridurg, T. Y. Wong, T. J. Naduvilath, and S. Resnikoff, “Global Prevalence of Myopia and High

Myopia and Temporal Trends from 2000 through 2050," *Ophthalmology*, vol. 123, no. 5, pp. 1036–1042, May 2016.

[148] T. S. Kuntzleman, K. Rohrer, and E. Schultz, "The Chemistry of Lightsticks: Demonstrations To Illustrate Chemical Processes," *J. Chem. Educ.*, vol. 89, no. 7, pp. 910–916, Jun. 2012.

[149] T. F. de Oliveira, A. L. M. da Silva, R. A. de Moura, R. Bagattini, A. A. F. de Oliveira, M. H. G. de Medeiros, P. Di Mascio, I. P. de Arruda Campos, F. P. Barretto, E. J. H. Bechara, and A. P. de Melo Loureiro, "Luminescent threat: toxicity of light stick attractors used in pelagic fishery," *Sci. Rep.*, vol. 4, no. 1, p. 5359, May 2015.

[150] T. Vettese and J. J. Hurwitz, "Toxicity of the chemiluminescent material Cyalume in anatomic assessment of the nasolacrimal system.," *Can. J. Ophthalmol.*, vol. 18, no. 3, pp. 131–5, Apr. 1983.

[151] R. J. Hoffman, L. S. Nelson, and R. S. Hoffman, "Pediatric and young adult exposure to chemiluminescent glow sticks.," *Arch. Pediatr. Adolesc. Med.*, vol. 156, no. 9, pp. 901–4, Sep. 2002.

[152] Smurrayinchester, "Cyalume-reactions," *Wikimedia Commons*, 2007. [Online]. Available: https://commons.wikimedia.org/wiki/File:Cyalume-reactions.svg. [Accessed: 19-Nov-2018].

[153] L. Maggie, "Data Sheet for XZBGR155W5MAV," 2016.

[154] R. Shadid and S. Noghanian, "Review Article A Literature Survey on Wireless Power Transfer for Biomedical Devices," *Int. J. Antennas Propag.*, vol. 2018, 2018.

[155] M. A. Hannan, H. A. Hussein, S. Mutashar, S. A. Samad, and A. Hussain, "Automatic frequency controller for power amplifiers used in bio-implanted applications: Issues and challenges," *Sensors (Switzerland)*, vol. 14, no. 12, pp. 23843–23870, 2014.

[156] H. A. Wheeler, "Simple Inductance Formulas for Radio Coils," *Proc. IRE*, vol. 16, no. 10, pp. 1398–1400, Oct. 1928.

[157] A. Vander Vorst, A. Rosen, and Y. Kotsuka, *RF / Microwave Interaction with Biological Tissues*. 2006.

[158] H. W. Johnson and M. Graham, *High-speed digital design : a handbook of black magic*. Prentice Hall, 1993.

[159] I. Cadence Design Systems, "Modeling Schottky Diodes | PSpice," 2016. [Online]. Available: https://www.pspice.com/resources/application-notes/modeling-schottky-diodes. [Accessed: 12-Oct-2018].

[160] L. Edwards, “Samsung contact lens displays will put AR video and cameras in your eyes - Pocket-lint,” *Pocket-lint*, 2016. [Online]. Available: https://www.pocket-lint.com/ar-vr/news/samsung/137239-samsung-contact-lens-displays-will-put-ar-video-and-cameras-in-your-eyes. [Accessed: 23-Jun-2018].

[161] M. V Riley, “Glucose and oxygen utilization by the rabbit cornea.,” *Exp. Eye Res.*, vol. 8, no. 2, pp. 193–200, Apr. 1969.

[162] S. D. Klyce, “Stromal lactate accumulation can account for corneal oedema osmotically following epithelial hypoxia in the rabbit.,” *J. Physiol.*, vol. 321, pp. 49–64, Dec. 1981.

[163] R. D. Freeman, “Oxygen consumption by the component layers of the cornea.,” *J. Physiol.*, vol. 225, no. 1, pp. 15–32, Aug. 1972.

[164] I. Fatt, R. D. Freeman, and D. Lin, “Oxygen tension distributions in the cornea: A re-examination,” *Exp. Eye Res.*, vol. 18, no. 4, pp. 357–365, Apr. 1974.

[165] V. Compa˜n, C. Oliveira, M. Aguilella-Arzo, S. Moll´a, S. C. Peixoto-de-Matos, and J. M. Gonz´alez-M´eijome, “Oxygen diffusion and edema with modern scleral rigid gas permeable contact lenses,” *Investig. Ophthalmol. Vis. Sci.*, vol. 55, no. 10, pp. 6421–6429, 2014.

[166] B. A. Holden and G. W. Mertz, “Critical oxygen levels to avoid corneal edema for daily and extended wear contact lenses.,” *Invest. Ophthalmol. Vis. Sci.*, vol. 25, no. 10, pp. 1161–7, Oct. 1984.

[167] G. W. Mertz, “Overnight swelling of the living human cornea.,” *J. Am. Optom. Assoc.*, vol. 51, no. 3, pp. 211–4, Mar. 1980.

[168] R. B. Mandell and I. Fatt, “Thinning of the human cornea on awakening.,” *Nature*, vol. 208, no. 5007, pp. 292–3, Oct. 1965.

[169] M. D. Sarver, D. A. Baggett, M. G. Harris, and K. Louie, “Corneal edema with hydrogel lenses and eye closure: Effect of oxygen transmissibility,” *Optometry and Vision Science*, vol. 58, no. 5. pp. 386–392, 1981.

[170] N. A. Brennan, “Beyond flux: total corneal oxygen consumption as an index of corneal oxygenation during contact lens wear.,” *Optom. Vis. Sci.*, vol. 82, no. 6, pp. 467–472, 2005.

[171] D. M. Harvitt and J. A. Bonanno, “Re-evaluation of the oxygen diffusion model for predicting minimum contact lens Dk/t values needed to avoid corneal anoxia.,” *Optom. Vis. Sci.*, vol. 76, no. 10, pp. 712–9, Oct. 1999.

[172] R. Hill and W. Jeppe, “Hydrogels: Is a pump still necessary?,” *Int. Contact Lens Clin.*, vol. 2, no. 4, pp. 27–29, 1975.

[173] W. J. Benjamin, “EOP and Dk/L: the quest for hyper transmissibility.,” *J. Am. Optom. Assoc.*, vol. 64, no. 3, pp. 196–200, Mar. 1993.

[174] Paragon Vision Sciences, “Gas Permeable Materials.” [Online]. Available: https://www.paragonvision.com/ecp/products/gp-materials. [Accessed: 20-Oct-2018].

[175] L. Menicon Co., “Menicon Z.” [Online]. Available: http://www.menicon.com/pro/our-products/gp-lens/menicon-z/. [Accessed: 20-Oct-2018].

[176] R. B. Bird, W. E. Stewart, and E. N. Lightfoot, *Transport phenomena*. New York: John Wiley and Sons, Inc, 1960.

[177] R. D. Freeman and I. Fatt, “Oxygen Permeability of the Limiting Layers of the Cornea,” *Biophys. J.*, vol. 12, no. 3, pp. 237–247, 1972.

[178] P. Buchwald, “FEM-based oxygen consumption and cell viability models for avascular pancreatic islets,” *Theor. Biol. Med. Model.*, vol. 6, no. 1, 2009.

[179] T. Merkel and V. Bondar, “Gas sorption, diffusion, and permeation in poly (dimethylsiloxane),” *J. Polym. Sci. Part B Polym. Phys.*, pp. 415–434, 2000.

[180] S. Gruener, D. Wallacher, S. Greulich, M. Busch, and P. Huber, “Hydraulic transport across hydrophilic and hydrophobic nanopores: Flow experiments with water and n-hexane,” *Phys. Rev. E*, vol. 93, no. 1, 2016.

[181] M. J. Tang, R. A. Cox, and M. Kalberer, “Compilation and evaluation of gas phase diffusion coefficients of reactive trace gases in the atmosphere: Volume 1. Inorganic compounds,” *Atmos. Chem. Phys.*, vol. 14, no. 17, pp. 9233–9247, 2014.

[182] E. N. Fuller, P. D. Schettler, and J. C. Giddings, “NEW METHOD FOR PREDICTION OF BINARY GAS-PHASE DIFFUSION COEFFICIENTS,” *Ind. Eng. Chem.*, vol. 58, no. 5, pp. 18–27, May 1966.

[183] Z. He, F. Forest, P. Gain, D. Rageade, A. Bernard, S. Acquart, M. Peoc’h, D. M. Defoe, and G. Thuret, “3D map of the human corneal endothelial cell,” *Sci. Rep.*, vol. 6, no. 1, p. 29047, Sep. 2016.

[184] B. A. Holden and D. F. Sweeney, “The oxygen tension and temperature of the superior palpebral conjunctiva,” *Acta Ophthalmol.*, vol. 63, no. 1, pp. 100–103, May 2009.

[185] R. E. Barr and I. A. Silver, “Effects of corneal environment on oxygen tension in the anterior chambers of rabbits.,” *Invest. Ophthalmol.*, vol. 12, no. 2, pp. 140–4, Feb. 1973.

[186] S. C. Takatori, P. L. de la Jara, B. Holden, K. Ehrmann, A. Ho, and C. J. Radke, “In Vivo Oxygen Uptake into the Human Cornea,” *Investig. Opthalmology Vis. Sci.*, vol. 53, no. 10, p. 6331, 2012.

[187] J. A. Bonanno, T. Stickel, T. Nguyen, T. Biehl, D. Carter, W. J. Benjamin, and P. Sarita Soni, “Estimation of human corneal oxygen consumption by noninvasive measurement of tear oxygen tension while wearing hydrogel lenses,” *Investig. Ophthalmol. Vis. Sci.*, vol. 43, no. 2, pp. 371–376, 2002.

[188] G. D. B. and A. P. R. Gokul K. C., “Thermal effects of eyelid in human eye temperature model,” *Appl. Math. Informatics*, vol. 32, no. 5–6, pp. 649–663, 2014.

[189] X. Larrea and P. Büchler, “A transient diffusion model of the cornea for the assessment of oxygen diffusivity and consumption,” *Investig. Ophthalmol. Vis. Sci.*, vol. 50, no. 3, pp. 1076–1080, 2009.

[190] S. K. Mitra and S. Chakraborty, *Microfluidics and nanofluidics handbook : fabrication, implementation, and applications*. CRC Press, 2012.

[191] V. C. Pinto, P. J. Sousa, V. F. Cardoso, and G. Minas, “Optimized SU-8 processing for low-cost microstructures fabrication without cleanroom facilities,” *Micromachines*, vol. 5, no. 3, pp. 738–755, 2014.

[192] E. Koukharenko, M. Kraft, G. J. Ensell, and N. Hollinshead, “A comparative study of different thick photoresists for MEMS applications,” vol. 6, pp. 741–747, 2005.

[193] DuPont, “DuPont ™ WBR ™ 2000 Series - DATA SHEET & PROCESSING INFORMATION FOR MICROLITHOGRAPHIC POLYMER FILM,” 2000.

[194] D. Nührmann, *Das große Werkbuch Elektronik : [Ausg. in 4 Bd.] / 1 Tabellen, Mathematik, Formeln, Mechanik und mechanische Baugruppen, Berechnungsgrundlagen für Elektronikschaltungen, Kühlkörper, Leiterplattentechnik, SMD-Technik, Starkstromversorgungstechnik.* Franzis, 1998.

[195] P. Macleod, *Technology Watch: A Review of Flexible Circuit Technology and its Applications*, no. June 2002. 2002.

[196] D. C. Rodger, A. J. Fong, W. Li, H. Ameri, A. K. Ahuja, C. Gutierrez, I. Lavrov, H. Zhong, P. R. Menon, E. Meng, J. W. Burdick, R. R. Roy, V. R. Edgerton, J. D. Weiland, M. S. Humayun, and Y. C. Tai, “Flexible parylene-based multielectrode array technology for high-density neural stimulation and recording,” *Sensors Actuators, B Chem.*, vol. 132, no. 2, pp. 449–460, 2008.

[197] W. Li, D. C. Rodger, E. Meng, J. D. Weiland, M. S. Humayun, and Y.-C. Tai, "Flexible Parylene Packaged Intraocular Coil for Retinal Prostheses," in *2006 International Conference on Microtechnologies in Medicine and Biology*, 2006, pp. 105–108.